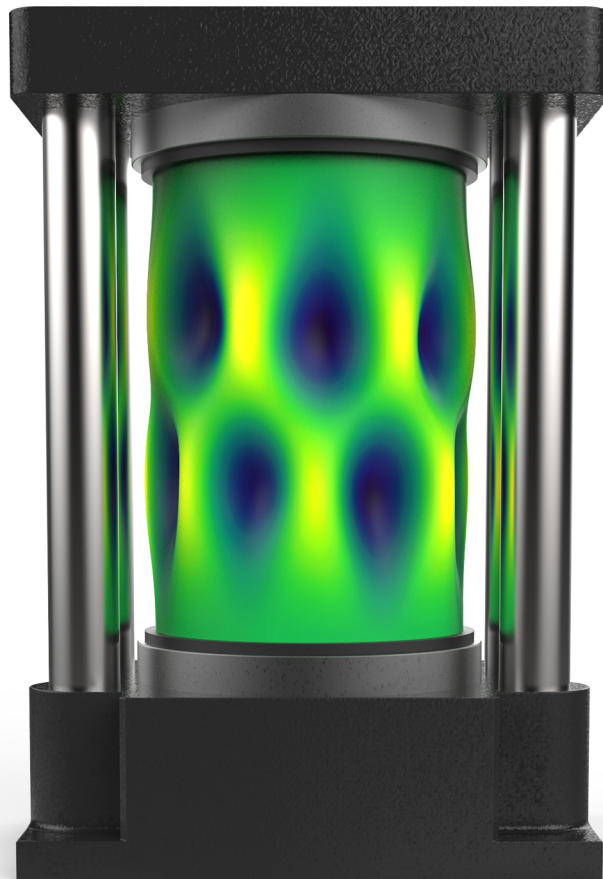


MASTER OF SCIENCE THESIS

# Composite Cylindrical Shell Buckling: Simulation & Experimental Correlation

David J. Eberlein



Faculty of Aerospace Engineering · Delft University of Technology



# **Composite Cylindrical Shell Buckling: Simulation & Experimental Correlation**

MASTER OF SCIENCE THESIS

For obtaining the degree of Master of Science in Aerospace Engineering  
at Delft University of Technology

David Jeffrey Eberlein

October 9, 2019



DELFT UNIVERSITY OF TECHNOLOGY  
FACULTY OF AEROSPACE ENGINEERING  
DEPARTMENT OF AEROSPACE STRUCTURES AND MATERIALS

**GRADUATION COMMITTEE**

Dated: October 9, 2019

Chair holder:

\_\_\_\_\_  
Prof. Dr. Chiara Bisagni

Committee members:

\_\_\_\_\_  
Dr. Ir. Otto K. Bergsma

\_\_\_\_\_  
Dr. Ing. Saullo G.P. Castro



---

# Abstract

Guidelines dating back 50 years, NASA SP-8007, are employed today in the design of thin-walled launch vehicle structures. Due to advances in materials, structural designs, and manufacturing techniques since the publication of SP-8007, the development of new knockdown factors for contemporary launch vehicle structures is an ongoing subject of research. The work presented herein was performed in collaboration with the NASA Engineering and Safety Center on the Shell Buckling Knockdown Factor Project.

A laboratory-scale composite cylindrical shell test article, which had previously been designed according to a novel scaling methodology, was the subject of simulation and testing. Its inner, outer, and boundary surface imperfection signatures were measured and implemented in finite element models for buckling test simulations. These were then used to provide prediction data for an experiment conducted at NASA Langley Research Center. Buckling loads from the two pre-test analyses were within 0.08% and 3.7% of the experimental buckling load. The concurrence of axial shell stiffness, localized strains, and buckling shape evolution was also established between the experiment and simulations. A slight loading imperfection was found during the test; however, it was demonstrated through post-test analyses that this did not affect the buckling load substantially.

The test article's 0.91 normalized buckling load was much higher than the 0.59 knockdown factor specified by SP-8007. The correlation between the experimental and simulation results, as well as their contrast with SP-8007's prescription, suggests that directly measured imperfections are capable of playing a role in the development of modern and potentially less conservative knockdown factors for future launch vehicle structures.



---

# Table of Contents

<b>Acknowledgments</b>	<b>v</b>
<b>1 Introduction</b>	<b>1</b>
<b>2 Literature Review</b>	<b>5</b>
2.1 Research with Directly Measured Imperfections . . . . .	5
2.2 Comparison of Data from Simulation and Experiments . . . . .	15
2.3 Modeling and Analysis Considerations . . . . .	17
2.3.1 Imperfection Implementation . . . . .	17
2.3.2 Modeling Experimental Setups . . . . .	19
2.3.3 Additional Modeling Details . . . . .	20
<b>3 Simplified Shell Description &amp; Modeling</b>	<b>23</b>
3.1 Geometry, Material, and Layup . . . . .	23
3.2 Analytical Buckling Load . . . . .	25
3.3 Finite Element Modeling . . . . .	25
<b>4 Analyses of the Simplified Shell without Imperfections</b>	<b>29</b>
4.1 Eigenvalue Buckling Analyses . . . . .	29
4.2 Linear Static Analysis . . . . .	31
4.3 Nonlinear Dynamic Analysis . . . . .	31
<b>5 Eigenmode &amp; Trigonometric Imperfections</b>	<b>33</b>
5.1 Eigenmode Shape Imperfections . . . . .	33
5.2 Trigonometric Imperfections . . . . .	35
5.3 Conclusions on Eigenmode and Trigonometric Imperfections . . . . .	38

---

<b>6</b>	<b>Loading Imperfections</b>	<b>39</b>
6.1	Loading Imperfection 1: Settling Platen . . . . .	39
6.2	Loading Imperfection 2: Platen with Fixed Angular Offset . . . . .	42
6.3	Conclusions on Loading Imperfections . . . . .	43
<b>7</b>	<b>NDL-1 Description &amp; Measured Imperfection Signature</b>	<b>45</b>
7.1	NDL-1 Specifications . . . . .	45
7.1.1	Shell . . . . .	45
7.1.2	Potting and End Rings . . . . .	46
7.2	Imperfection Measurement Data . . . . .	48
7.2.1	Inner and Outer Surfaces . . . . .	49
7.2.2	Boundary Surfaces . . . . .	50
<b>8</b>	<b>NDL-1 Modeling &amp; Preliminary Simulation Results</b>	<b>53</b>
8.1	Test Article Model . . . . .	53
8.1.1	Element Type and Mesh Size . . . . .	53
8.1.2	Input File Generation . . . . .	54
8.1.3	Final Mesh Details . . . . .	55
8.1.4	Interpolated Imperfection Surfaces . . . . .	56
8.2	Choice of Composite Material Properties for Simulation . . . . .	61
8.3	Preliminary NDL-1 Simulation Results with Imperfections . . . . .	65
<b>9</b>	<b>Experimental Results &amp; Simulation Correlation</b>	<b>73</b>
9.1	Load-Displacement . . . . .	77
9.2	Load-Strain . . . . .	82
9.3	Pre-buckling and Buckling Shape Evolution . . . . .	89
9.3.1	Pre-buckling . . . . .	89
9.3.2	Buckling Event . . . . .	96
9.4	Additional Observations . . . . .	104
<b>10</b>	<b>Conclusions</b>	<b>107</b>
	<b>References</b>	<b>111</b>

---

# Acknowledgments

This work would not have been possible without the support of many individuals. I greatly appreciate the help of the following people. . .

Thanks to Professor Chiara Bisagni for providing the opportunity to collaborate with NASA and for her guidance during this project. As an American who came to the Netherlands specifically for this master's program, I did not imagine the possibility of working with NASA for the thesis; it was an honor and a humbling experience. Additionally, Professor Bisagni has taught me a multitude of invaluable skills that I look forward to applying to future endeavors, including: making detailed scientific information easily interpretable and logically structured; the importance of keeping organized simulation data; having a healthy skepticism of averages; and perhaps most importantly, that when modeling and simulating physical phenomena, one must not get so lost in the minutiae as to lose track of what is actually happening in reality.

Thanks to Professor Saullo Castro and Professor Otto Bergsma for agreeing to partake in my graduation committee. Professor Castro kindly provided advice on interpolation and numerical simulation from the early stages of my thesis, before either of us knew that he might be on the committee. Professor Bergsma's course on the design of lightweight structures was particularly inspiring by connecting theoretical concepts to the practical engineering mindset.

Thanks to Dr. Marc R. Schultz of NASA Langley Research Center and Michelle T. Rudd of NASA Marshall Space Flight Center for providing advice and ideas throughout the course of the thesis. It was a pleasure to work with both them on this project, and their views provided unique insights into the approaches taken to advanced structural research.

Thanks to Inés Uriol Balbin for her openness, enthusiasm, and availability to discuss all matters related to shell buckling, big-picture and detailed information alike. At one point, one of her office mates actually thought she was my co-advisor (she was not).

Thanks to my fellow ASM master's students and colleagues in the Aerospace Structures and Computational Mechanics research group for helping to make this a great experience.

Finally, thanks to my parents, Jane and Robert, and my partner, Tessa, for their support during this intense and rewarding project.



---

# Chapter 1

---

## Introduction

A crucial aspect of designing the unstiffened thin-walled cylindrical shell structures found in space launch vehicles is ensuring that they can withstand a specified axially compressive load without buckling. Once buckled, cylindrical shells may experience a significant reduction of load capacity and stiffness. Furthermore, the incipient deformations can cause failure of the constituent material(s). Therefore, judiciousness must be employed when designing these structures so that this stability phenomenon does not occur during operation.

However, the well-documented imperfection-sensitive nature of thin-walled shells complicates this matter. While the theoretical buckling load of cylindrical shells can be calculated analytically, it has been known for around a century that experimental buckling loads are often lower due to imperfections inherent to manufactured structures [1, 2, 3, 4].

As a result, statistically based “knockdown factors” (KDFs) are used to account for the observed discrepancy when designing such structures. The document containing these industry-standard guidelines, NASA SP-8007 [5], was last updated in 1968, and consequently its prescriptions do not always account for the designs, materials, and construction techniques utilized in contemporary launch vehicle structures (e.g. sandwich structures with composite face sheets). Advances in computational mechanics (and measurement devices) since SP-8007’s last revision have also enabled unique topological imperfections signatures to be modeled with increasing fidelity, and it will be demonstrated that doing so can predict experimental buckling loads more accurately than analytical solutions and statistical knockdown factors.

When applied to modern composite shells, SP-8007 has been known to give mixed results in terms of conservatism. As noted by Hilburger and Starnes Jr. [6], these guidelines may be unconservative if the statistical data upon which they are based do not reflect the shell construction method of interest. In 2016, NASA even warned that structural designers should be prudent when attempting to apply SP-8007 to composite shells [7]. On the other hand, it is thought that in many cases SP-8007 KDFs may be overly conservative [8, 9, 10, 11, 12]. In the event that some currently employed KDFs are too conservative, there is an added bonus that modernized KDFs could lead to decreased structural mass. This in turn could reduce launch costs, which in 2017 ranged from \$10,000 to \$100,000 (US) per kilogram [13].

A leading initiative in devising new knockdown factors is the NASA Engineering and Safety Center’s Shell Buckling Knockdown Factor Project. In addition to researching full-scale launch vehicle structures, the project has been investigating the role that laboratory-scale shells can play in the development process. Delft University of Technology collaborates with NASA in that effort [14, 15]. The work herein concerns a laboratory-scale composite cylindrical shell test article, referred to as NDL-1, which was derived from NASA’s full-scale test article CTA8.1 and manufactured at NASA Marshall Space Flight Center.

Figure 1.1 shows the process by which NDL-1 was designed from CTA8.1 (this was not performed by the present author). The employed scaling methodology was developed by Uriol Balbin et al. [16] and prescribes scaling via parameters derived from nondimensionalized anisotropic cylindrical shell buckling equations. Because these equations apply to purely isolated shells – rather than to test articles that have additional features necessary for experiments – two simplified shell designs were used as intermediaries between the designs of CTA8.1 and NDL-1; however, neither simplified shell was manufactured.

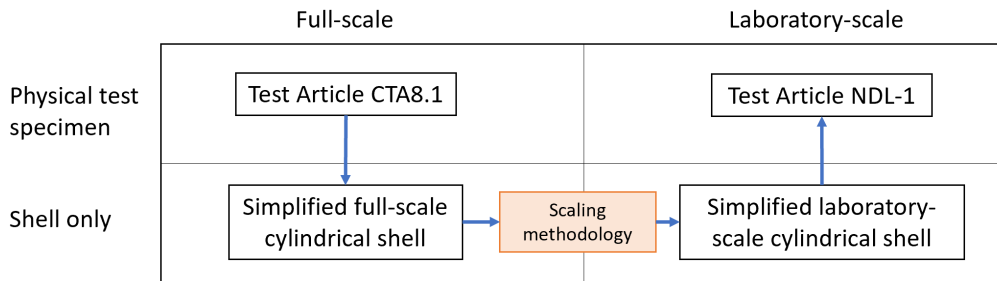


**Figure 1.1:** Flowchart showing how the laboratory-scale test article NDL-1 was developed from the full-size test article CTA8.1.

As Figure 1.1 indicates, CTA8.1 was initially translated into an equivalent simplified full-scale shell. This was accomplished via iterative numerical analyses, with a priority on matching the buckling load and axial stiffness as closely as possible. Then the scaling methodology was applied to the simplified full-scale shell to produce a simplified laboratory-scale shell. Finally, iterative numerical analyses were conducted to translate the simplified laboratory-scale shell into NDL-1’s design by attempting to match the stiffness and buckling load, while simultaneously adding necessary testing features and accounting for the limitations of the material, manufacturing process, and test-equipment. A key difference between CTA8.1 and NDL-1 is that the former is a sandwich structure with composite face sheets, while the latter features a solid composite laminate; this was a consequence of the scaling methodology and manufacturing considerations.

## Thesis Research

The objective of the thesis was to contribute to the development of modern knockdown factors for composite launch vehicle structures by: simulating NDL-1’s buckling behavior using measured imperfection data from the manufactured shell itself; providing pre-test buckling predictions and related simulation data for use during the buckling experiment of NDL-1 at NASA Langley Research Center; post-processing the test data; and comparing the results of the simulations and the experiment, thus ultimately assessing the simulations’ validity in

light of the test. Pre-test simulations are important for use both during testing and after. They provide reference data for comparison with the experiment as it is happening in real time, giving test personnel a clearer lens through which to monitor for potentially anomalous large-scale behavior. When comparing them to post-processed test data, the lens can further reveal smaller details. As research continues, pre-test simulation techniques may ultimately enable shorter design cycles and reduce the necessity of project-specific experimental testing.

## Report Structure

Chapter 2 provides a review of literature focusing on the use of measured imperfections in composite cylindrical shell modeling, with an emphasis on comparing simulated data to experimental results. Additionally, it provides an overview of common themes pertaining to the intricacies of these simulations.

Chapter 3 presents the specifications of the aforementioned simplified laboratory-scale shell, which was used in preliminary simulations. These details include geometry, material, and layup information, along with the analytical buckling load and the knockdown factor prescribed by SP-8007. This chapter additionally elucidates the choices in finite element modeling of the simplified shell and the reasons for which they were made.

Simulation data for the simplified shell without imperfections is presented in Chapter 4.

The sensitivity of the simplified shell to eigenmode shape and trigonometric imperfections is explored in Chapter 5. The former has been used classically in the estimation of experimental buckling behavior, although it is often considered to give conservative results [17, 18, 19, 20, 21]. The latter was studied in the context of the SP-8007 analytical solution [22], which specifies the analytical shape with which the simplified shell is expected to buckle.

The influence of two loading imperfections arising from the equipment-article interface are studied in Chapter 6 also using the simplified shell. These simulations were performed because in reality, no buckling experiment features perfect load introduction. Furthermore, these loading imperfections can reduce the observed buckling load.

The nominal specifications of NDL-1 are introduced Chapter 7. Additionally, its measured inner, outer, and edge imperfection surfaces are presented.

Chapter 8 covers the modeling and simulation of NDL-1. The process by which NDL-1's specifications and imperfections were transformed into a finite element model is presented. A statistical analysis was also performed to verify the shell model's imperfections were representative of the actual measured imperfection signatures. Additionally, adjustments to the nominal composite material properties are discussed. These adjustments were made based upon the results of a NASA tensile test, as well as thickness information that was derived via the interpolated outer and inner imperfection surfaces. The preliminary results of two simulations are then given.

The experiment, results, and simulation correlation are detailed in Chapter 9. First, the experimental setup and data acquisition sources are introduced. Then data from test and simulation are compared side-by-side. These include load-displacement behavior, load-strain behavior, pre-buckling shape evolution, and post-buckling shape evolution. The concurrence between the experimental and simulated behavior for each of these metrics is assessed.

Finally, Chapter 10 presents conclusions.



---

## Chapter 2

---

# Literature Review

A major aspect of developing knockdown factors for launch vehicle structures involves the numerical estimation of experimental buckling loads. Several approaches have been employed to this end, although only one is discussed here as others are beyond the scope of the thesis research. The strategy herein prescribes the utilization of measured imperfections from physical test specimens in numerical models in order to simulate the buckling behavior of those unique specimens. The use of directly measured imperfections in estimating experimental buckling behavior dates back as far as 1979, when Arbocz championed the creation of reference databases for measured imperfections to enhance the understanding of cylindrical shell buckling, such as in his work with Abramovich [23].

A review of studies from 2000 through the present is given, specifically with a view towards research in which finite element simulations of composite shells with directly measured imperfections were compared to experimental results. Following this, a comparative table summarizes the correlation between numerical and experimental results from several of these research endeavors. Finally, common themes in the practical matters related to simulating cylindrical shell buckling experiments are explored.

### 2.1 Research with Directly Measured Imperfections

In 2000, Bisagni [24] determined that a test article's experimental and simulated buckling loads were significantly lower than the analytical buckling load. The middle portion of a manufactured cylindrical shell's surface was measured, and its imperfection signature was implemented into a finite element model. Imperfections in unmeasured areas of the shell were modeled by linearly tapering the extents of measurement data down to the nominal shell geometry at the edges. The simulated buckling loads of these models – which were found through Riks analysis and nonlinear dynamic analysis – were 15% and 20% higher, respectively, than the experimental buckling load, with the numerical post-buckling load also overestimating that of the experiment. The experimental, Riks analysis, and dynamic analysis normalized buckling loads were 0.68, 0.78, and 0.83, respectively.

Wullschleger and Meyer-Piening [25] published numerical and experimental results for two composite cylindrical shells, Z32 and Z33, with measured geometric imperfections in 2002. Nonlinear dynamic analysis of the shell models without imperfections produced buckling loads of 105 kN and 199 kN, respectively. When geometric imperfections were implemented, analysis revealed reduced buckling loads of 103 kN and 145 kN, respectively. By comparison, the average results from experimental tests at the German Aerospace Center (DLR) and the Swiss Federal Laboratories for Materials Science and Technology (EMPA) gave buckling loads of 91 kN and 179 kN for Z32 and Z33, respectively. Thus analysis with imperfections over-predicted the real buckling load by 13% for Z32 and under-predicted the buckling load by 19% for Z33.

In 2002, Hilburger and Starnes Jr. [26] from NASA Langley Research Center published results of experiments on three solid composite cylindrical shells and compared them each to a range of numerical analysis predictions, as shown in Figure 2.1. The implemented imperfections included mid-surface imperfections, thickness variations, ply gaps, and fiber volume fraction fluctuations. The logic behind producing prediction ranges, rather than discrete predictions, was to attempt to characterize the uncertainty in some parameters, in addition to the effects of the imperfections themselves. Such included uncertainties were related to the imperfection measurement system, nominal fiber volume fraction, and loading. A combinatorial analysis was used to determine the best and worst cases for each set of parameters in the range. The experimental buckling loads for all cylindrical shells were reported normalized to the linear bifurcation load of the C3 model without imperfections (42.59 kip). These were 0.652 for C1, 0.749 for C2, and 0.803 for C3. Hilburger and Starnes Jr. cited that the experimental buckling loads were 7.8%, 13.7%, and 17.6% lower than the loads predicted by the cylindrical shell model analyses without imperfections. They noted, as Figure 2.1 indicates, that the experimental behavior was well-captured by the predicted bounds for C1, and almost captured by the ranges of C2 and C3 predictions. For comparison, Hilburger and Starnes Jr. indicated the NASA SP-8007 KDF is 0.47 for an isotropic shell with the same radius-to-thickness ratio of 200 as the three composite cylindrical shells manufactured.

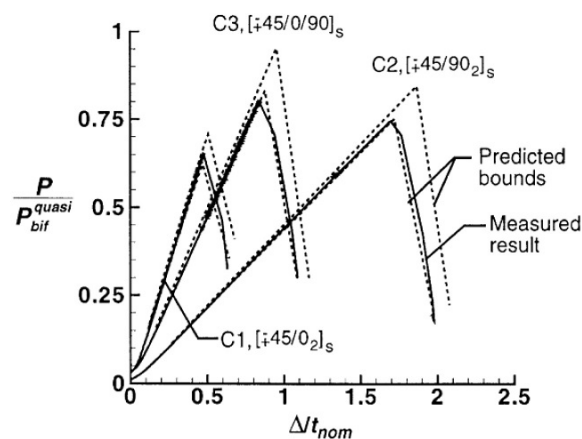


**Figure 2.1:** Experimental results of Hilburger and Starnes Jr. for three cylindrical shells C1, C2, and C3 compared with analysis-based buckling load prediction ranges [26]. The buckling load on the vertical axis is normalized to the linear bifurcation load of C3, and the imposed displacement is normalized to wall thickness on the horizontal axis.

In 2004, Hilburger et al. [17] followed up on that work. For the cylindrical shell C3, a detailed comparison was given between FE analyses with several varieties of imperfection signature, as shown in Table 2.2: the mean imperfection signature of the three cylindrical shells C1-C3, the mean plus one standard deviation, the mean minus one standard deviation, and the as-measured signature. With a range of normalized buckling loads from approximately 0.85 to 0.95, the sensitivity of these cylindrical shells to varying imperfection signatures was illustrated. The mean imperfection signature gave a slightly higher buckling load than the as-measured signature, while reducing the imperfection by one standard deviation increased the predicted buckling load. Conversely, increasing the imperfection signature by one standard deviation decreased the buckling load, which confirms the expectation that more geometric imperfection amplitude would lead to a lower buckling load. All results of the study are shown in Table 2.1. The resultant KDFs for the closest measured imperfection simulation were 0.92, 0.95, and 0.88 for C1, C2, and C3, respectively, while the experimental KDFs were 0.93, 0.88, and 0.82, respectively. This implies errors of -1%, 8%, and 7% on the buckling load predictions.

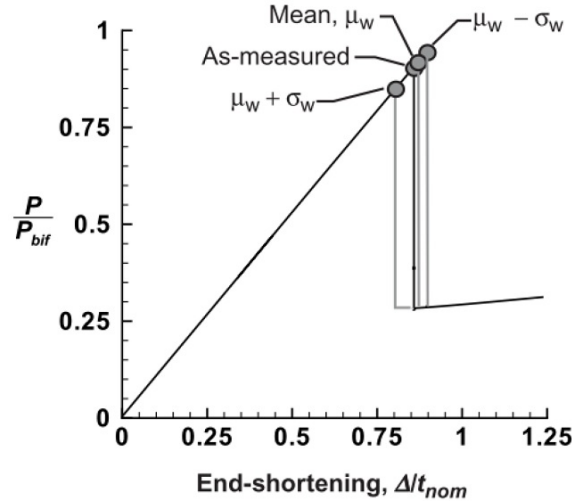


**Figure 2.2:** FEA results of Hilburger et al. for several varieties of geometric imperfection signature: mean of C1-C3, mean minus one standard deviation, mean plus one standard deviation, and C3 as-measured [17].

Shell	Predicted Buckling Loads, lbf						Experimental Buckling Load
	Perfect Shell	Measured Imperfection	Mean Imperfection, $\mu$	$\mu + \sigma$ Imperfection	$\mu - \sigma$ Imperfection	Linear-bifurcation-mode Imperfection, $w_0/l_{nom} = 0.5$	
C1	29900	29300	29000	27500	29850	17040	27788
C2	36300	34400	36170	34430	36930	14470	31924
C3	41500	38180	39100	36400	40200	21300	34082

**Table 2.1:** All results of Hilburger et al. [17].

Hühne et al. [27] combined measured imperfections in numerical models with the Single Per-

turbation Load Approach (SPLA) in 2008 for six composite cylindrical shells, which comprised four different designs (Z07 and Z08 were of the same design, Z09 was a second design, Z10 and Z11 were a third design, and Z12 was a fourth). The research was generally meant to propose new design guidelines for developing launch vehicle structures. The results compared the analysis of imperfect shells with the SPLA to experimental data and NASA SP-8007 guidelines. It was found that the  $N_1$  buckling load plateau of simulations for the six imperfect shells showed agreement with the  $N_1$  test data, as seen in Figure 2.3. Relative to the linearly obtained buckling loads for perfect cylindrical shells, the KDFs combining the SPLA and measured imperfections were approximately 0.55 for Z07 and Z08, 0.86 for Z09, 0.60 for Z10 and Z11, and 0.88 for Z12. The experimentally obtained KDFs were 0.52 (average of Z07 and Z08), 0.82 (Z09), 0.56 (average of Z10 and Z11), and 0.79 (Z12). This implies errors between test and simulation of 5%, 4%, 7%, and 11%, respectively for the aforementioned sets of cylindrical shells. However no comparison to SPLA models *without* imperfections was given. Thus, it cannot be concluded from this publication how much the measured imperfections in the models influenced the simulated  $N_1$  loads.

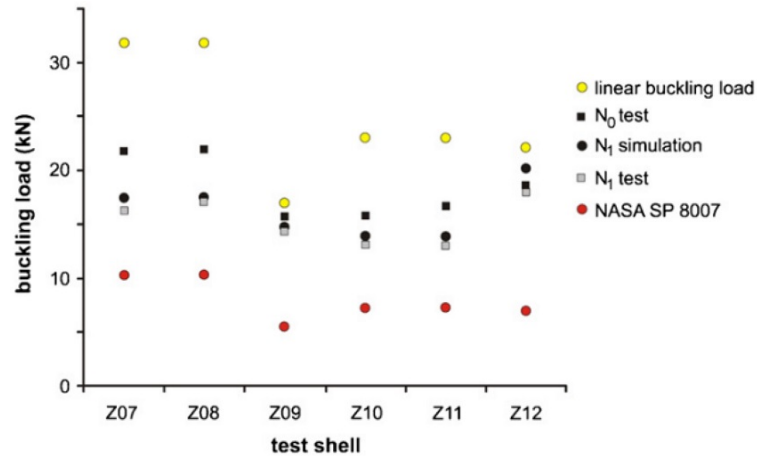


**Figure 2.3:** Results of Hühne et al. for six composite cylindrical shells' experimental SPLA tests and SPLA simulations with the inclusion of measured imperfections [27].

Between 2010 and 2011 researchers at the European Space Agency (ESA), the German Aerospace Center (DLR), and the University of Innsbruck studied a set of 10 solid laminate cylindrical shells. This research spawned three publications in which measured imperfections were related back to experimental results [28, 29, 30]. In the first article from Degenhardt et al. [28], models with mid-surface imperfections and thickness imperfections in combination and individually were created. The authors used the classical buckling load of 31.3 kN as the basis for KDFs rather than the higher simulated buckling load of 38.2 kN from geometrically perfect cylindrical shells, noting that the difference is due to the clamped edge condition in the model versus the classical buckling load which accounts only for simply supported edges. Here, the KDF of each basis is given in the format  $KDF_{classical} (KDF_{FEA,ideal})$ . The mean of the experimental buckling loads from the 10 specimens, which ranged from 21.3 kN to 25.7 kN, was 23.6 kN. This translated to average resultant experimental KDFs of 0.75 (0.62). The authors only published data on the numerical models of cylindrical shell Z26 (see Figure 2.4), which featured an experimental buckling load of 22.43 kN, for resultant experimental KDFs of 0.72 (0.59). Resultant KDFs from the models with only thickness imperfections, only geo-

metric imperfections, and both geometric and thickness imperfections were respectively 1.16 (0.95), 1.05 (0.86), and 1.00 (0.82), which translate to relatively large errors of 62%, 46%, and 39% respectively. The authors suggested that inhomogeneous material properties in the specimen and loading imperfections were responsible for the discrepancy, and later turned to stochastic methods to attempt to explain the difference. Despite this, all experimental and numerical KDFs were well above the SP-8007 KDF of 0.32.

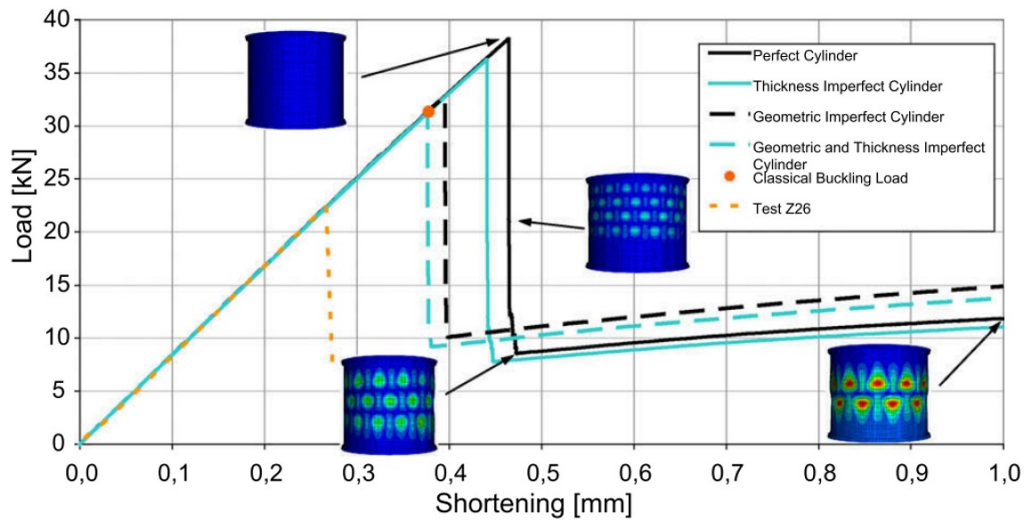


**Figure 2.4:** Results of Degenhardt et al. for cylindrical shell Z26 simulations and experiment [28].

Broggi et al. [30] in a second study incorporated fiber volume fraction (FVF) variances into measured imperfection models. Notably, these FVF imperfections were derived from measured variations in thickness; the authors attributed variations from the nominal thickness entirely to changes in resin content, rather than having a proportional increase in fiber content. This was a sensible assumption, because during the manufacturing process of composites, uncured resin is able to relocate with greater ease than fibers. Thus, the absolute amount of fiber in a given area should remain relatively constant. In conjunction with observed thickness variations, this means that the FVF, a relative quantity, should vary between areas of different thickness. The results of their study are shown in Figure 2.5. For cylindrical shell Z26, the FVF-variation-inclusive model predicted a buckling load of approximately 32 kN, slightly farther from the experimental result than Degenhardt et al. [28] simulated with measured imperfections only. Consequently the corresponding KDFs were 1.02 (0.84), for an approximately 43% error. When assessing the 10 cylindrical shells in aggregate, the average of the FVF-variation-inclusive models predicted a buckling load of approximately 31.2 kN, resulting in 1.00 (0.82) KDFs (which was incidentally the same as the Z26 mid-surface with thickness imperfection model of Degenhardt et al. [28]), whereas the mean experimental buckling load was 23.6 kN.

The third publication of the set, authored by Broggi and Schuëller [29], built upon the above research by further incorporating ply-gap imperfections into numerical models with geometric and thickness imperfections. These ply gaps and thickness imperfections were modelled using the “moving window averaging technique”. This method effectively recomputed the ABD matrix of small sub-sections (windows) of the FE model using thickness data that had been

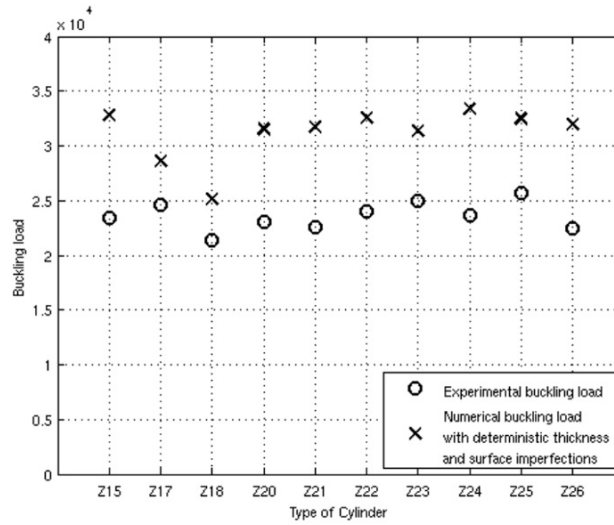


**Figure 2.5:** Results of Broggi et al. for 10 cylindrical shell models with measured imperfections, thickness imperfections, and fiber volume fraction fluctuations, compared with experimental data [30].

determined from ply gaps. The average simulated buckling load of the 10 models including geometric imperfections, thickness imperfections, and ply gaps was 30.8 kN, for resultant KDFs of 0.98 (0.81). For a direct comparison with cylindrical shell Z26 from the study of Degenhardt et al. [28], the incorporation of ply gaps into the numerical model actually resulted in slightly worse buckling load prediction of 31.6 kN, with resultant KDFs of 1.01 (0.83).

In 2013, Wu et al. [31] researched the impact of geometric imperfections on the buckling behavior on two variable stiffness solid composite cylindrical shells and additionally accounted for thickness variations due to overlapping fiber tows caused by the filament winding manufacturing process. This study was unusual in that the experimental buckling loads of both Shells A and B were *higher* than the buckling loads predicted by perfect models. Using the latter set of values as the baseline reference for the denominator in the KDF calculation, their experimental results imply KDFs of 1.08 and 1.14, respectively. Models of Shells A and B with their imperfections resulted KDFs of 1.01 and 0.98, respectively, which correspond to errors of -7% and -14% relative to the experimental KDFs. The authors speculated that the variably stiff nature of the shells caused this imperfection insensitivity, although it was suggested that further exploration was needed for definitive conclusions.

Arbelo et al. [32], studied measured geometric and thickness imperfections individually and in combination for the test cylindrical shell Z15, along with geometric imperfections for a second cylindrical shell Z33. Models with only geometric imperfections yielded KDFs of 0.837 and 0.72 for Z15 and Z33, respectively, which corresponded to errors of 13% and -17% with respect to the experimental KDFs of 0.74 and 0.87. For Z15, thickness imperfections alone gave a numerical KDF of 0.97, for an error of 32%. The consideration of both geometric and thickness imperfections very slightly improved the FE-predicted KDF to 0.836 relative to isolated geometric imperfections. Comparing solely geometric imperfections for Z15 and Z33, it is clear that those had a greater impact on the buckling load of Z33. NASA SP-8007 guidelines were overly conservative relative to the experimental results of both cylindrical

shells, as design KDFs of 0.31 for Z15 and 0.48 for Z33 were prescribed.

As part of the German LuFo program, Schillo et al. [33] studied the effects of combinations of measured geometric imperfections, layup variations, and load imperfections in four FE models of two filament-wound composite cylindrical shells in 2015. Photogrammetry was used to measure the geometry of the cylindrical shell, and Fourier analysis was further employed on this measurement data to obtain a representative mid-surface for implementation in the models. Additionally, the researchers used microscopy to investigate the as-manufactured nature of the layup. Thus, an “as-built” set of material properties were derived from analyzing voids and resin-rich areas, rather than simply basing the models’ material properties on the nominal material data. For the 11 cylindrical shells tested, load imperfections were detected via the test setup, and they were described as most likely being caused by tolerances of holes in the attachment rings that linked the test specimens to the Hexapod test equipment. The experimental buckling loads are compared with results of four varieties of numerical models in Figure 2.6 containing: (1) geometric and load imperfections; (2) geometric imperfections with a load imperfection and the as-built layup; (3) geometric imperfections only; and (4) a load imperfection only. The average resultant KDFs for each of the categories one through four were 0.565, 0.57, 0.67 and 0.58, respectively. Given an experimental mean KDF of 0.56, the corresponding differences between the numerical models and the mean experimental KDFs were 1%, 2%, 19%, and 4%, respectively. This clearly illustrates the significance that loading imperfections applied in mutually orthogonal directions to the cylindrical shells’ axes can have on the buckling behavior (see Figure 2.7). These loading imperfections  $F_x$  and  $F_y$  resulted in an average 3.1 kN shear load, which itself is approximately 5% of the mean buckling load. By contrast, the measured imperfection appears to have had about a fifth of the impact on the buckling load as the loading imperfection did. The orthotropic NASA SP-8007 KDF for the same cylindrical shell models was 0.54. So, unlike other studies in which the SP-8007 KDF appears to be overly conservative, it was not the case here, likely due to the loading imperfections; it is possible that without the presence of such significant shear loads, this may not have been the result.

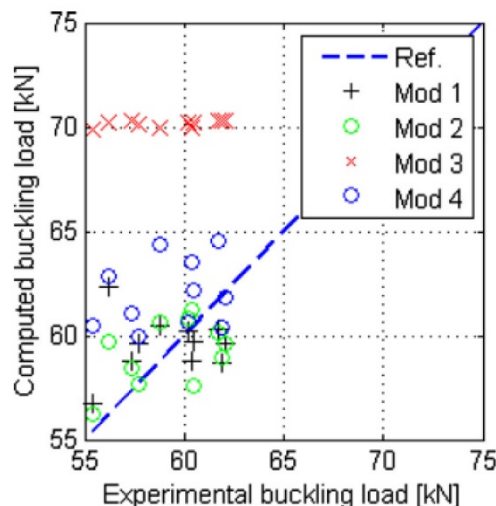


**Figure 2.6:** Numerical versus experimental results for four model variations of Schillo et al. [33].

In a joint study between researchers at the University of Bristol and NASA in 2015, White

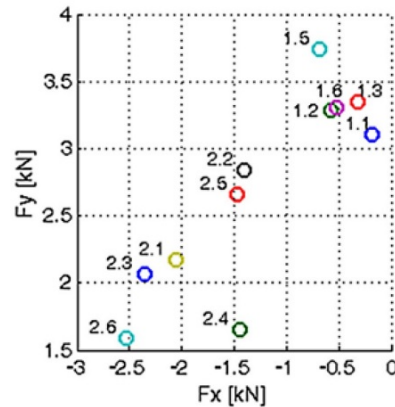


**Figure 2.7:** Measured loading imperfections resulted in net shear, shown above at the point of buckling [33].

et al. [34] investigated the effects of modeling variable stiffness solid composite cylindrical shells with imperfections. Due to the variable tow angles of fibers, individual elements in the model required their own material properties (e.g. orientation angle). Both thickness imperfections and geometric imperfections were incorporated into the models. Additionally, while the authors did not model the epoxy potting in the full FE models, they incorporated the effective stiffness of the potting into the full models by first making sub-models of the shell boundary areas with potting (as shown in Figure 2.8) and calculating the effective stiffness of the end sections via static analyses. Multiple encasement stiffness ratios  $\eta$  were obtained for each cylindrical shell's sub-model due to the fact that different lamina stacking sequences were present at the end of the cylindrical shell (as a result of fiber overlaps). Thus the buckling sensitivity responses of the full model with varying  $\eta$  are shown in Figure 2.9. It is apparent however that altering the stiffness of the encased elements did not ultimately have a dramatic impact on the buckling loads obtained. Overall, the best numerical KDF for Shell A was within -1% of the experimental KDF, while that of Shell B was within -7% agreement with the experimental result.

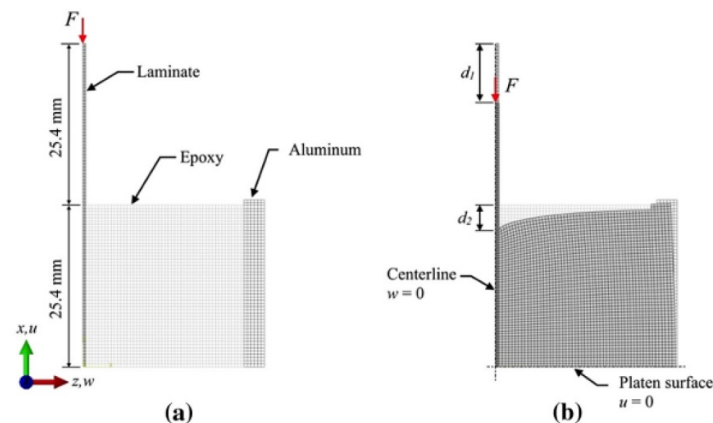


**Figure 2.8:** Sub-models from which effective stiffness of encased regions of the cylindrical shells as determined by White et al. [34].

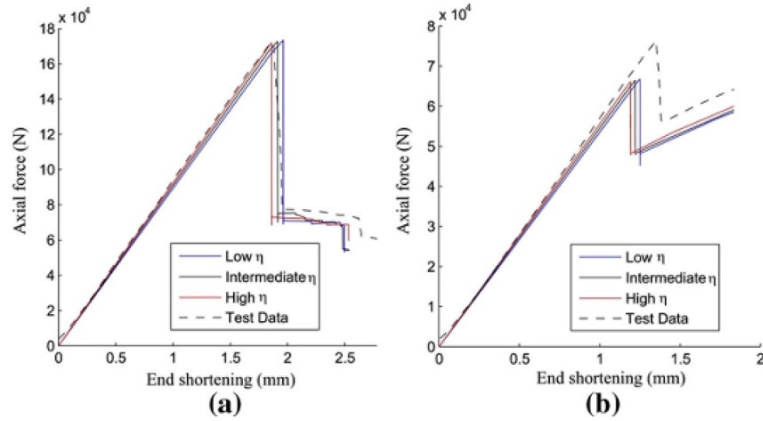


**Figure 2.9:** The effect of altering encasement sensitivity on the buckling curves of two variable stiffness cylindrical shells, with measured geometric and thickness imperfections included [34].

Continuing off of research from the DESICOS project, Khakimova et al. [35] in 2017 investigated the effects of incorporating individual and combinations of imperfections into solid composite cylindrical shell models in order to determine how the accuracy of buckling load and KDF predictions were affected. The types of imperfections considered were geometric imperfections, thickness imperfections via ultrasonic measurement, and fiber volume fraction variations. Additionally, the authors analyzed a model incorporating all imperfection types and potting on the cylindrical shell ends, which helps to facilitate load transfer. For the specimen Z36, the load-displacement curve is shown in Figure 2.10. It can be seen clearly that the inclusion of more imperfection types reduced the difference in FEA buckling load relative to the experimental buckling load; for cylindrical shell Z36, the closest FEA prediction yielded a KDF of 0.8, whereas the actual experimental test gave 0.71. Similarly, for a second specimen investigated, Z37, the model with all imperfections gave a KDF of 0.79, while the test gave 0.65. The corresponding errors between these numerical and experimental KDFs for Z36 and Z37 are 13% and 22%, respectively. The authors attributed these differences to loading asymmetries in the test setup, which were observed via strain gauge readings from the cylindrical shells' surfaces.

Schultz et al. [36] of NASA studied the buckling behavior of a large-scale composite honeycomb-core sandwich cylindrical shell CTA8.1 in 2018 via FEA and experimental testing. Using structured light scanning to measure the inner and outer molds, the authors were able to derive both mid-surface imperfection (via averaging) and thickness imperfection (via subtraction) information for incorporation into FE models. Because shell elements of two-dimensional geometry were used, imperfections were implemented via perturbation of node locations from their idealized positions to the imperfect mid-surface locations determined from the structured light scanning. Because the authors furthermore attributed thickness variations in the cylindrical shell to changes in the core thickness, the thickness imperfection was implemented by varying the core thickness in each element via the composite layup properties. In addition to modeling the cylindrical shell, the authors also modeled the rest of the test setup, which included load-orientation lines and assemblies on the top and bottom of the cylindrical shell, each consisting of an attachment ring, a transition section, load struts, and a load spider (in order of proximity to CTA8.1). The pre-test FE analysis buckling load yielded excellent

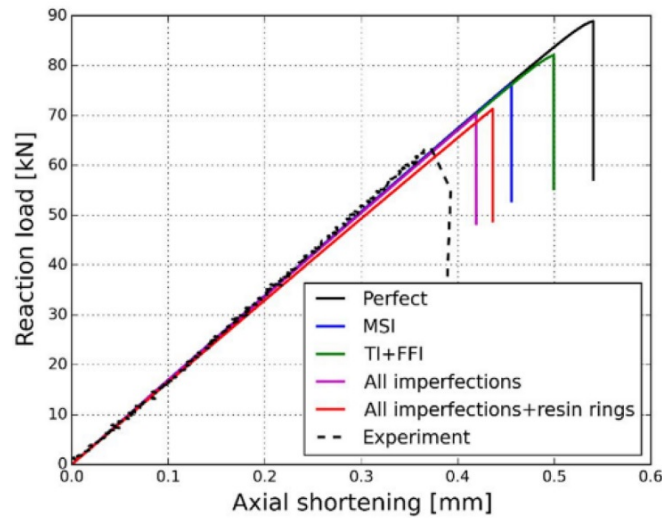


**Figure 2.10:** The effect of incorporating various imperfections on FE buckling analyses [35].

agreement with the experimental test result: 865 kip and 857 kip, respectively, for KDFs of 0.88 and 0.87, which translates to a 0.9% over-prediction. A post-test simulation was also conducted to account for material nonlinearities, which were measured from destructively removed specimens of CTA8.1. Incorporation of the nonlinear material response also gave good agreement with the experimental result, with an FEA buckling load of 845kip, which corresponds to an error of -1.4%. The authors noted that while this slightly increased discrepancy in buckling load was present, the nonlinear material model better reflected the pre-buckling load-displacement curve of the experiment. Noting that the NASA SP-8007 KDF for CTA8.1 was 0.61, the authors concluded that the guidelines may be overly conservative.

In 2019, Labans and Bisagni [37] sought to investigate the numerical and experimental buckling behavior of a variable stiffness solid composite cylindrical shell and a constant stiffness quasi-isotropic composite cylindrical shell with measured geometric imperfections. One cylindrical shell of each category was manufactured, and the inner and outer surfaces of the shells were measured via laser and digital image correlation (DIC), respectively. These imperfections were implemented into numerical models in Abaqus, and dynamic implicit analyses for each cylindrical shell were conducted. Additionally, eigenvalue analysis was performed on geometrically perfect cylindrical shells in order to calculate KDFs from each analysis and the experiments. For the highest resolution variable stiffness model (in which five separate zones were discretized from continuously varying tow angles), the KDF was 0.77, while KDFs of 0.76 and 0.81 were found for laser-measured and DIC-measured imperfection models of the constant stiffness cylindrical shell, respectively. In comparison, the experimentally obtained KDFs were 0.80 for the variable stiffness cylindrical shell and 0.72 for the constant stiffness cylindrical shell, indicating that numerical models were able to predict the actual buckling load within 5% for both cylindrical shells (in the case of the DIC-measured constant stiffness cylindrical shell, the prediction was 12%). While the authors did not calculate a NASA SP-8007 KDF for the constant stiffness cylindrical shell, a 0.44 KDF could be calculated from the geometric, material, and layup information provided.

## 2.2 Comparison of Data from Simulation and Experiments

Table 2.2 gives an overview of resultant simulated and experimental KDFs for unstiffened composite cylindrical shells found in the literature. The table is sorted in reverse chronological order. The number of the reference is given in the first column, and the second column gives the year of publication. The third column describes the type of material and construction with the following designations: “CS” for solid composite, “CSV” for solid composite with variable stiffness, and “CSW” for composite sandwich.

Ref	Year	Type	Specimen or Model Variant	FEA Imperfection Type				KDF			Error % FEA	r/t
				Geo	Thk	Mat	Other	Exp.	FEA	SP-8007		
[37]	2019	CSV	1 (5-zone model)	x				0.80	0.77	N/A	-4	208
		CS	2 (FEA from laser imperfection)	x				0.72	0.76	0.44	5	
			2 (FEA from DIC imperfection)	x					0.81		12	
[36]	2018	CSW	Pre-test FEA	x	x			0.87	0.88	0.61	0.9	149
			Post-test FEA	x	x				0.86		-1.4	
[35]	2017	CS	Z36	x				0.71	0.85	0.31	21	533
				x	x	FVF			0.80		13	
			Z37	x				0.65	0.86		32	
				x	x	FVF			0.79		22	
[34]	2015	CSV	Shell A	x	x			1.00	1.00	N/A	-1	163
			Shell B	x	x			1.07	0.99		-7	209
[33]	2015	CS	FEA 1	x			load	0.56	0.56	0.54	1	142
			FEA 2	x		x	load		0.57		2	
			FEA 3	x					0.67		19	
			FEA 4				load		0.58		4	
[32]	2014	CS	Z15	x	x			0.74	0.84	0.31	13	540
				x	x				0.97		32	
			Z33	x				0.87	0.72		0.48	
[31]	2013	CSV	Shell A	x	x			1.08	1.01	N/A	-7	188
			Shell B	x	x			1.14	0.98		-14	
[29]	2011	CS	Z15, Z17, Z18, Z20-Z26	x	x		PG	0.75	0.98	0.32	41	1000
[30]	2011			x	x	FVF			1.00		31	
			[28]	2010	Z26	x	x	FVF			1.02	
x								1.05	46			
[27]	2008	CS	Z07, Z08 (avg)	x			SPLA	0.52	0.55	0.31	5	500
			Z09	x			SPLA	0.82	0.86	0.31	4	
			Z10, Z11 (avg)	x			SPLA	0.56	0.60	0.30	7	
			Z12	x			SPLA	0.79	0.88	0.31	11	
			C1 vs best FEA	x	x	x		0.93	0.92	0.47	-1	
[17]	2004	CS	C2 vs best FEA	x	x	x		0.88	0.95	0.47	8	200
			C3 vs best FEA	x	x	x		0.82	0.88	0.46	7	
			Z32	x				0.87	0.98	0.48	13	
[25]	2002	CS	Z33	x				0.90	0.73	0.48	-19	200
			Dynamic	x				0.68	0.83	0.45	21	
[24]	2000	CS	Riks	x				0.68	0.78	0.45	14	265

**Table 2.2:** Comparison of findings from literature in which experimental results were compared specifically with FEA that included measured imperfections.

The fourth column specifies either the name of the specimen and/or the variant of the FE model used as referred to in the given publication. In some cases of multiple shells having the same nominal specifications, the data is averaged and noted with “avg”. The imperfection types stated indicate which imperfections were incorporated into the FE models, and they are given in the fifth through eighth columns: geometric, thickness, material, and other, respectively. Specific material imperfection abbreviations are: “FVF” for fiber volume fraction and “PG” for ply gap.

The resultant experimental and FEA KDFs in columns nine and ten represent the experimental or FEA buckling load divided a reference buckling load. In some cases where these KDFs were not stated explicitly, they were calculated by the present author by dividing the experimentally or numerically obtained buckling load by the reference buckling load of the

imperfection-free shell provided in the publication. Typically this reference load was the analytical buckling load, although occasionally linear eigenvalue analysis buckling loads were reported. If both were provided in a study without a KDF given, the greater of the two values was used as the reference in the present KDF calculation.

In the eleventh column, the NASA SP-8007 design KDFs were either taken from the literature when presented by the authors, or calculated by the present author by using the provided geometry and material specifications of the given literature and the relevant equations of NASA SP-8007 [5]. Error percentages found in the twelfth column were obtained using the experimentally obtained KDF as the reference. Finally, the last column gives the radius-to-thickness ratio ( $r/t$ ) of the cylindrical shell or set thereof.

From Table 2.2, it can be seen that finite element models with directly measured imperfections are capable of predicting the experimental buckling loads with a high degree of accuracy in some cases. However, several studies have noted that other factors such as experimental loading imperfections can reduce the accuracy of such predictions by large margins.

Figure 2.11 shows data of the experimental KDFs from the studies shown in Table 2.2 plotted against the radius-to-thickness ratio. The light grey shapes in the background of Figure 2.11 represent data points for composite cylindrical shells aggregated in 2012 by Takano [38], who comprehensively studied available data to propose a new set of statically based knockdown factors for composite cylindrical shells. Figure 2.11 also shows the classical NASA SP-8007 KDF prescription, which is a function of a shell's radius-to-thickness ratio. (For composite shells, an equivalent radius-to-thickness ratio is calculated via constants of the ABD matrix.)

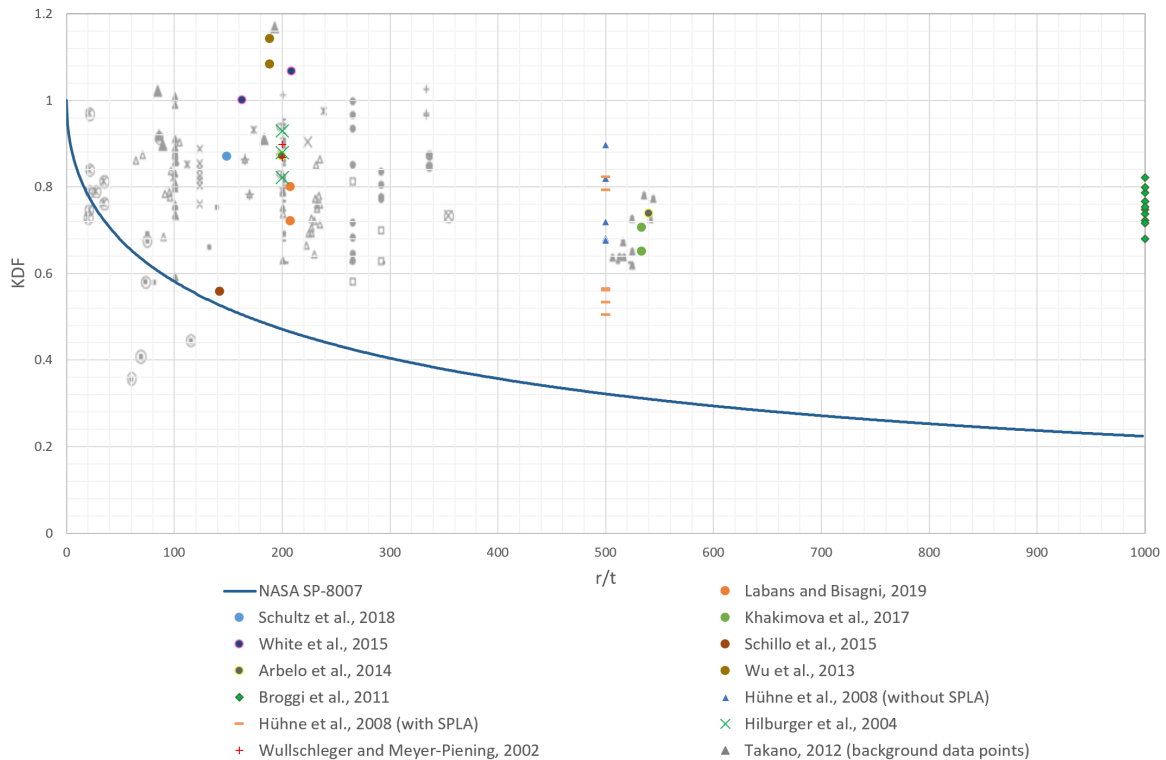


**Figure 2.11:** KDFs aggregated by the present author and overlaid with the compilation of Takano [38], shown in light grey.

## 2.3 Modeling and Analysis Considerations

This section details specific practices and trends that were found in the literature with regard to finite element modeling and simulation of cylindrical shell buckling. Common themes were extracted and are summarized here.

### 2.3.1 Imperfection Implementation

#### Geometric Imperfections

It is often not the case that the geometric imperfection measurement data points correspond precisely to the regularly spaced axial and circumferential grid coordinates that might be found in a finite element model of a shell containing no imperfections. Thus, some form of interpolation or curve fitting must be performed in order to translate the measured imperfection data into the finite element mesh.

Linear interpolation is a simple way of translating measurement data to the FE model. Several have employed this method including Hilburger and Starnes Jr. [6, 39], Meyer-Piening et al. [40], Wullschleger and Meyer-Piening [25], and Hilburger [41]. It is surmised that several previously mentioned studies from the previous sections in which interpolation methods were not specified may have also used linear interpolation due to its simplicity, although this is not certain.

Castro et al. [20] and Wang et al. [42] used inverse distance weighted interpolation to translate measurement data into FE models. For a given mesh location (defined as a circumferential and axial coordinate set), the interpolated radius is calculated based on a weighted mean of the experimentally measured imperfection radii. The points to be included in an interpolation to an individual mesh point may be limited to either a fixed number of nearest neighboring points or all points within a threshold distance. The weighting term for a given measured-point/mesh-point pair is the inverse of Euclidean distance of the “unwrapped” cylindrical surface between the point pairs, which is then raised to a specified power. It is thought that inverse distance weighted interpolation can help to reduce noise obtained from the measurement system and provide a smoother surface [42].

Fourier analysis differs from the above techniques in that it is not an interpolation method; rather, it is a type of curve-fitting. Hilburger [41] used Fourier analysis to generate mean imperfection signatures of three cylindrical shells based upon separate Fourier analysis of each. It is thought to be useful for comparing the frequency in occurrence of different magnitudes of variances in shape, which may be characteristic to the given manufacturing technique. Additionally, it can be used in stochastic methods to generate imperfection patterns. Others who have employed this interpolation are Schillo et al. [33], Bisagni and Alfano [43], Wagner and Hühne [44], and Wang et al. [42].

The method chosen to translate geometric imperfection data into the mesh may have some influence on the numerically obtained buckling load, although this has not been studied extensively for composite cylindrical shells. However, Wang et al. [42] did compare Fourier analysis and inverse weighted distance interpolation for metallic cylindrical shells; this resulted in only a small difference in numerical buckling load.

### Thickness Variations

Thickness imperfection may be calculated or measured directly. In the case of the former, measurement of both the inner and outer surfaces are required, and thus subtraction of the inner surface from the outer surface will lead to a thickness profile of a shell, as for example Schultz et al. [36] did. Alternately, direct measurement may be conducted on test specimens, such as Khakimova et al. [35] who opted to use ultrasonic testing for thickness measurement. Once obtained, thickness imperfections are implemented into models with two-dimensional shell elements on an element-by-element basis. If solid or continuum elements are used, the thickness would already be implied by the node locations if inner and outer surface measurements were taken into account in the FE models. Conversely, if outer surface and thickness measurements are taken, the inner surface of the FE model would be implied by the subtraction of the thickness from the outer surface.

### Material Imperfections

Several studies presented have used thickness imperfection data to derive positional variances in fiber volume fraction, a form of material imperfection, from nominal values [30, 35, 41, 45]. All such studies utilized the assumption that variations in thickness were due to changes in resin content, while absolute fiber volume remained constant. In the cases of Broggi et al. [30] and Khakimova et al. [35], the recalculation of the lamina properties were obtained via Chamis's corrected composition rule [46]. In contrast, Hilburger [41] used the rule of mixtures to recalculate ply properties. It is not expected by the present author that these varieties of calculation would lead to drastic differences in buckling behavior in models compared to one another; however, this has not been demonstrated explicitly in the literature.

Another aspect of material variation implementation relates to the resolution or fidelity at which material changes are reproduced in models. As a basis for comparison, geometric imperfections can be reproduced at every node in model, and thus the as-measured geometry of a cylindrical shell has the resolution of the finite element mesh. To have a similar resolution with material properties that are assigned to finite elements, every element could ostensibly have a different material property, leading to finite element model input files containing tens or hundreds of thousands of material property sets. Hilburger did just that by creating updated ply properties via programming subroutines on an element-by-element basis. On the other hand, Khakimova et al., noting the aforementioned issue, created a set of 100 discrete sets of lamina properties (corresponding to 100 increments of thickness variations from minimum to maximum), and then assigned the constituent material of each element's plies to the nearest corresponding set of material properties.

### Additional Notes

Unlike many measured imperfection approach studies, Hilburger and Starnes Jr. [26] produced a window of buckling behavior predictions rather than single predictions of combinations of imperfections. Combinatorial analysis was used to create high and low bounds of the ranges. In practice, this approach to characterizing uncertainty in model parameters could be applied to any combination of properties. The fact that different measurement systems in the work

of Labans and Bisagni [37] produced different FEM buckling load predictions suggests that it may be useful to produce a range of predictions as Hilburger and Starnes Jr. [26] did.

### 2.3.2 Modeling Experimental Setups

#### Potting

Some researchers have included test articles' potting in finite element models, such as Degenhardt et al. [28]. As an alternative strategy to capture the effect of potting on the encased shell acreage without actually modeling it, some have opted to measure the equivalent stiffness of the encased areas of the cylindrical shells via sub-model finite element analyses, as shown in Figure 2.8. Then resultant properties were incorporated back into the full model in those localized areas, as Hilburger and Starnes Jr. [26], White et al. [34], and Hilburger [41] have done. In another implementation, Kepple et al. [11, 47] used clamped boundary conditions applied to all nodes along the top and bottom 20 mm axial length of the cylindrical shell to simulate the effect of resin encasing that area, without actually modeling the encasement itself or performing an equivalent stiffness sub-analysis.

#### Test Setup

Some numerical models have included the entire compression testing equipment setup [36, 48, 49], although this is not commonplace. Figure 2.12 shows such a model of full testing equipment. Cha and Schultz [48] investigated the effect of modeling the test setup with perfect sandwich composite cylindrical shell in comparison with modeling the perfect cylindrical shell with potting only. As seen in Figure 2.13, inclusion of the test setup yielded a slightly higher buckling load than modeling the cylindrical shell only.

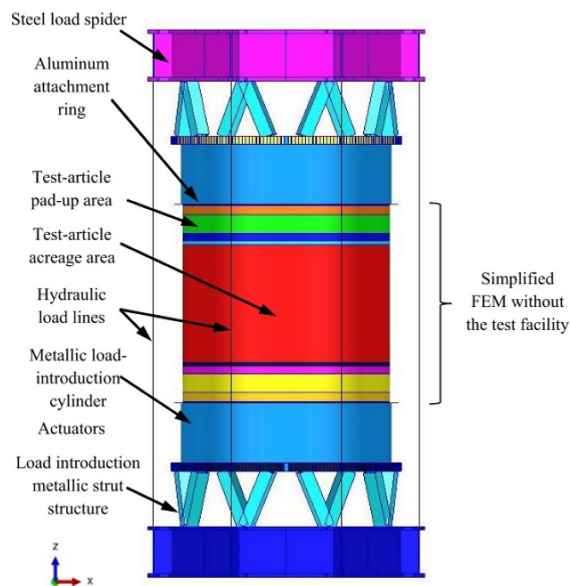
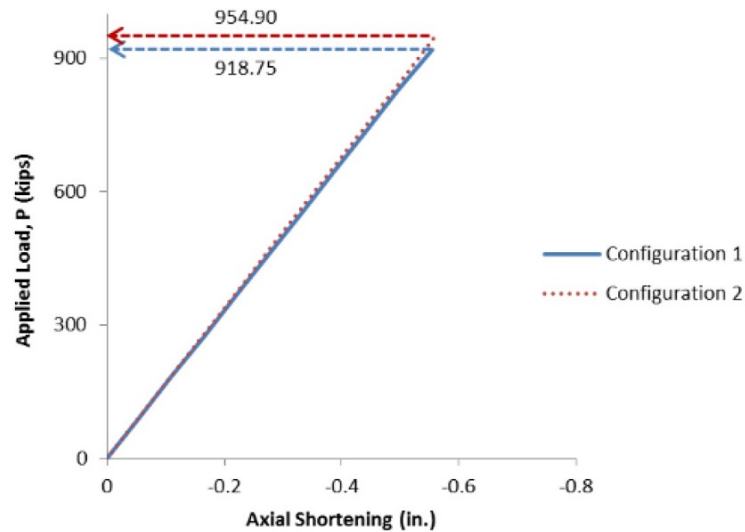


Figure 2.12: Model of the full test setup by Przekop et al. [49].



**Figure 2.13:** Comparison of nonlinear analysis of a perfect sandwich cylindrical shell with potted regions only (Configuration 1) against the same cylindrical shell with modeled test setup (Configuration 2) from Cha and Schultz [48].

### 2.3.3 Additional Modeling Details

#### Element Choice

The S4R four-node reduced integration shell element of the Abaqus FEA solver has been featured prominently in unstiffened shell buckling studies of the past 10 years [12, 16, 19, 20, 29, 30, 32, 33, 34, 37, 42, 43, 44, 50, 51, 52, 53, 54] as well as the S4 four-node shell element [10, 36, 48]. These elements are surface-based (i.e. two-dimensional) and do not account for transverse shear, unlike the SC8R eight-node continuum shell element of Abaqus [55], which was only found to have been studied by van Dooren in the context of composite cylindrical shell buckling [56].

#### Boundary Conditions and Constraints

In situations where either only the cylindrical shell is modeled or the shell with potting is modeled (rather than the full test setup), reference nodes are typically created at points coincident with the cylindrical shell's nominal axis and planes of the upper and lower edges [31, 33]. From here, nodes along the shell's edges are then constrained to the respective reference point. Corresponding to the non-moving boundary of the experimental setup, the associated reference point would then be clamped. Similarly, the side of the cylindrical shell corresponding to location of imposed displacement be constrained to only move along the shell's axial direction.

#### Analysis Type

Implicit and explicit numerical time integration schemes each offer advantages over the other, which result in certain trade-offs. Implicit analysis solves a system of equations using in-

formation from the current and next time step simultaneously. This requires large matrix inversion for every increment, which can be computationally expensive. Explicit analysis does not have this constraint, only solving one increment at a time, and then moving on to the next. However, this requires much smaller time increments than implicit analysis both because the time step must be less than the time it takes a sound wave to pass across an element, as well as to avoid error accumulating over large periods of simulation. The advantage of explicit analysis is that it can capture the inertial effects present in models. Whether or not axial compression buckling simulations require these inertial effects to be included, however, is not entirely straightforward for investigation of pre- and initial buckling behavior (in contrast to post-buckling). This is because end-shortening rates used in experiments are on the order of millimeters per minute or less, whereas the overall scale of the cylindrical shells is often on the order of meters. Some examples of references using implicit analysis are [11, 18, 28, 32, 33, 47, 54, 57]. Others have used explicit: [16, 19, 24, 27, 52]. In summary, there is no consistently preferred method throughout the literature.



# Simplified Shell Description & Modeling

The equivalent simplified laboratory-scale used in preliminary analyses is introduced in this chapter. The shell geometry, material properties, and layup are presented. The shell's analytical buckling load and corresponding knockdown factor per NASA SP-8007, which thereby pertain to NDL-1, are introduced. Details of the simplified shell's finite element model are then provided.

### 3.1 Geometry, Material, and Layup

The simplified shell features a mid-surface radius of 400 mm and a height of 1120 mm, as summarized in Table 3.1.

Mid-Surface Radius [mm]	Height [mm]
400	1120

**Table 3.1:** Geometry of the simplified laboratory-scale cylindrical shell.

The material properties of Hexcel's preimpregnated carbon-fiber-epoxy composite IM7-8552 were used. The elastic properties, density, and ply thicknesses of Table 3.2 were taken from Clarkson [58]. These are henceforth referred to as the "nominal" material properties. The failure stresses of IM7-8552 were also taken from Clarkson and are specified in Table 3.3. The fiber-direction failure strains were calculated by dividing the failure stresses by  $E_{11}$ . Transverse failure strains were obtained by dividing the transverse failure stresses by  $E_{22}$ . Similarly, the shear failure strain was taken as the shear failure stress divided by  $G_{12}$ .

The layup of the simplified shell is  $[(23/0/-23)_{S4}]$ . Figure 3.1 shows the orientation system of the plies with respect to the outside of the shell and its axis of rotation.

$E_{11}$ [GPa]	$E_{22}$ [GPa]	$G_{12}$ [GPa]	$G_{13}$ [GPa]	$G_{23}$ [GPa]	$\nu_{12}$ [-]	$\rho$ [g/cm <sup>3</sup> ]	Ply Thickness [mm]
140.9	9.72	4.69	4.69	3.58	0.356	1.58	0.175

**Table 3.2:** Nominal material properties of Hexcel IM7-8552 composite [58].

Direction	Failure Stress [MPa]	Failure Strain [ $\mu\epsilon$ ]
Fiber tensile	2212	15969
Fiber compressive	1731	12280
Transverse tensile	64	6584
Transverse compressive	286	29400
Shear	54	11520

**Table 3.3:** Failure stresses of Hexcel IM7-8552 composite from Clarkson [58] and calculated failure strains.

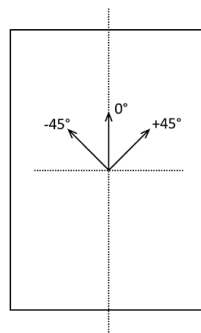


**Figure 3.1:** Ply rosette as viewed from the outside of the shell. The shell's axis is parallel with the 0° direction.

## 3.2 Analytical Buckling Load

The shell's 2271-kN analytical buckling load was computed by minimizing Equation 44 of NASA SP-8007 [5] with respect to the number of axial half waves  $m$  and circumferential full waves  $n$ . The knockdown factor prescribed by SP-8007 is determined according to its Equations 45 and 46. These results are shown in Table 3.4. The axial half-waves and circumferential full-waves correspond to the analytical buckling shape that provides the minimum strain energy state satisfying the equations.

Buckling Load		KDF	Axial Half-Waves	Circumferential Full-Waves
Analytical [kN]	Analytical with KDF [kN]			
2271	1338	0.59	9	0

**Table 3.4:** Buckling loads, knockdown factor, and mode shapes calculated according to NASA SP-8007 [5].

## 3.3 Finite Element Modeling

Abaqus 2017 was employed for all simulations in this report. The simplified shell was modeled in two ways: with the S4R four-node conventional shell element and with the SC8R eight-node continuum shell element [55]. The former is modeled with surface geometry and does not consider transverse shear, while the latter is modeled with solid geometry and does consider transverse shear. This was done to determine if the consideration of transverse shear compliance made substantial differences in the numerically obtained buckling loads with this particular laminate. With both element types, only one element through the thickness was used.

A model of the simplified shell without imperfections is presented in Figure 3.2. Upper and lower reference nodes were created at the center of the upper and lower edges, respectively. Nodes along models' upper edges were constrained to the upper reference nodes, and similarly all lower edge nodes were constrained to the lower reference nodes. Tie constraints were used, which have the effect of the making the slave nodes' (i.e. the edges) degrees of freedom take on the same translational and rotational displacement values as those of the corresponding master reference node. This was done to simplify both the application of boundary conditions to the shell models and to streamline simulation data post-processing; regarding the latter, the reaction force due to axial compression along the shell's edge was extracted from the reference node. (If no reference node had been used, the reaction force of each individual upper nodes would need to be summated to determine the total reaction load.) The lower reference node was clamped. The upper reference node's rotational degrees of freedom were constrained to zero, as were its X- and Y- translational degrees of freedom as indicated by the orientation system in Figure 3.2 (i.e. it was only free to move in the Z-direction).

The choice of mesh size was based on the findings of van Dooren [56] and the results of a convergence study. The latter was conducted with linear eigenvalue buckling analysis. A unit load was applied to the upper reference node in the axially compressive direction. The metric

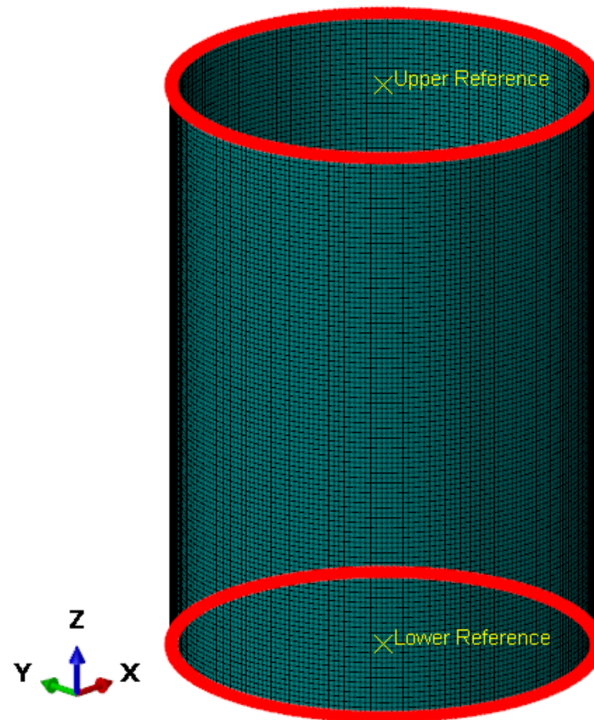


**Figure 3.2:** All nodes along the top and bottom edges (red) were constrained to a respective upper or lower reference node (yellow). (10-mesh shown.)

used for assessing convergence was the lowest eigenvalue buckling load. Results are shown in Figure 3.3. Considering both the convergence of this metric and the computational time in the same manner as Wang et al. [42], it was determined that a 10-mm mesh (corresponding to 28,336 elements in Figure 3.3) would be sufficient for conducting preliminary analyses with both element types. The computation time between the S4R and SC8R models were very similar, despite the fact that the latter contains double the number of nodes as the former. The reason is likely that S4R nodes have both translational and rotational degrees of freedom (for a total of six degrees of freedom per node), whereas SC8R nodes only have translational degrees of freedom. Thus, both the S4R and SC8R have the same number of degrees of freedom per element: 24. The models of each element appear to converge to approximately 2285 kN in Figure 3.3, whereas the analytical buckling load is 2271 kN. This slightly higher numerical analysis value was probably due to the fact that the models featured clamped boundary conditions, whereas the analytical solution is formulated with simply supported end conditions [5, 28].

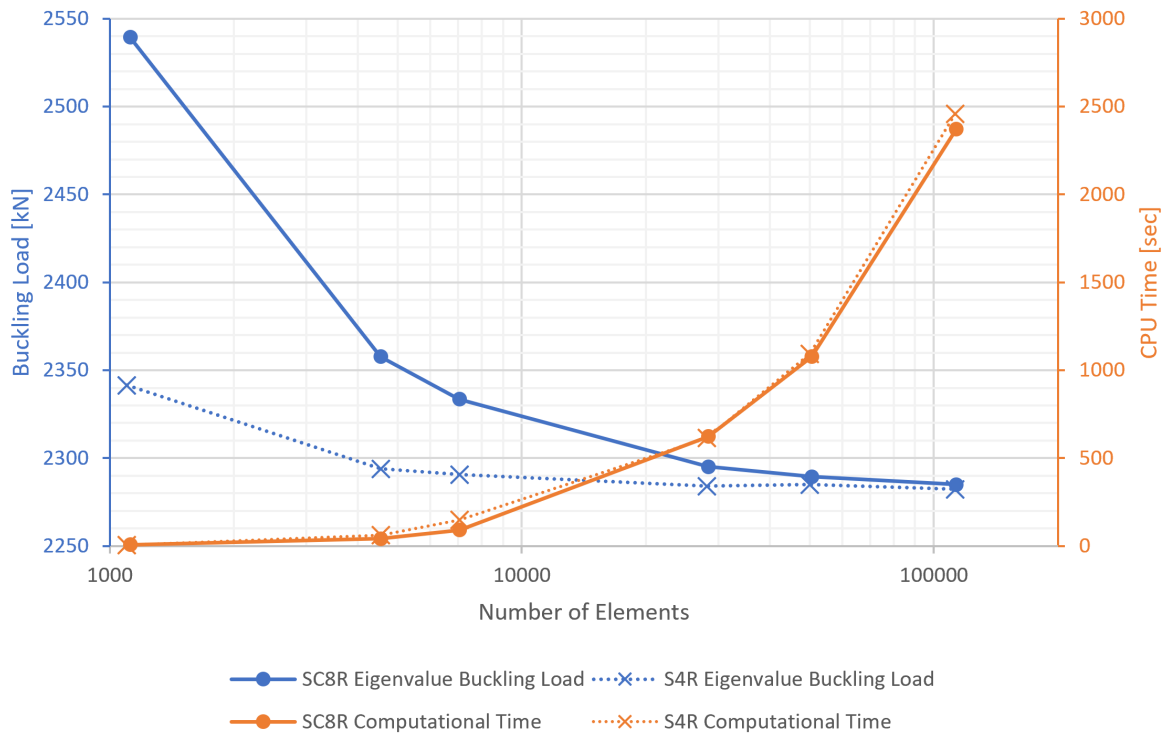


**Figure 3.3:** Convergence study of the lowest eigenvalue buckling load for S4R and SC8R shell models, with computational time indicated. From left to right, the data points correspond to mesh sizes of 50 mm, 25 mm, 20 mm, 10 mm, 7.5 mm, and 5 mm.



## Analyses of the Simplified Shell without Imperfections

Several analyses were performed on the simplified shell without imperfections to determine agreement with one another and the SP-8007 analytical buckling solution. Eigenvalue analyses were used to determine the expected buckling load and corresponding displacement (and thereby axial stiffness), along with potential buckling shapes. Linear static analysis was conducted to determine the axial stiffness of the shell. Finally, the results of nonlinear dynamic analysis are presented.

### 4.1 Eigenvalue Buckling Analyses

The results of eigenvalue buckling load and eigenvalue buckling displacement analyses are presented in Table 4.1. The lowest three eigenvalue buckling loads were taken from same simulations as the 10-mm mesh models from the convergence study found in Section 3.3. Eigenvalue buckling displacement analyses were performed via prescription of an axially compressive unit displacement to the S4R and SC8R models' upper reference nodes. This was done to determine the lowest displacement value corresponding to the shells' first three eigenmode buckling load values.

Element	Eigenmode 1		Eigenmode 2		Eigenmode 3		CPU Time	
	Disp. [mm]	Load [kN]	Disp. [mm]	Load [kN]	Disp. [mm]	Load [kN]	Disp. [s]	Load [s]
SC8R	2.373	2295	2.373	2295	2.375	2297	1107	1132
S4R	2.363	2284	2.363	2284	2.365	2286	1139	1117
Difference	-0.4%	-0.5%	-0.4%	-0.5%	-0.4%	-0.5%	2.9%	-1.3%

**Table 4.1:** Eigenvalue load and displacement analysis results for both elements types. The percentage difference is taken with respect to the SC8R element.

Both elements show good agreement in terms of load, displacement, and computational time. The first eigenmode buckling loads show good agreement with the NASA SP-8007 analytical load without imperfections: the SC8R model is 1% higher, and the S4R model is only 0.5% higher. As mentioned in Chapter 3, this is likely due to the clamped edge condition of the models versus the simply supported condition of the SP-8007 analytical solution. The axial stiffnesses of each model was calculated by dividing the lowest eigenvalue buckling load by the lowest eigenvalue buckling displacement. The SC8R and S4R models exhibited stiffnesses of 967.1 kN/mm and 966.6 kN/mm, respectively (agreement within 0.05%).

Figures 4.1 and 4.2 show the eigenmode buckling shapes for shell models with SC8R elements and S4R elements, respectively. These first three mode shapes show excellent agreement between the two element types. The number of axial half-waves (9) and circumferential full-waves (0) of the third eigenmode shape are in agreement with the analytical solution.

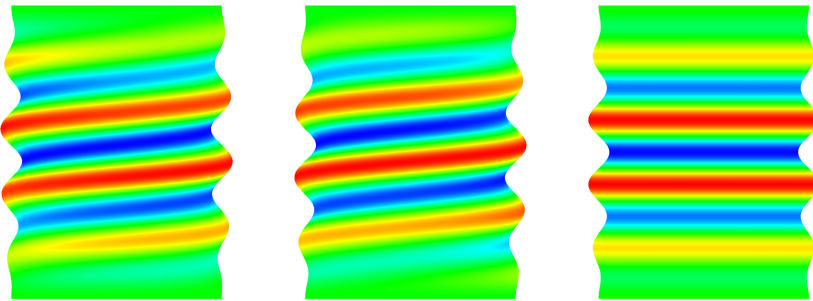


**Figure 4.1:** The first three eigenmode buckling shapes of the simplified shell modeled with SC8R elements with a 10-mm mesh. The amplitude of these shapes is equal to 100% the shell's 4.2-mm wall thickness, magnified 10x.

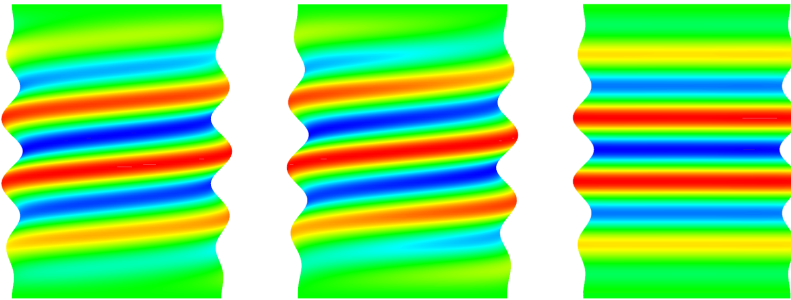


**Figure 4.2:** The first three eigenmode buckling shapes of the simplified shell modeled with S4R elements. The amplitude of these shapes is equal to 100% the shell's 4.2-mm wall thickness, magnified 10x.

## 4.2 Linear Static Analysis

Linear static analyses were used to check the stiffness of the shell models. To accomplish this, the lowest eigenmode buckling displacement values presented in Table 4.1 were prescribed to the upper reference node of the corresponding model in the axially compressive direction (2.373 mm for the SC8R model and 2.363 mm for the S4R model), and the reaction load at this node was requested as simulation output data. These results are shown in Table 4.2. The output loads, and thereby the computed axial stiffnesses, showed excellent agreement with one another and those obtained via eigenvalue analysis in Section 4.1.

Element	Displacement [mm]	Load [kN]	Axial Stiffness [kN/mm]
SC8R	2.373	2295	967.1
S4R	2.363	2284	966.6

**Table 4.2:** Linear static analysis results.

## 4.3 Nonlinear Dynamic Analysis

Nonlinear implicit dynamic analyses were used to investigate the buckling load of the shell without imperfections in response to dynamic loading. A displacement rate of 2 mm per second was applied to the upper reference node in the axially compressive direction. Simulation duration was determined by the amount of time required to reach 2.5 mm of displacement, slightly higher than the eigenvalue displacement of Section 4.1; this was to insure that buckling would occur. The buckling loads and displacements obtained from nonlinear analysis are indicated in Table 4.3 and show excellent agreement between the two element types, as well as good agreement with the eigenvalue analyses. As the nonlinear dynamic analysis buckling loads are lower than the analytical load, the resultant knockdown factors in Table 4.3 are calculated by dividing the numerical buckling loads by the reference analytical buckling load of 2271 kN from Table 3.4, as indicated by Equation 4.1.

Element	Displacement [mm]	Load [kN]	Resultant KDF [-]
SC8R	2.336	2194	0.97
S4R	2.334	2193	0.97

**Table 4.3:** Nonlinear dynamic analysis buckling load and displacement, alongside the resultant KDF.

$$\text{Resultant numerical KDF} = \frac{\text{numerical load}}{SP - 8007 \text{ analytical load}} \quad (4.1)$$

The full load-displacement behaviors from the S4R and SC8R nonlinear dynamic analyses are compared with the eigenvalue and linear static analyses in Figure 4.3, in addition to the SP-8007 buckling load. The qualitative stiffnesses indicated by the nonlinear analyses

show good agreement with those of the eigenvalue and linear static analyses. However, the nonlinear dynamic analyses display slight stiffness reductions and nonlinearities closer to buckling, which is expected from this analysis type. The post-buckled region, beginning at 2.34 mm of displacement, features reduced loading capacity and stiffness.

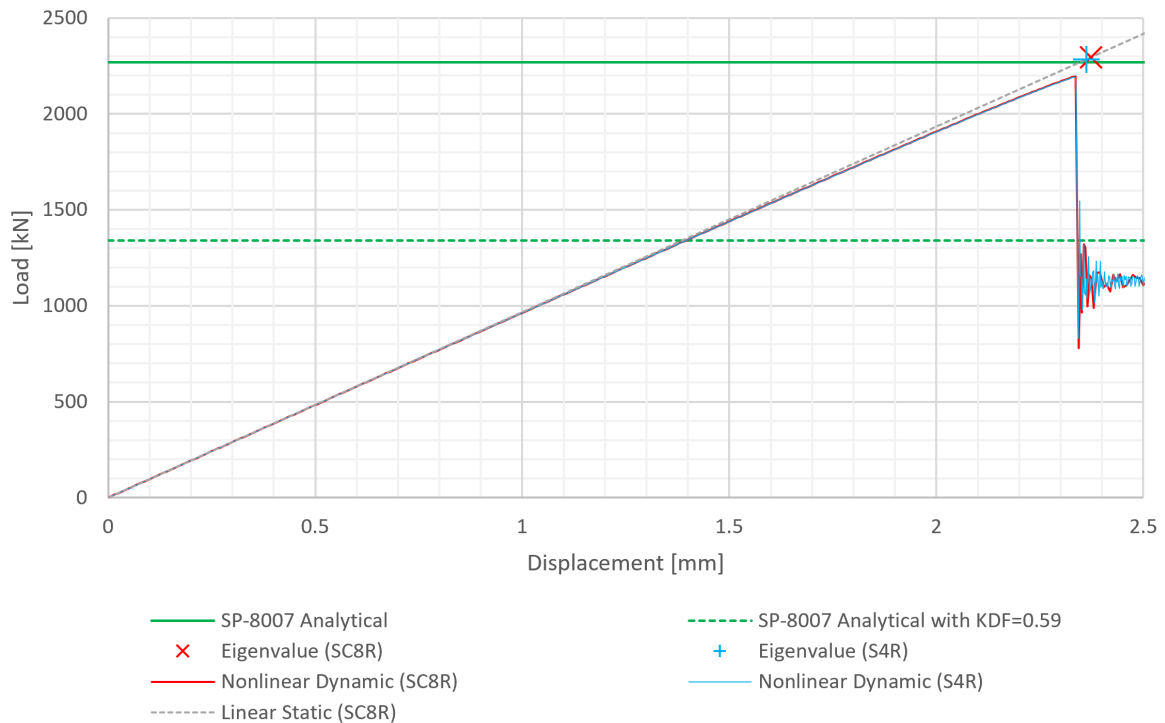


**Figure 4.3:** Comparison of analyses of the simplified shell without imperfections. Only linear analysis for the SC8R is shown due to similar results indicated in Table 4.2.

# Eigenmode & Trigonometric Imperfections

In this chapter, the sensitivity of the simplified shell to eigenmode shape and trigonometric imperfections was studied with nonlinear dynamic analysis. Eigenmode shape imperfections have been classically used in the estimation of experimental knockdown factors [17, 18, 19, 20, 21]. The trigonometric imperfection shape was explored as a result of the buckling shape prescription from the NASA SP-8007 solution. The performance of both the S4R and SC8R element types was analyzed.

## 5.1 Eigenmode Shape Imperfections

The eigenmode buckling shapes were extracted during the eigenvalue buckling analysis of Section 4.1 for implementation as imperfection shapes. The third eigenmode shape was used (rightmost in Figures 4.1 and 4.2). These were implemented with the \*IMPERFECTION keyword in conjunction with node shape files generated from the eigenvalue buckling analyses. Imperfection amplitudes corresponding to 5%, 10%, 20%, and 50% of the shell's nominal 4.2-mm wall thickness were chosen. An imposed axially compressive displacement rate of 2 mm per second was applied to the upper reference node. Buckling load results and resultant KDFs (calculated via Equation 4.1) are given in Table 5.1.

The buckling loads for given imperfection amplitudes are consistent between the two shell element types. Relative to the shell without imperfections, it is clear that even a 5% imperfection amplitude causes a significant reduction in the shell's buckling load. Further reduction of the buckling load is achieved with higher imperfection amplitudes.

Figures 5.1 and 5.2 reveal the full load-displacement curves for the SC8R and S4R simulations, respectively. Both show qualitatively similar behavior. Increasing imperfection amplitudes are accompanied by decreased pre-buckling stiffnesses, as indicated by the slopes of the curves. The post-buckled loading capacities for the 5% and 10% imperfection amplitude models do not

Eigenmode 3 Imperfection Amplitude	SC8R		S4R	
	Load [kN]	KDF [-]	Load [kN]	KDF [-]
0%	2194	0.97	2193	0.97
5%	1702	0.75	1726	0.76
10%	1461	0.64	1488	0.66
20%	1172	0.52	1143	0.50
50%	790	0.35	776	0.34

**Table 5.1:** Buckling load results from nonlinear dynamic analysis of eigenmode imperfections. The KDF is taken with respect to the SP-8007 analytical load without imperfection.

change as drastically as the buckling load itself relative to the shell without imperfections. For the higher 20% and 50% imperfection amplitudes, the transition from pre-buckling to post-buckling is much less distinct, in that there is a minimal or almost no sudden drop in loading capacity. In all cases, the post-buckled regime is characterized by low axial stiffness.

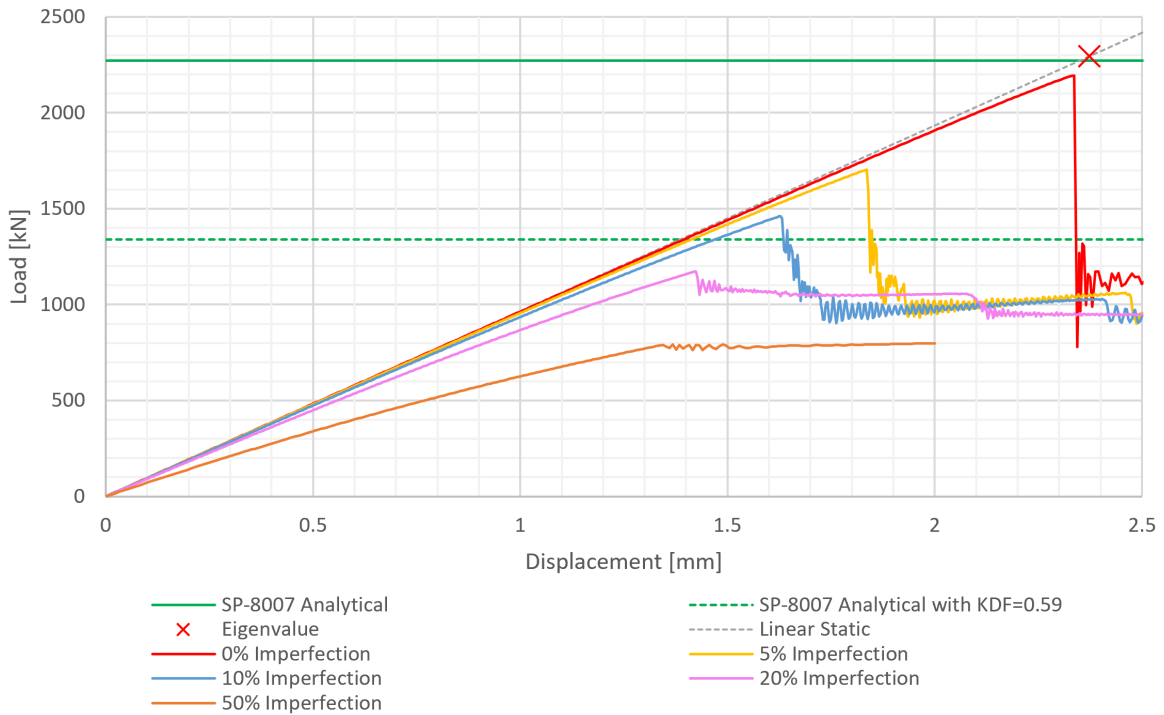


**Figure 5.1:** Third eigenmode imperfection results for the SC8R element model.

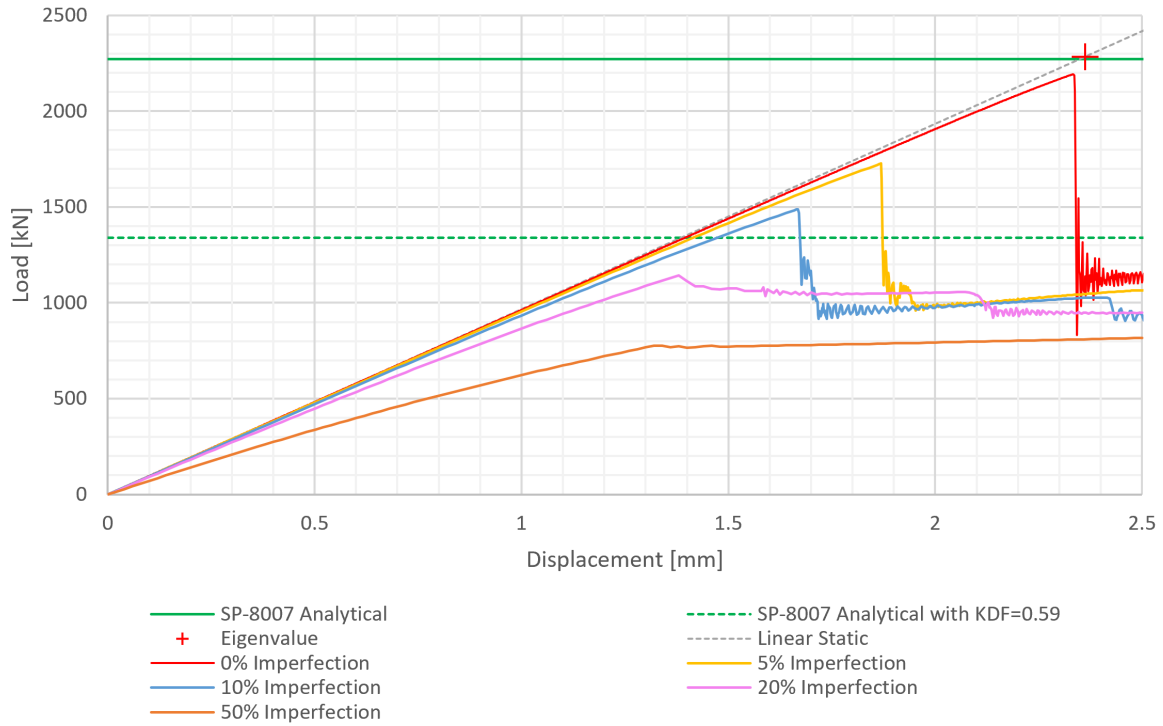


Figure 5.2: Third eigenmode imperfection results for the S4R element model.

## 5.2 Trigonometric Imperfections

The shape chosen for the trigonometric imperfection analyses were defined by the NASA SP-8007 analytical solution from Section 3.2 and Table 3.4. The initial trigonometric imperfection shape  $w_0$  was defined by Equation 5.1, where  $\theta$  is the angular position,  $z$  is the axial position,  $a$  is the amplitude,  $t$  is the wall thickness,  $h$  is the height,  $m$  is the number of axial half-waves, and  $n$  is the number of circumferential full-waves. The shape of this imperfection with  $m = 9$  and  $n = 0$  is illustrated in Figure 5.3.

$$w_0(\theta, z) = a \cdot t \cdot \sin\left(\frac{m\pi}{h}z\right)\cos(n\theta) \tag{5.1}$$

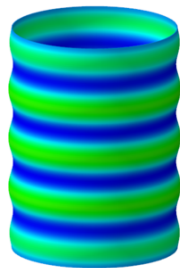


Figure 5.3: The initial trigonometric imperfection shape applied to the simplified laboratory-scale shell geometry with  $m = 9$ ,  $n = 0$ , and  $a = 50\%$  ( $\pm 2.1$  mm with respect to wall thickness), magnified 3x.

The initial imperfection shape was implemented into a finite-element model via a MATLAB script designed to generate node locations specifically with the shape defined by Equation 5.1. As with the eigenmode imperfections, a displacement rate of 2 mm per second was applied to the model's upper reference node in the axially compressive direction.

Table 5.2 shows the buckling load results of the trigonometric imperfection sensitivity analyses. In addition to good agreement between the two elements, the resultant KDFs for each imperfection amplitude are similar to those of the third eigenmode imperfection sensitivity study.

Trigonometric Imperfection Amplitude	SC8R		S4R	
	Load [kN]	KDF [-]	Load [kN]	KDF [-]
0%	2194	0.97	2193	0.97
5%	1700	0.75	1698	0.75
10%	1437	0.63	1432	0.63
20%	1125	0.50	1124	0.50
50%	732	0.32	734	0.32

**Table 5.2:** Buckling load results from nonlinear dynamic analysis of trigonometric imperfections. The KDF is taken with respect to the SP-8007 analytical buckling load.

The dynamic load-displacement behaviors of the various trigonometric imperfection amplitude models are compared in Figure 5.4 for the SC8R model and Figure 5.5 for the S4R model. As with the eigenmode shape imperfections, increased imperfection amplitude leads to a reduction in buckling load and pre-buckling stiffness.

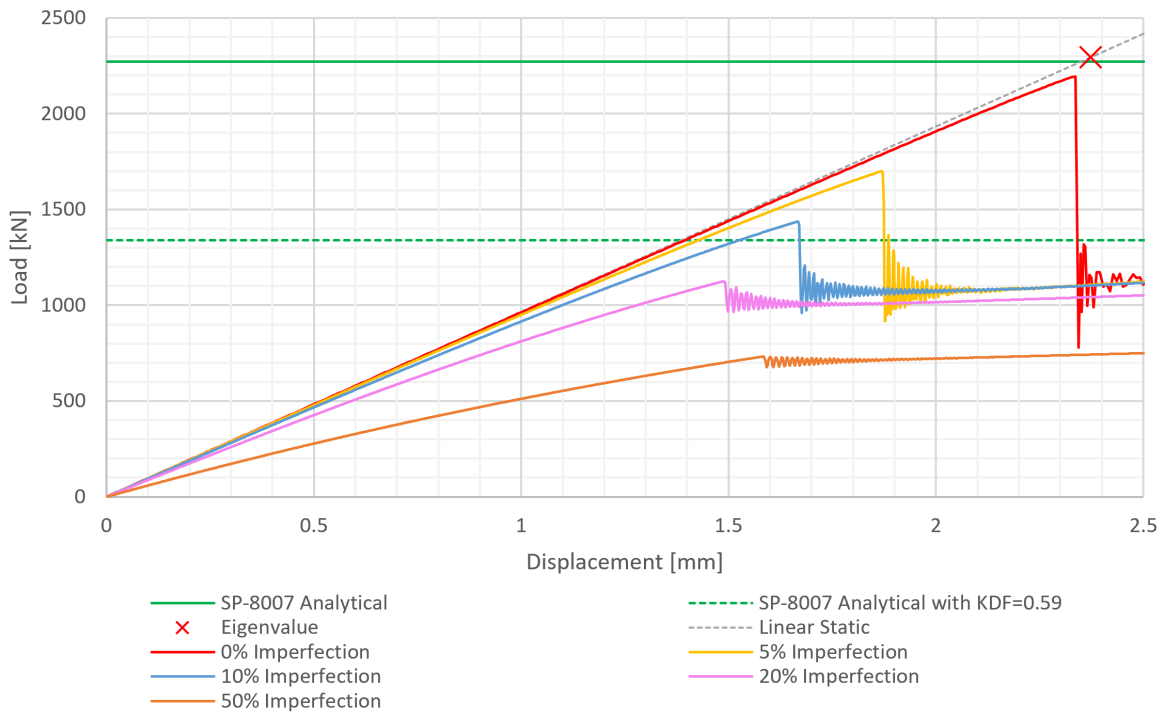


Figure 5.4: 9 axial half-wave trigonometric imperfection results for the SC8R element model.

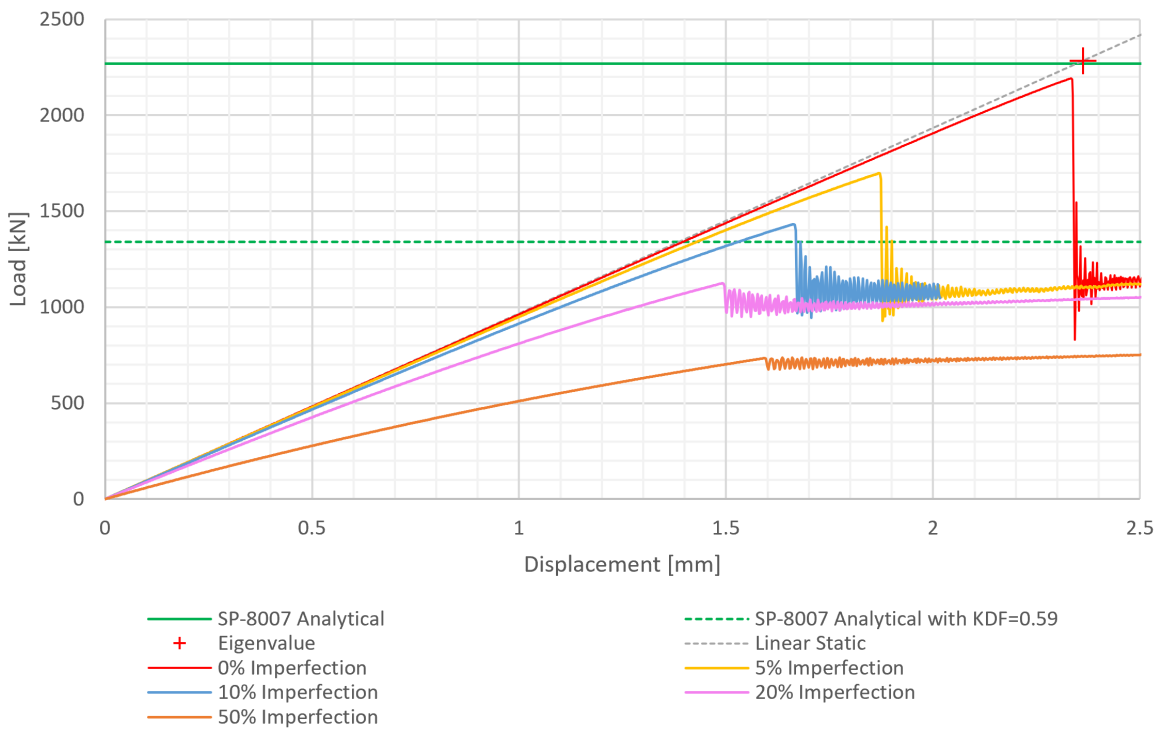


Figure 5.5: 9 axial half-wave trigonometric imperfection results for the S4R element model.

### 5.3 Conclusions on Eigenmode and Trigonometric Imperfections

At a given level of imperfection amplitude, the S4R and SC8R models have negligible differences in the buckling load for both eigenmode and trigonometric shape imperfections. This may be due to transverse shear within the shell wall being negligible, so the fact that the SC8R element accounts for transverse shear may not have substantially affected the buckling load or overall load-displacement behavior. It is possible that when applied to sandwich shell designs with a transversely shear compliant core material, these element types would not show the same level of agreement as with this solid laminate shell design.

Comparing the third eigenmode imperfections with this particular trigonometric imperfection pattern, a specified amplitude percentage gives very similar results. This is likely due to the fact that both have nine axial half waves. Additionally, the models with trigonometric imperfections were less stiff than their eigenmode shape counterparts at a given imperfection amplitude. This may be caused by the trigonometric imperfection waveform reaching a maximum amplitude at every peak or valley (i.e. at nine locations, per Figure 5.3), whereas the third eigenmode shape amplitude is only at a maximum amplitude near the center (see the two red peaks and one blue valley in Figures 4.1 and 4.2). The result is that the trigonometric imperfection shell models have a larger net amount of “waviness” for a given amplitude, and thus they are more compliant.

# Loading Imperfections

Two types of loading imperfection were investigated in order to simulate two different physical situations that might occur in experimental testing. The first loading imperfection model attempts to simulate a test in which the upper loading surface “settles” during testing due to the center-of-load being misaligned with the shell’s axis (this could be due to a load frame having “play” in its actuation mechanisms). The second type attempts to mimic the behavior of an upper loading platen that has a fixed angular offset relative to the shell’s upper edge. A distinguishing feature between the two is that the former results in no reaction moment at the upper boundary, whereas the latter does. Both sets of simulations used a loading rate 2 mm per second loading rate with nonlinear dynamic implicit analysis.

### 6.1 Loading Imperfection 1: Settling Platen

This first loading type imperfection was implemented into finite element models by using a multi-point beam constraint (Abaqus keyword \*MPC with the BEAM option) between the top reference node and the top nodes of the shell model rather than the previously used rigid body tie constraint. The top reference node was then moved laterally in the X direction (within the plane of the shell’s top edge) by varying amounts to create an off-axis load application point, and the reference node was allowed to rotate freely about the Y direction. An example of this setup is shown in Figure 6.1.

The multi-point beam constraint allows for the reaction forces in the model to be distributed in proportion to the distance from a given shell edge node to the reference point. Consequently, if the reference node is placed off-center (see Figure 6.1) and is allowed to rotate about the Y-axis, the upper boundary of the shell will rotate about the Y-axis during load application. A displacement rate of 2 mm per second was used with nonlinear implicit dynamic simulation.

The results of varying the top reference node’s center offset are given in Table 6.1. Figure 6.2 shows the load-displacement curves for this imperfection type, and Figure 6.3 indicates the progression of Y-axis rotation of the top edge until buckling as the imposed displacement was applied.

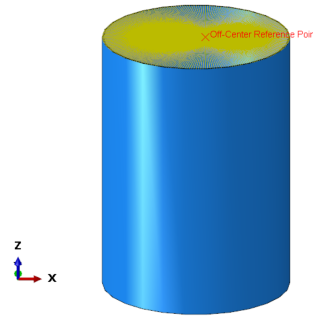


**Figure 6.1:** Schematic implementation of the “settling platen” load imperfection. Note that the top reference point (red) is shifted slightly off-center. The yellow lines represent multi-point beam type constraints.

Center Offset		Buckling Load [kN]	KDF [-]	Rotation @ Buckling [°]
[mm]	[% of radius]			
0	0%	2194	0.97	0
5	1.25%	2165	0.95	0.008
10	2.5%	2120	0.93	0.014
20	5%	2035	0.90	0.026

**Table 6.1:** Summary of “settling platen” loading imperfection sensitivity.

The results indicated that moving the center-of-load off-center by 5% of the shell’s radius reduces the buckling load of the shell without geometric imperfections by 10% relative to the analytical buckling load. Furthermore, Table 6.1 and Figure 6.3 indicate that this type of loading imperfection resulted in the loading boundary rotating by of  $0.026^\circ$  at the moment of buckling.

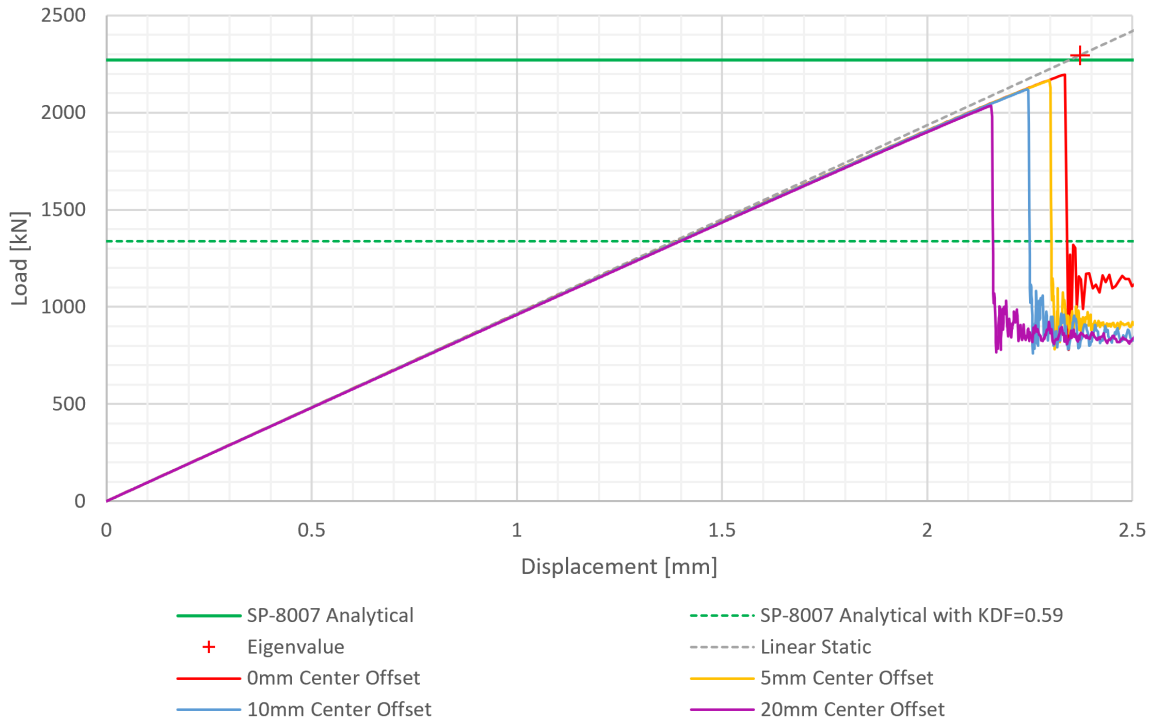


Figure 6.2: Load versus displacement results of the “settling platen” loading imperfection.

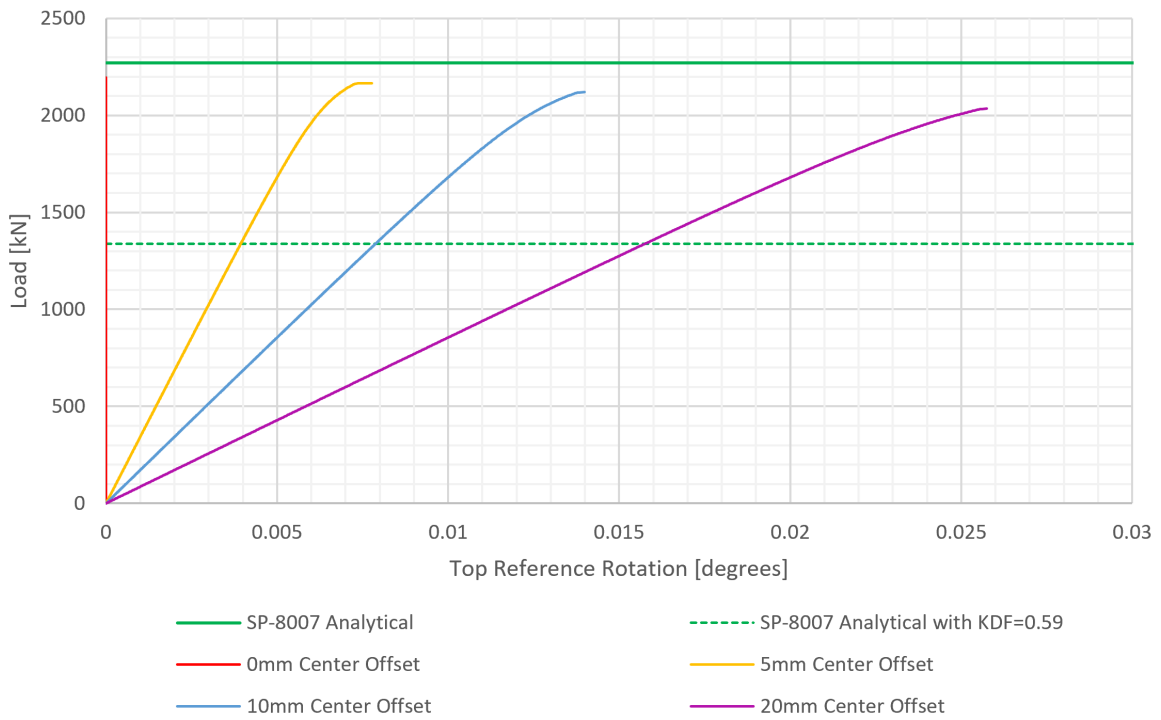


Figure 6.3: Load versus top edge rotation angle for the “settling platen” loading imperfection.

## 6.2 Loading Imperfection 2: Platen with Fixed Angular Offset

The fixed angular offset simulation of this section was conducted to simulate a loading platen with constant angular tilt relative to the top edge of the shell. This was accomplished via a two-step analysis. In the first step, an initial rotation was applied to the top reference node ( $0.001^\circ$ ,  $0.01^\circ$ ,  $0.05^\circ$ , or  $0.1^\circ$ ). Once the rotation angle was reached, an axially compressive displacement rate of 2 mm per second was applied to the top reference while maintaining the fixed rotation angle achieved from the previous step.

Results are shown in Table 6.2 and Figure 6.4. The boundary height difference noted in the second column of Table 6.2 indicates the vertical distance between the highest and lowest points on the upper shell edge. These analyses indicate that the shell model's buckling load begins to respond to upper boundary rotations between  $0.001^\circ$  and  $0.01^\circ$ . After this initial amount, an increase of the boundary rotation to  $0.1^\circ$  has a notable effect on reducing the shell's buckling load.

Angular Offset [ $^\circ$ ]	Boundary Height Difference Range (with 400-mm radius) [mm]	Buckling Load [kN]	KDF [-]
0	0	2194	0.97
0.001	0.014	2195	0.97
0.01	0.14	2145	0.94
0.05	0.7	2066	0.91
0.1	1.4	1473	0.65

**Table 6.2:** Summary of fixed angular platen offset loading imperfection sensitivity.

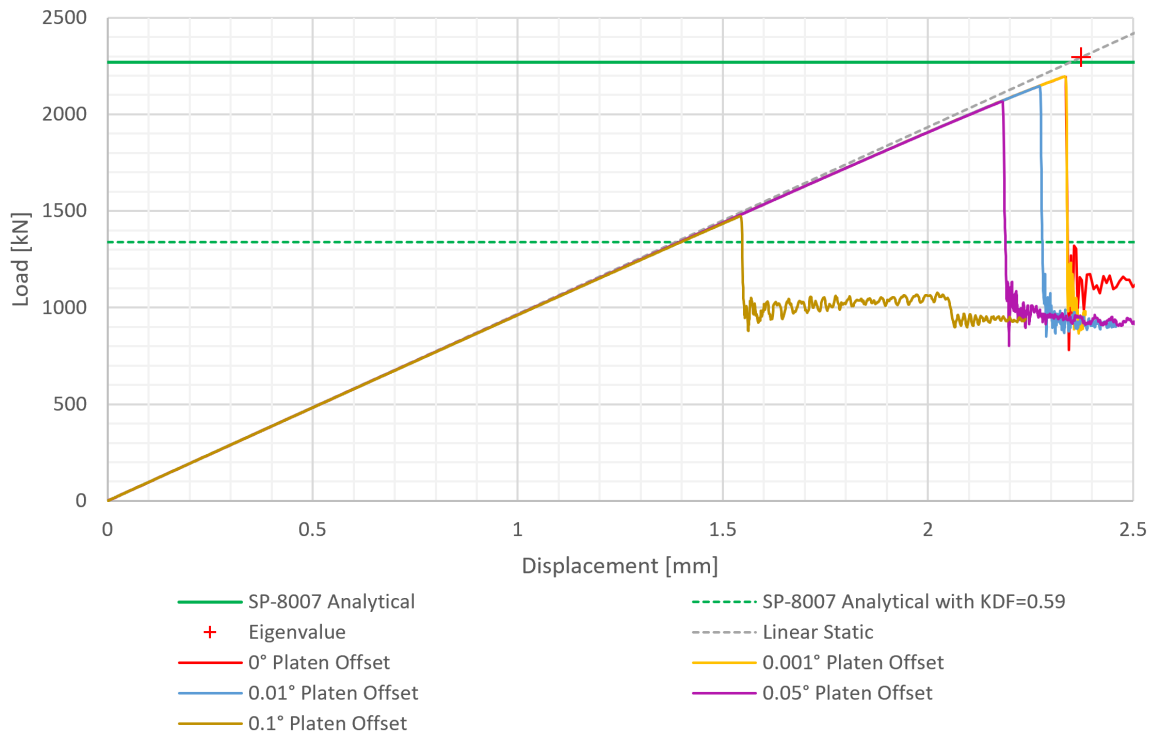


Figure 6.4: Load versus displacement results of the fixed platen angle loading imperfection.

### 6.3 Conclusions on Loading Imperfections

Of the two loading imperfections investigated, even seemingly minor rotational offsets or off-center loads can reduce the buckling load. Most likely, a loading imperfection experienced in reality would be closer to the second type in which there is a fixed offset. This imperfection could be due to misalignment of the platen itself and/or variation between linear actuators controlling an experimental load frame, if there are multiple actuators controlling the displacement. For “settling platen” imperfection to occur in reality, there would likely need to be a large amount of “play” in the actuation machinery of the load frame, or the shell being tested would need to be extremely stiff compared to the load frame such that deformation of the load frame itself would not be negligible. The KDFs due to loading imperfections show that even small angular misalignment of the platen – as low as  $0.01^\circ$  – can reduce the buckling load of this shell model without imperfections by 3%.



# NDL-1 Description & Measured Imperfection Signature

The test article NDL-1 and its imperfection signature are described in this chapter. First, NDL-1's composite shell geometry is presented; it differs slightly from the equivalent simplified shell studied in the previous chapters. NDL-1's four constituent layups are then given. The primary portion of the shell has the same layup as the simplified shell, but three additional layup sections at each end aid in load introduction. The geometric and material specifications of NDL-1's potting and end rings, which are required for experimental testing and also assist in load transfer, are presented. Then NDL-1's unique measured imperfection signature is introduced; this consists of inner, outer, and boundary surface data.

## 7.1 NDL-1 Specifications

NDL-1 is comprised of a composite shell, four sections of potting that encase the shell's ends both on the inside and outside, and four aluminum end rings that in turn surround the innermost and outermost potting surfaces, as indicated in Figure 7.1.

### 7.1.1 Shell

The shell of NDL-1 was manufactured via hand layup of 12.5-mm wide tows of the preimpregnated carbon-fiber-epoxy composite IM7-8552 introduced in Chapter 3. The composite shell geometry is given in Table 7.1 and Figure 7.2. Table 7.2 specifies the four layups that comprise the shell: a primary layup (the same as the simplified shell) and three pad-up sections found on either end of the shell. The same stacking orientation system specified in Figure 3.1 was used. Pad-ups assist in transferring load from the edge regions to the central portion of the shell [36, 49]. Furthermore, they induce buckling to occur in this central acreage during testing, thus insuring that the stability phenomenon can be studied in a controlled manner. The first, second, and third pad-up ply lengths referred to in Table 7.1 correspond to the 90°,

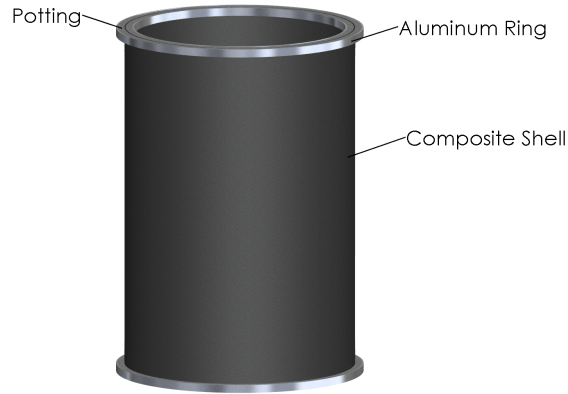


**Figure 7.1:** 3D view of the NDL-1 assembly.

$-45^\circ$ , and  $45^\circ$  plies, respectively. Figure 7.3 further illustrates the ply stacking and pad-up regions. The shell has a constant nominal inner radius, as the mandrel upon which the shell was manufactured also had a constant radius; pad-up plies are layered such that the shell has varying mid-surface and outer radii when comparing the primary section to the pad-up sections.

Inner Radius [mm]	Height		Pad-up ply length		
	Total [mm]	Un-potted [mm]	1st [mm]	2nd [mm]	3rd [mm]
400.1	1224.3	1168.4	104.1	87.6	72.4

**Table 7.1:** Geometry of the NDL-1 composite shell.

Section	Layup
Primary	$[(23/0/-23)_{S4}]$
1st pad-up	$[(23/0/-23)_{S3}/(23/0/-23/\overline{90})_S]$
2nd pad-up	$[(23/0/-23)_{S3}/-45/(23/0/-23/\overline{90})_S]$
3rd pad-up	$[(23/0/-23)_{S2}/(23/0/-23/\overline{45})_S/-45/(23/0/-23/\overline{90})_S]$

**Table 7.2:** Section layup definition. The stacking sequences are listed from innermost ply to outermost ply.

### 7.1.2 Potting and End Rings

The potting and end rings of NDL-1 act as stabilizing media that provide a partial clamping effect on the shell's edges; this is not a fully clamped condition because the potting itself is able to deform. The potting's surface area also helps facilitate load transfer from the test apparatus into the shell by minimizing the risk of damage to the shell's edges. The material properties of the potting and end rings are presented in Table 7.3. Micorox Standard Grout was used for potting. While its elastic modulus and density were available via the manufacturer [59], its Poisson's ratio was assumed to be 0.30. No grade of aluminum was specified, so the

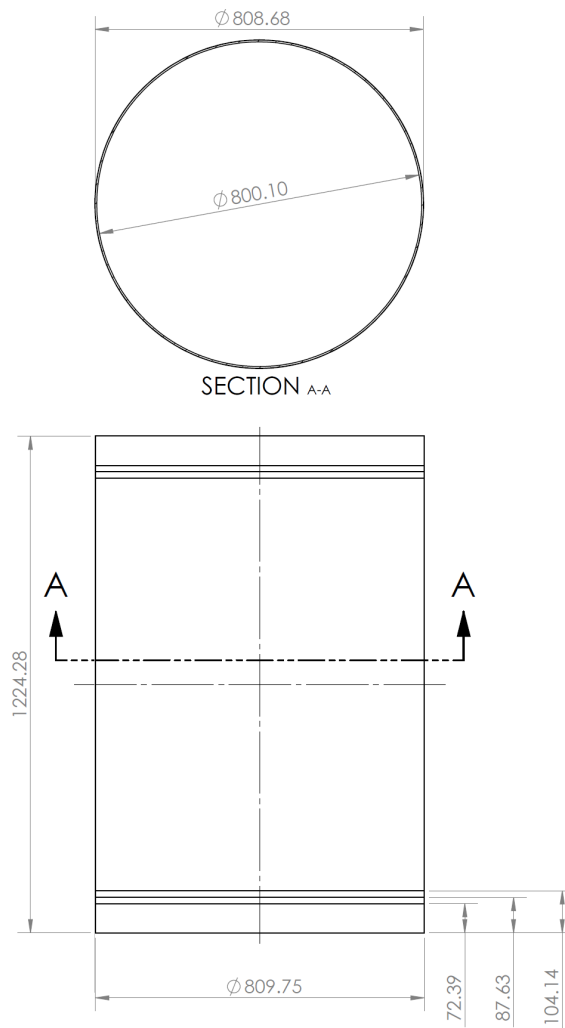


**Figure 7.2:** Drawing of the NDL-1 composite shell. Dimensions are in millimeters.

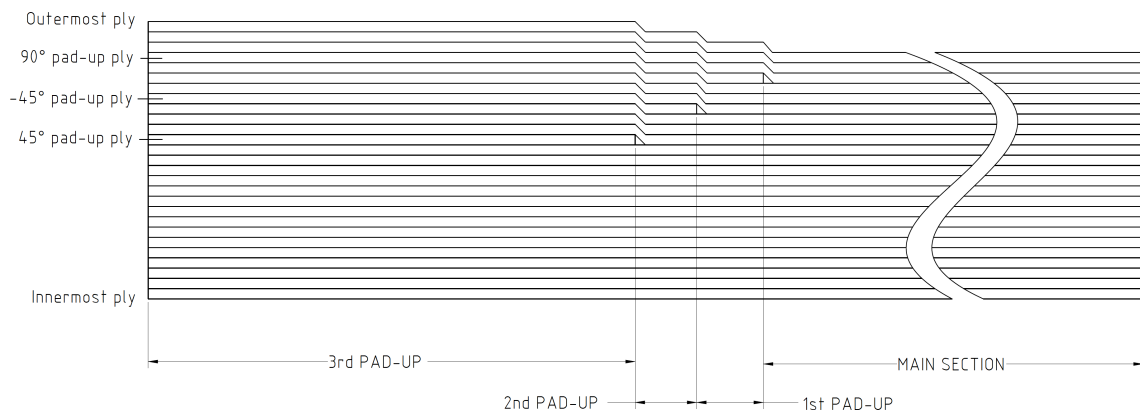


**Figure 7.3:** Ply stacking schematic indicating the pad-up zones and pad up plies (stacking illustration courtesy of NASA).

properties of the end rings were assumed based on typical aluminum properties. NDL-1's end ring geometry is given in Table 7.4. The potting fills the volumes between the composite shell and the rings as indicated in Figure 7.1.

Part	Material	$E$ [GPa]	$\nu$ [-]	$\rho$ [g/cm <sup>3</sup> ]
Potting	Epoxy	7.6	0.30	1.68
End Rings	Aluminum	69	0.33	2.70

**Table 7.3:** Potting and end-ring properties.

Ring Set	Quantity	Height [mm]	Inner Diameter [mm]	Outer Diameter [mm]
Inner	2	27.9	741.4	754.1
Outer	2	27.9	855.7	868.4

**Table 7.4:** Geometry of NDL-1's aluminum end rings.

## 7.2 Imperfection Measurement Data

NDL-1's imperfection signature was measured with an ATOS II structured light scanner at NASA Marshall Space Flight Center. Figure 7.4 shows the edge of the test article being scanned.

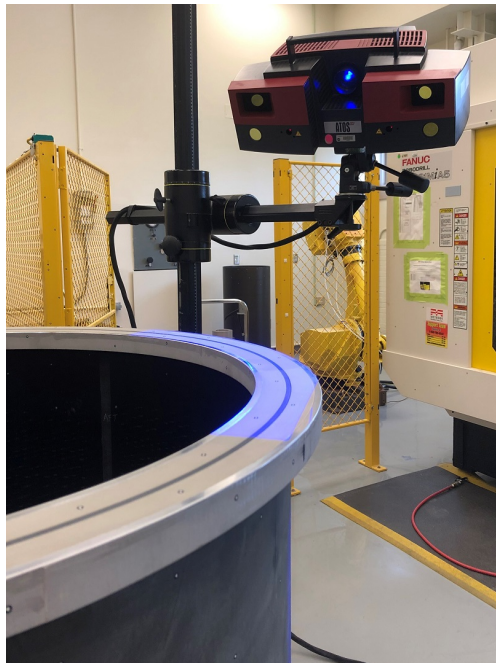


**Figure 7.4:** Imperfection measurements were taken by a structured light scanner at NASA Marshall Space Flight Center (photo courtesy of NASA).

### 7.2.1 Inner and Outer Surfaces

The inner and outer surface data, shown in Figures 7.5 and 7.6, consisted of approximately 11.5 million and 28 million 3D-scan points, respectively, and correspond to areal densities of 4.1 and 9.5 points per square millimeter. A ring-shaped imperfection can be seen between axial positions of approximately 125 mm and 175 mm around the entire circumference of both surfaces. It is thought that the mandrel was doubly machined here during finishing, and that this shape was then consequently transferred to the shell during manufacturing.

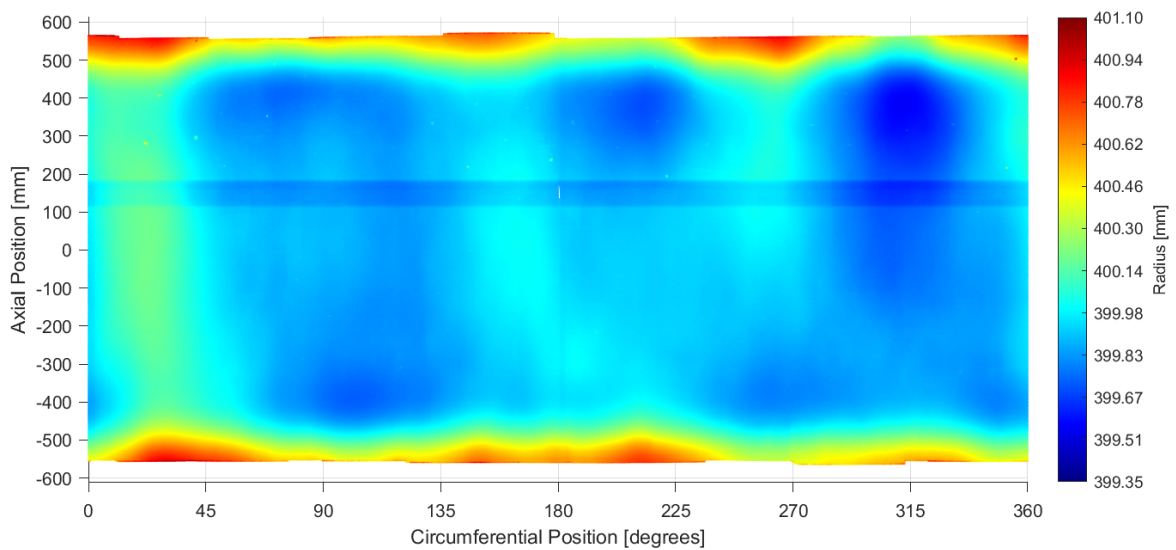


Figure 7.5: Measured inner surface data.

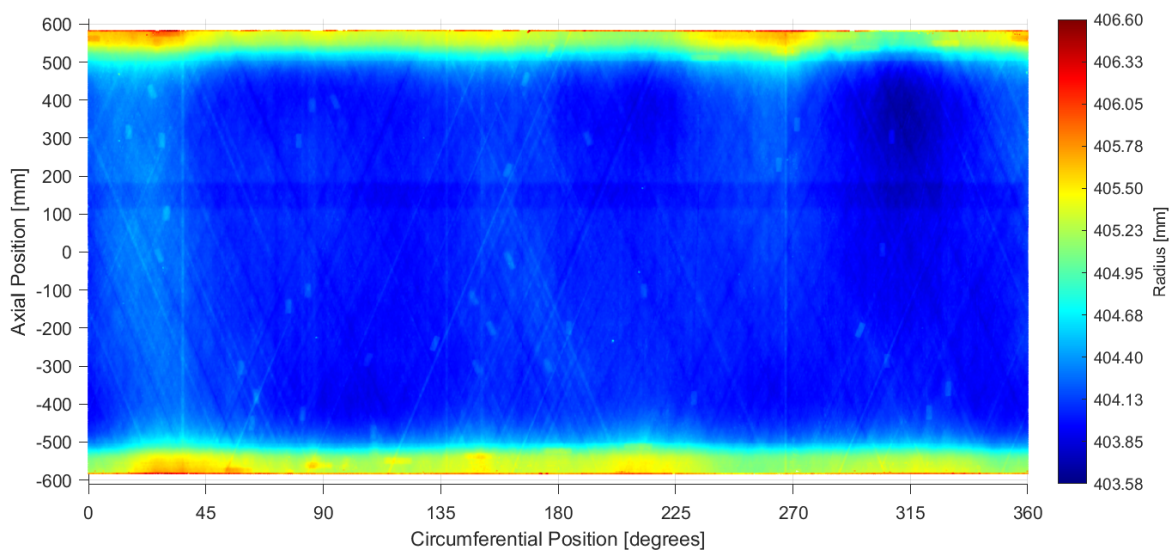
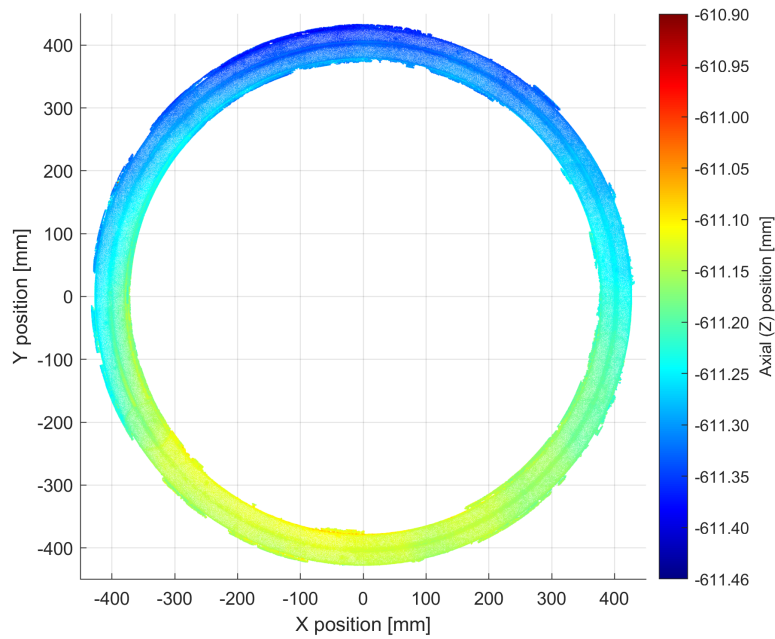


Figure 7.6: Measured outer surface data.

### 7.2.2 Boundary Surfaces

The lower and upper boundary surfaces of NDL-1 were measured, as shown in Figures 7.7 and 7.8, respectively. Milling was performed on these surfaces after the shell was potted, and the boundary surface measurements were taken after this. The number of raw data points per boundary surface measurement set is approximately 500,000, yielding an areal density of 4.2 points per square millimeter.



**Figure 7.7:** Measured lower boundary surface data.

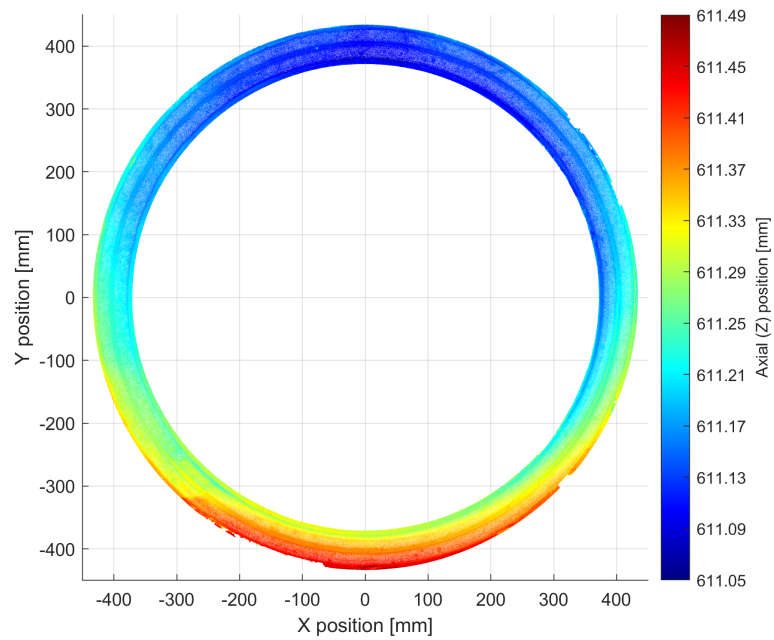


**Figure 7.8:** Measured upper boundary surface data.



# NDL-1 Modeling & Preliminary Simulation Results

This chapter details the process of modeling the test article, material property values used in the simulations, and preliminary simulation results. First, the modeling procedure is presented, including details on mesh size, element choice, and the generation of Abaqus solver input files. The interpolated inner and outer surfaces used in the model are also presented, including a statistical quality analysis to insure that these modeled surfaces were properly representative of the raw 3D-scan data. Additionally, the shell thickness and mid-surface contours are presented; these were derived from the interpolated inner and outer surfaces. Aspects relating to the final composite material property values used in simulation are then discussed, for which the reasons are twofold. First, a NASA tensile test indicated that the as-manufactured IM7-8552 properties differed from the nominal properties. Furthermore, the thickness contour derived from the interpolated surfaces indicated the manufactured shell was thinner than the nominal ply thickness and mean tensile specimen thickness, potentially warranting additional adjustment of the material property values. Finally, a preliminary set of results from two pre-experimental simulations with imperfections are presented.

## 8.1 Test Article Model

### 8.1.1 Element Type and Mesh Size

The SC8R eight-node continuum shell element was chosen for modeling the test article due to its solid geometry and ability to account for transverse shear. The former implies that the inner and outer imperfection surfaces of the measured test article could be conveniently implemented directly at the SC8R elements' nodes. If using a surface-geometry-based shell element (such as the S4R) when attempting to model inner and outer imperfections rather than only a single surface (e.g. an outer or mid-surface imperfection), each element would require a unique thickness value to capture both the inner and outer surface imperfections.

This in turn would necessitate as many section definitions as elements contained in the shell, leading to large solver input files.

A 5-mm mesh was chosen for the test article model and deemed acceptable based on the simplified shell convergence study of Chapter 3. This size was used rather than 10 mm in order to better capture the details of the measured surfaces, with an accepted decrease in computational efficiency.

### 8.1.2 Input File Generation

A MATLAB script was written to automate the creation of Abaqus node and element input files from nominal shell geometry and imperfection data. The flow of data in the script is summarized as follows.

- Define the nominal test article geometry.
- Define the target mesh size.
- Determine the number of elements along the circumference/height from the target mesh size.
- Define the circumferential and axial node coordinate grid sets from the element quantities and nominal dimensions.
- Import the inner and outer surface Cartesian 3D-scan point imperfection data.
- Convert the surface imperfection data from Cartesian coordinates to cylindrical coordinates.
- Define the upper and lower trim limits for the surface imperfections; exclude data points outside of these limits. This step is performed to remove fringes of data points from the edges. Moreover, these inner and outer surfaces are trimmed at the same levels to insure even thickness when extrapolating radius values to the shell model's acreage that corresponds to the actual shell acreage covered by potting, which could not be measured.
- From the imperfection 3D-scan point data, interpolate the radial coordinates of inner and outer surface nodes for every circumferential/axial node coordinate grid set previously defined.
- Generate the radial locations for potting and end ring nodes.
- Convert the shell, potting, and end-ring node locations from cylindrical coordinates to Cartesian coordinates.
- Adjust the axial node locations of upper and lower surfaces via linear interpolation of edge imperfection data.
- Assign the nodes to elements.
- Write the node and element input files.

### 8.1.3 Final Mesh Details

The 5-mm mesh size resulted in 123,725 SC8R continuum shell elements for the composite cylindrical shell. The potting and aluminum rings were modeled respectively with 60,600 and 12,120 C3D8 three-dimensional stress elements. The upper end section of the model is illustrated in Figure 8.1. Further details of the mesh are given in Table 8.1. As with the previous simulations, all upper edge nodes of the NDL-1 model (including those of the potting and end rings) were tied to an upper reference node, and all lower edge nodes were tied to a lower reference node. The lower reference node was clamped, and the upper reference node was constrained in all degrees of freedom except for the axial direction. Axial displacement was applied to the upper reference node, and the reaction force at this node was measured.

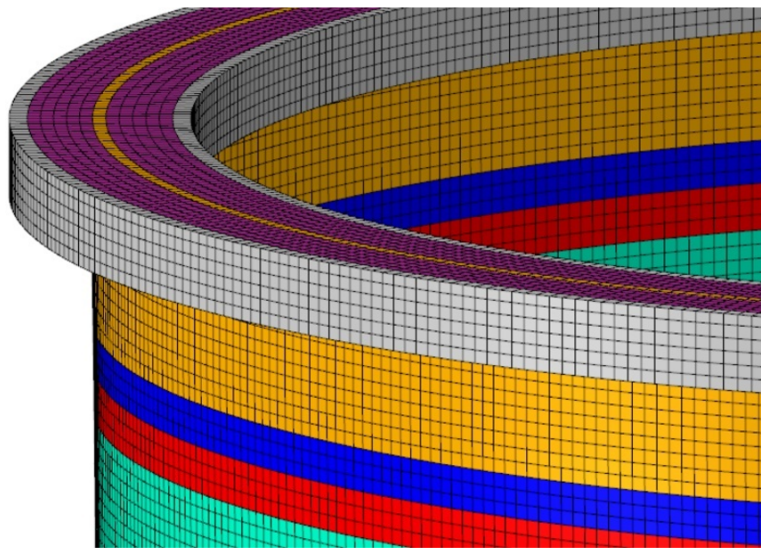


**Figure 8.1:** Detail view of the mesh used in pre-test simulations.

Section	Color in Figure 8.1	Element Type	Quantity of Sections	Elements along		
				Circumference	Height	Thickness
Main	Cyan	SC8R	1	505	203	1
1st Pad-up	Red	SC8R	2	505	3	1
2nd Pad-up	Blue	SC8R	2	505	3	1
3rd Pad-up	Gold	SC8R	2	505	15	1
Potting	Purple	C3D8	4	505	6	5
End Rings	Grey	C3D8	4	505	6	1

**Table 8.1:** Mesh information for the final pre-test simulations.

### 8.1.4 Interpolated Imperfection Surfaces

The interpolated inner and outer surfaces used in the final model are shown respectively in Figures 8.2 and 8.3.

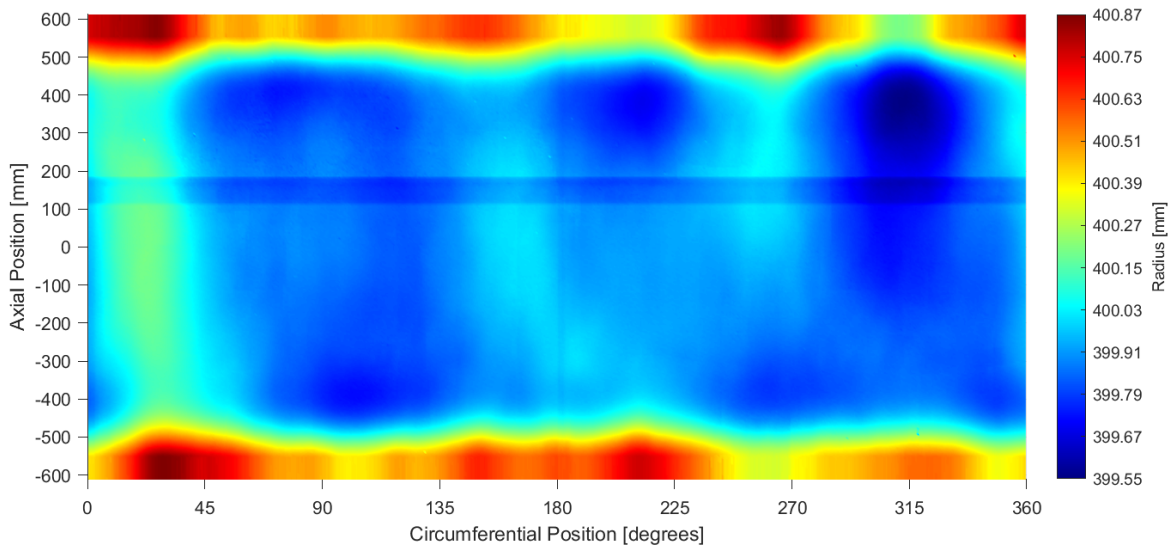


Figure 8.2: Interpolated inner surface.

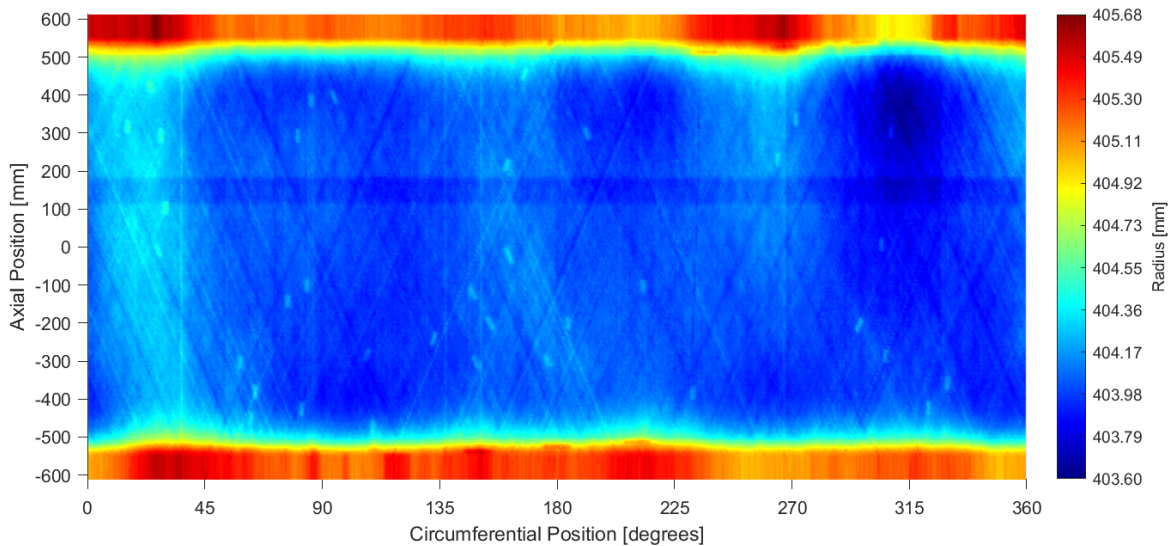


Figure 8.3: Interpolated outer surface.

As indicated by Figure 7.6, the measurement system was able to capture almost all of the nominal free (non-potted) height of the cylindrical composite shell's outer surface. However, Figure 7.5 reveals that the structured light scanner was unable to capture some of the shell's inner surface near the potting. Additionally, Figure 7.5 shows uneven upper and lower edges of the inner surface (i.e. the maximum and minimum axial data captured varies around the circumference). This fringing was also present on the outer surface data, although it was much

less prominent. The reason for the lower quality of inner surface measurement in the edge regions was likely due to the limited viewing angles and maneuverability of the scanner when measuring the inner surface from an exterior position, in contrast with the greater motional freedom when capturing the outer surface.

Consequently, the data sets were trimmed to fall within maximum and minimum axial limits. Initially, different minimum and maximum limits were applied to the inner and outer surfaces in order to retain as much of the raw data as possible. However, upon extrapolating the trimmed edge data to the axial extents of the test article model (i.e. the unmeasured areas covered by potting) in preliminary interpolation attempts, this led to unrealistic interpolated thickness in the areas immediately adjacent to and covered by potting. This was due to the fact that extrapolations occurred from different axial locations for the inner and outer surfaces. Thus, it was determined that a set of common trimming limits should apply to both the inner and outer surface data, so as to result in reasonable average ply thicknesses consistent with the rest of the shell. An upper axial trim location of 553.70 mm and a lower axial trim location of -551.25 mm were chosen. Node locations outside the aforementioned axial trim limits were assigned the radius value of the nearest node within the trim limits. The effect of this is characterized by repeating edge pixels at the tops and bottoms of Figures 8.2 and 8.3.

The influence of three interpolation methods was investigated for transforming the 3D-scan point data into FE mesh data: nearest-neighbor, linear, and inverse distance weighted. Nearest-neighbor interpolation is the most computationally efficient, but has a higher risk for translating noise from the measurement system into the final mesh. Another drawback is that if the 3D-scan point data has nonuniform density (in contrast to the regularly spaced mesh grid coordinates), there is a risk that a circumferential/axial mesh coordinate pair corresponding to a location far from the nearest 3D-scan point could result in far-away radial data being interpolated to that mesh point, thus distorting the shape of the model relative to NDL-1. Linear interpolation is slightly less computationally efficient, but mitigates the two aforementioned drawbacks of nearest-neighbor interpolation. Finally, inverse distance weighted interpolation (developed by Castro et al. [20]) was found to be less efficient for these particular amounts of 3D-scan data and mesh points (requiring either several hours on a machine with 32GB of RAM, or less time with *several terabytes* of RAM), but it can reduce the possibility of measurement noise being translated into the mesh better than the previous two methods by allowing a specified amount of points within a given radius to contribute to the interpolated value. Ultimately the difference between methods – with respect to load-displacement behavior and buckling load – was found to be negligible. Thus, linear interpolation was selected due to its efficiency and presence in the literature [6, 25, 39, 40, 41, 43]. Linear interpolation was also used to translate the lower and upper boundary edge imperfection data of Figures 7.7 and 7.8 into the finite element mesh.

### Statistical Quality of Imperfection Surface Interpolation

The statistical quality of the interpolated surfaces was assessed in relation to the raw data to insure that the finite element mesh with imperfections was representative of the measured 3D-scan data. The efficacy of interpolation was evaluated via the frequency distributions of radial imperfection data, as given in Figures 8.4 and 8.5, which show the relative occurrence of

given radii in the raw data and the mesh. These histograms consider the middle 1000 mm of composite shell, which is just within the extent of the primary layup section (nominally 1016 mm in height). Solely on the basis of these plots (and not considering potential non-uniform density of the 3D-scan data), the inner interpolation shows generally good agreement, and the outer interpolation shows excellent agreement.

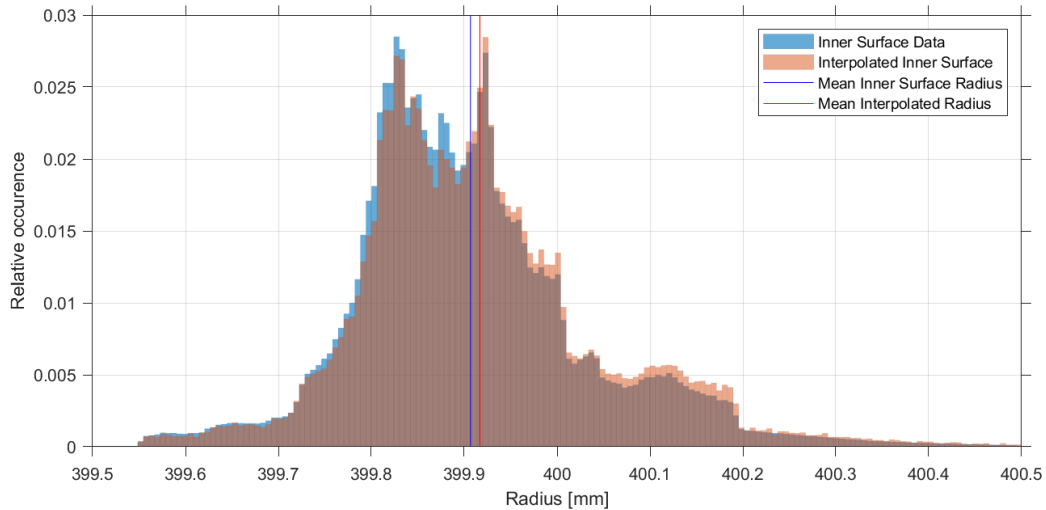


**Figure 8.4:** Histogram data for raw inner surface data and the interpolated surface for the middle 1000 mm of shell height.

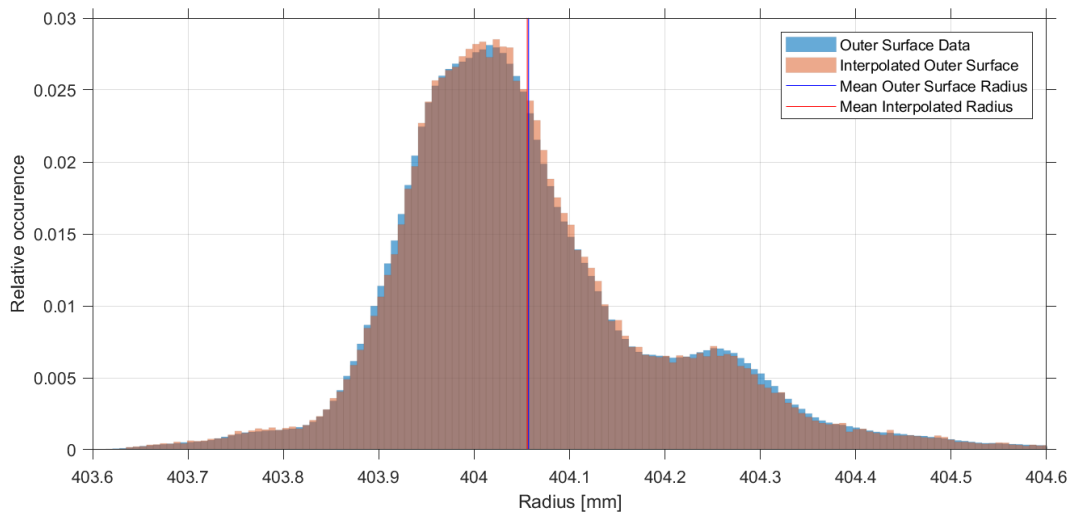


**Figure 8.5:** Histogram data for raw outer surface data and the interpolated surface for the middle 1000 mm of shell height.

A possible reason for the slight variance in distribution shape between the inner surface 3D-scan point data and its interpolation is non-uniform 3D-scan point density (i.e. the 3D-scan did not record data points at regularly spaced intervals). In contrast, the mesh points to which radius values were interpolated were by definition spatially uniform. Table 8.2 shows the number of 3D-scan points collected in the middle 1000 mm along NDL-1's height for

both the inner and outer surfaces. The number of points is segmented into 100-mm axial intervals. The higher coefficient of variation for the inner surface 3D-scan data than that of the outer surface potentially explains the minor qualitative difference in shape of the raw and interpolated radial distribution shapes illustrated in Figure 8.4; in comparison, the outer surface scan data has a lower coefficient of variation, and correspondingly the radial frequency distribution shapes of 3D-scan data and the interpolation appear to show better qualitative agreement.

Axial Window Bound		3D-Scan Points [millions]	
Lower [mm]	Upper [mm]	Inner Surface	Outer Surface
400	500	1.09	2.20
300	400	1.22	2.33
200	300	1.34	2.35
100	200	1.10	2.41
0	100	0.91	2.45
-100	0	0.94	2.40
-200	-100	0.94	2.40
-300	-200	0.87	2.33
-400	-300	0.86	2.35
-500	-400	0.84	2.48
Mean		1.01	2.37
Standard Deviation		0.17	0.08
Coefficient of Variation		1.67%	0.33%

**Table 8.2:** 3D-scan points contained per 100-mm axial window for the middle 1000 mm of shell. The outer surface shows a more axially uniform distribution of points than the inner surface.

### Interpolation-Derived Shell Thickness and Mid-Surface

Figure 8.6 shows the resultant interpolated shell thickness via subtraction of the interpolated inner surface from the interpolated outer surface. This was possible because the circumferential and axial mesh coordinates were defined at the same points for both the inner and outer interpolated surfaces. The layup's  $-23^\circ$ ,  $0^\circ$ , and  $23^\circ$  ply angles are prominent here; this may be an artifact of the hand-layup process in which the spacing between adjacent tows is not as consistent as with automation; additionally the ply angle visibility may have been caused by slight width variations along the unidirectional tape's length.

The interpolated mid-surface (average of the interpolated outer and inner surface node radii) is shown in Figure 8.7. Within the primary layup section (middle 1016 mm of the shell), this information was used to derive a rudimentary imperfection amplitude. This amplitude was taken as half of the difference between the mid-surface's maximum and minimum radii (402.65 mm and 401.58 mm, respectively) in this central region. The resulting imperfection amplitude is 0.53 mm. With a mean primary layup thickness of 4.14 mm, the amplitude with respect to wall thickness is 12.8%.

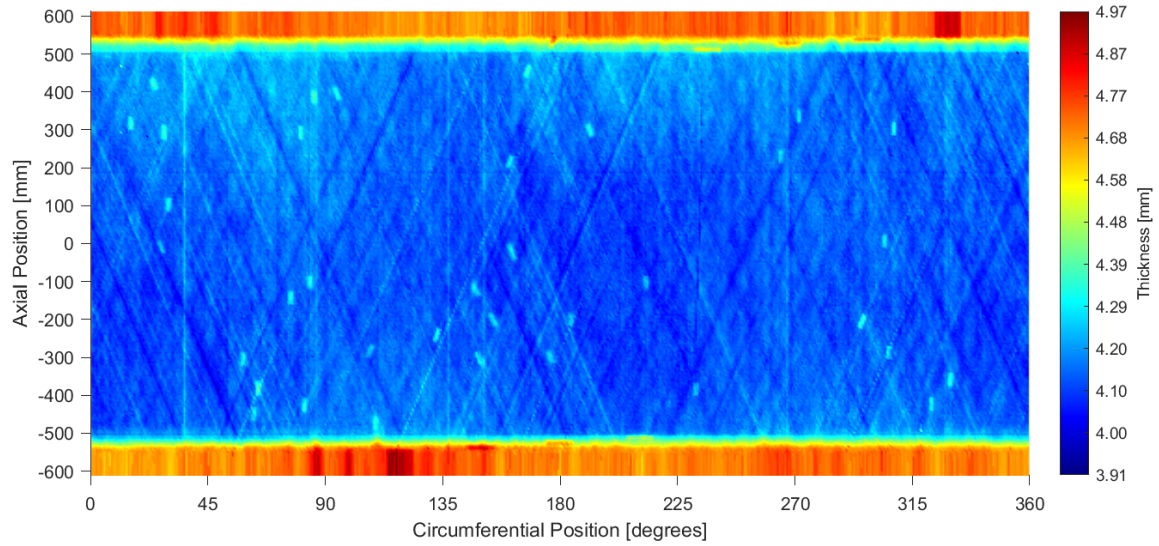


Figure 8.6: Interpolated thickness.

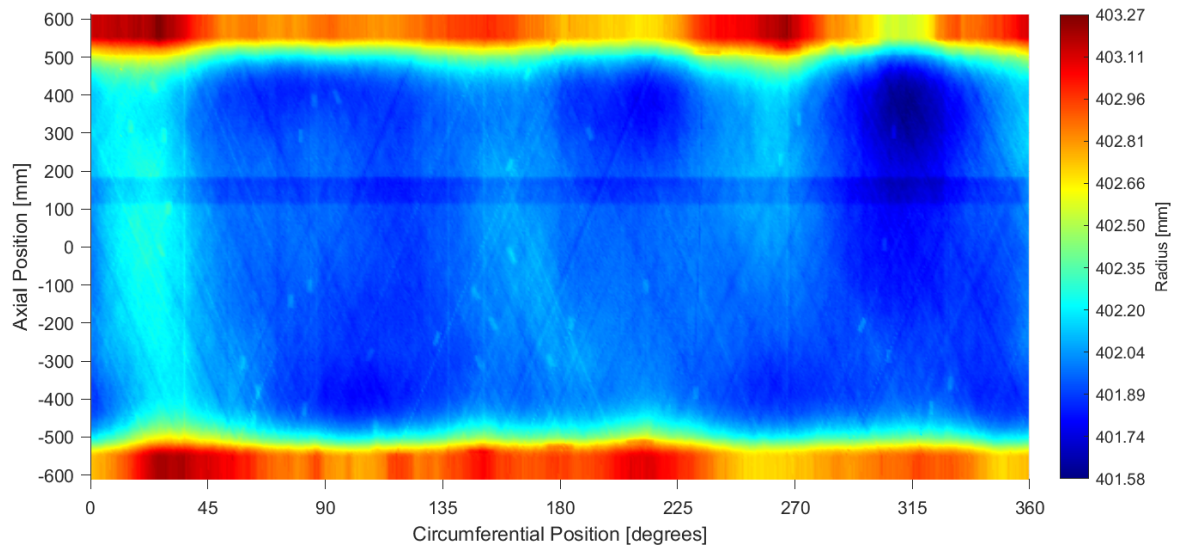


Figure 8.7: Interpolated mid-surface.

## 8.2 Choice of Composite Material Properties for Simulation

The nominal properties of IM7-8552 given in Table 3.2 were modified based on the results of a NASA tensile test, whose specimens had the same  $[(23/0/-23)_{S4}]$  layup as the test article's primary section and were deliberately built for this purpose. Results of the tensile test are given in Table 8.3. The  $0^\circ$  modulus and Poisson's ratio refer to the overall laminate.

Specimen Number		1	2	3	4	5	6	7	Mean
$0^\circ$ Modulus	[GPa]	107.3	108.7	115.0	109.4	106.1	108.8	105.3	108.7
Poisson's ratio	[-]	1.24	1.29	1.29	1.28	1.27	1.31	1.35	1.29
Width	[mm]	25.3	25.4	25.4	25.4	25.4	25.4	25.4	25.4
Thickness	[mm]	4.32	4.32	4.32	4.34	4.32	4.39	4.32	4.32

**Table 8.3:** Summary of the tensile test results from which the calibrated material properties were derived.

To calibrate the nominal properties of IM7-8552 to the tensile test, “digital” tensile test simulations were performed with linear static analysis. The goal of this procedure was to choose  $E_{11}$  and  $E_{22}$  ply property values such that the resultant  $0^\circ$  modulus and Poisson's ratio of the finite element specimen were within 1% of the mean values of the physical test. This calibration was similar to the process used by Schultz et al. [36] when performing analysis for CTA8.1 (although in that case, the experimental calibration reference was a pre-critical load sequence to determine CTA8.1's axial stiffness, rather than the results of a coupon-size tensile test).

Figure 8.8 shows the finite element model of the mean representative experimental tensile specimen cross-section dimensions – 25.4-mm width and 4.32-mm thickness – that was created for calibration. No length was specified in the NASA data, so a length of 200 mm was chosen. The SC8R element was used, with a mesh size of 4.3 mm. The nodes of the left edge of tensile specimen model were constrained in all degrees of freedom. The nodes on the right edge were tied to a reference node (all highlighted in red) via a rigid body tie constraint. This reference node was constrained in all degrees of freedom except for translation in the X direction. A displacement of 0.2 mm (corresponding to a length-wise strain of 0.1%) was applied to the reference node in the positive X direction.

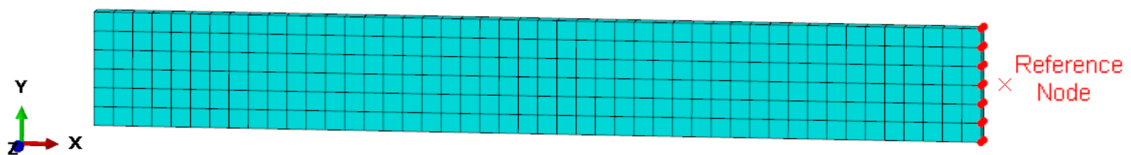


**Figure 8.8:** Finite element model of the representative tensile specimen.

Adjustment of the ply properties was conducted in a two-step process. First, the nominal  $E_{11}$  ply property was tuned so that the resultant  $0^\circ$  modulus of the model matched the mean of the tensile experiment. The resultant modulus from the model was calculated by dividing the reaction load at the reference node by the cross-sectional area and then by the specimen's longitudinal 0.1% strain. Next, the nominal  $E_{22}$  value was adjusted so that the model's resultant Poisson's ratio matched the experimental mean. The Poisson's ratio of

the model was derived from 0° and 90° strains extracted from a central element. Table 8.4 shows the nominal, intermediate, and calibrated  $E_{11}$  and  $E_{22}$  values and differences in the two aforementioned metrics relative to the test.

Version	Ply Property		[(23/0/-23) <sub>S4</sub> ] Laminate Property					
	$E_{11}$ [GPa]	$E_{22}$ [GPa]	0° modulus			Poisson's Ratio		
			Test [GPa]	FEA [GPa]	Difference	Test [-]	FEA [-]	Difference
Nominal	140.9	9.72	108.7	102.1	-6.0%	1.29	1.16	-10.1%
Iteration 1	155.0	9.72		111.1	2.2%		1.24	-4.1%
Iteration 2	152.2	9.72		109.3	0.6%		1.23	-4.8%
Calibrated	152.2	8.75		108.8	0.1%		1.28	-0.9%

**Table 8.4:** Iterations for calibrating the moduli of the ply properties to the tensile test. Percentage differences are taken with respect to the test.

Two iterations of the first step were required to tune  $E_{11}$ . The nominal value was initially increased by 10% to 155.0 GPa; however this resulted in a 0° laminate modulus that differed by more than the 1% threshold. An 8% increase of the nominal  $E_{11}$  was then attempted with success. Only one iteration of  $E_{22}$  adjustment (-10%) was required such that both metrics matched the tensile experiment's means within 1%. The final property set resulting from this process is contained in the last row labeled "calibrated". No other ply properties were adjusted.

After this initial calibration, a set of "recalibrated" properties were determined by scaling up the calibrated  $E_{11}$  and  $E_{22}$  values of Table 8.4 to account for an observed 4.3% difference between the test article's mean primary layup thickness of 4.14 mm and the tensile specimens' mean 4.32-mm thickness (these correspond to mean ply thicknesses of 0.173 mm and 0.180 mm, respectively). Figure 8.9 shows a three-dimensional view of the shell's interpolated thickness compared to an overlay of the shell's nominal thickness (without imperfections) given 0.180-mm thick plies, which further illustrates the discrepancy.

It was thought that this thickness difference was caused by more resin being bled-off in the shell's manufacturing process than that of the tensile specimens. The logic of recalibration was based upon the assumption that a given tow should contain the same quantity of fibers regardless of its cured thickness. It was thus assumed that the load-displacement behavior of a 0.180-mm-thick ply should have nearly identical behavior to that of a 0.173-mm-thick ply. By necessity, this would imply that the 0.180-mm and 0.173-mm plies have different stiffnesses due to the differing cross-sectional area. Thus recalibrated  $E_{11}$  and  $E_{22}$  values were obtained via multiplication of the calibrated  $E_{11}$  and  $E_{22}$  by the ratio of mean tensile specimen ply thickness to mean shell ply thickness, as shown in Equations 8.1 and 8.2. The rest of the properties for the recalibrated material set (e.g. shear moduli), were left the same as the those of nominal and calibrated properties. Failure properties were not adjusted for the calibrated or recalibrated material property sets from their nominal values from Clarkson [58], as this would have required additional assumptions. All three property sets are summarized in Table 8.5.

$$E_{11_{\text{Recalibrated}}} = E_{11_{\text{Calibrated}}} \frac{\text{ply thickness}_{\text{tensile specimen}}}{\text{ply thickness}_{\text{shell}}} = E_{11_{\text{Calibrated}}} * 1.043 \quad (8.1)$$

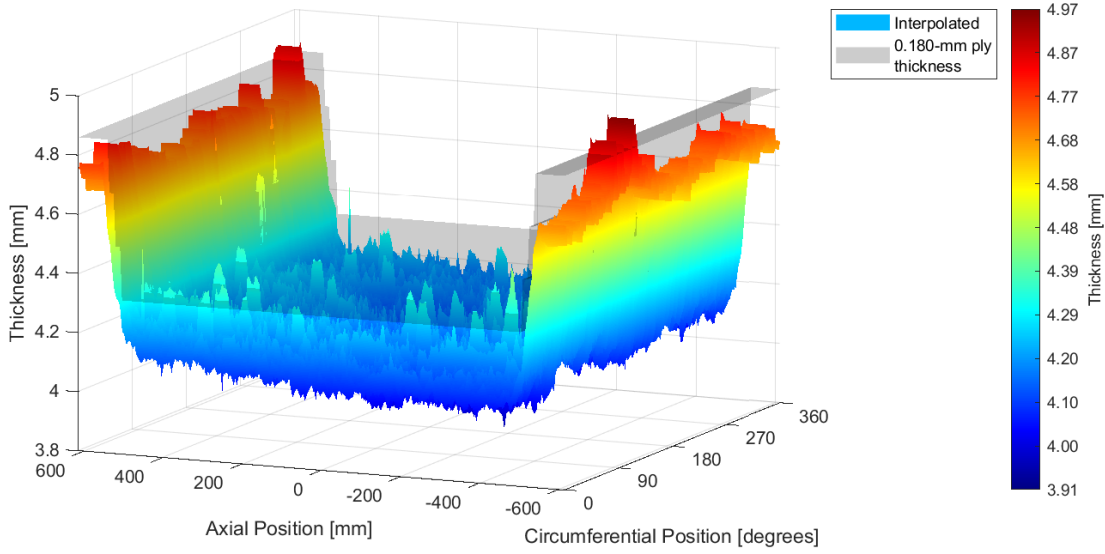


**Figure 8.9:** Interpolated thickness compared with an overlay corresponding to the mean 0.180-mm tensile test ply thickness.

$$E_{22_{\text{Recalibrated}}} = E_{22_{\text{Calibrated}}} \frac{\text{ply thickness}_{\text{tensile specimen}}}{\text{ply thickness}_{\text{shell}}} = E_{22_{\text{Calibrated}}} * 1.043 \quad (8.2)$$

Property Set	$E_{11}$ [GPa]	$E_{22}$ [GPa]	$G_{12}$ [GPa]	$G_{13}$ [GPa]	$G_{23}$ [GPa]	$\nu_{12}$ [-]	$\rho$ [g/cm <sup>3</sup> ]
Nominal	140.9	9.72	4.69	4.69	3.58	0.356	1.58
Calibrated	152.2	8.75	4.69	4.69	3.58	0.356	1.58
Recalibrated	158.7	9.12	4.69	4.69	3.58	0.356	1.58

**Table 8.5:** Material property sets of Hexcel IM7-8552 composite.

The effect of material property and thickness adjustments on the buckling load was investigated to determine if substantial changes were to be expected on the shell *without imperfections*. This was done via both the analytical buckling load calculation of the simplified shell, as well as via nonlinear dynamic analysis of full the test article without imperfections. The latter test article model was produced by forgoing the imperfection surface interpolation mentioned in Section 8.1.2 and prescribing the shell's inner and outer surfaces based on the nominal inner radius and the ply thicknesses of either 0.175 or 0.173 mm. A displacement rate of 2 mm per minute was applied to the reference node.

These results are shown in Table 8.6 and Figure 8.10. As indicated by the percentage differences, the change of materials and ply thicknesses did not affect the buckling load significantly. A slight increase in axial stiffness relative to the nominal material was observed. As a result of the similarity in these buckling loads, the nominal analytical buckling load of 2271 kN was retained as the reference buckling load.

Material	Ply Thickness [mm]	SP-8007		Nonlinear Dynamic	
		Buckling Load [kN]	Difference	Buckling Load [kN]	Difference
Nominal	0.175	2271	[ref]	2197	[ref]
Calibrated	0.173	2219	-2.3%	2131	-3.0%
Recalibrated	0.173	2291	0.9%	2210	0.6%

**Table 8.6:** Effect of adjusting the material properties and ply thickness on the simplified shell analytical buckling load alongside the test article nonlinear dynamic analysis buckling loads without imperfections.

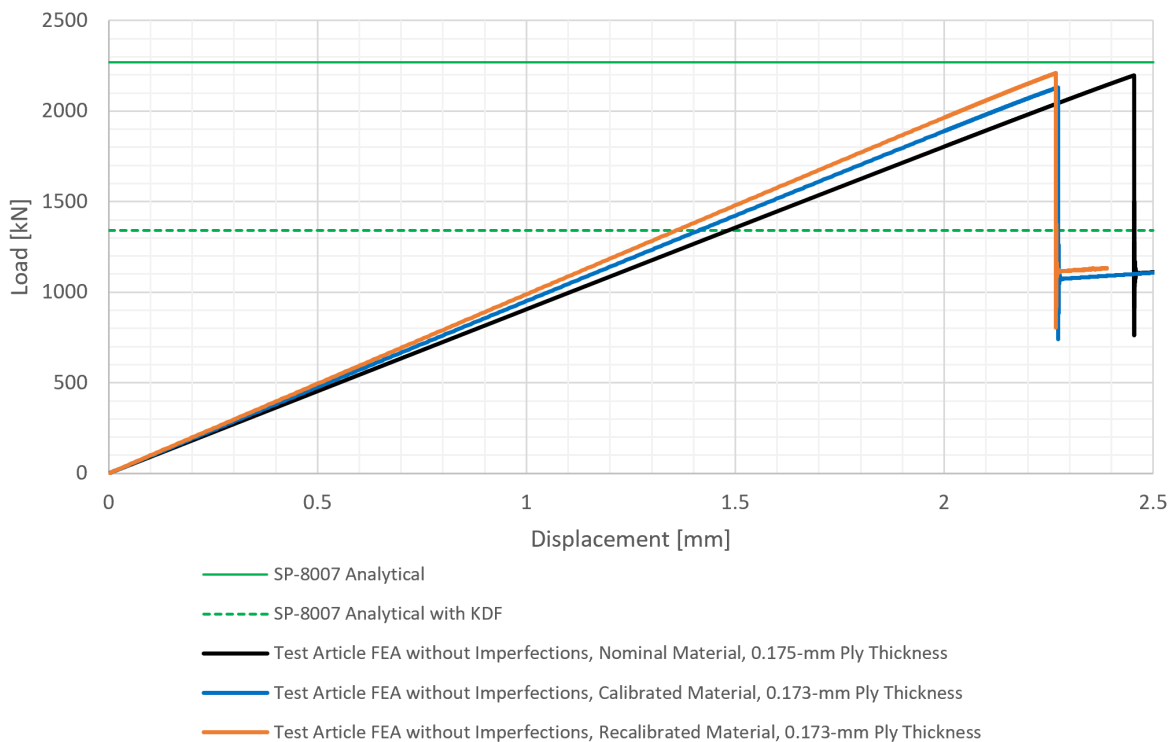


**Figure 8.10:** Effect of different material properties and thickness on the test article without imperfections.

### 8.3 Preliminary NDL-1 Simulation Results with Imperfections

Prior to the buckling experiment of NDL-1, two simulations with measured imperfections were conducted: one with the calibrated property set and one with the recalibrated properties. A displacement rate of 2 mm per minute was applied to the top reference node in the axially compressive direction. Only pre-test data for the recalibrated simulation was provided to NASA for use during the experiment.

The buckling loads and resultant knockdown factors are summarized in Table 8.7. The analytical buckling load of NASA SP-8007 is considered the reference load by which resultant knockdown factors are derived. Figure 8.11 shows the load versus displacement results for the both material variants. Buckling was expected to occur at 2.18 mm of axial compression and at a load between 2075 kN and 2154 kN. These are about 70% and 84% less conservative than NASA SP-8007.

Model	Buckling Load [kN]	KDF
SP-8007 Analytical	2271	-
SP-8007 Analytical with KDF	1338	0.59
Calibrated FEA with Measured Imperfections	2075	0.91
Recalibrated FEA with Measured Imperfections	2154	0.95

**Table 8.7:** Simulation results compared with the SP-8007 analytical solution.

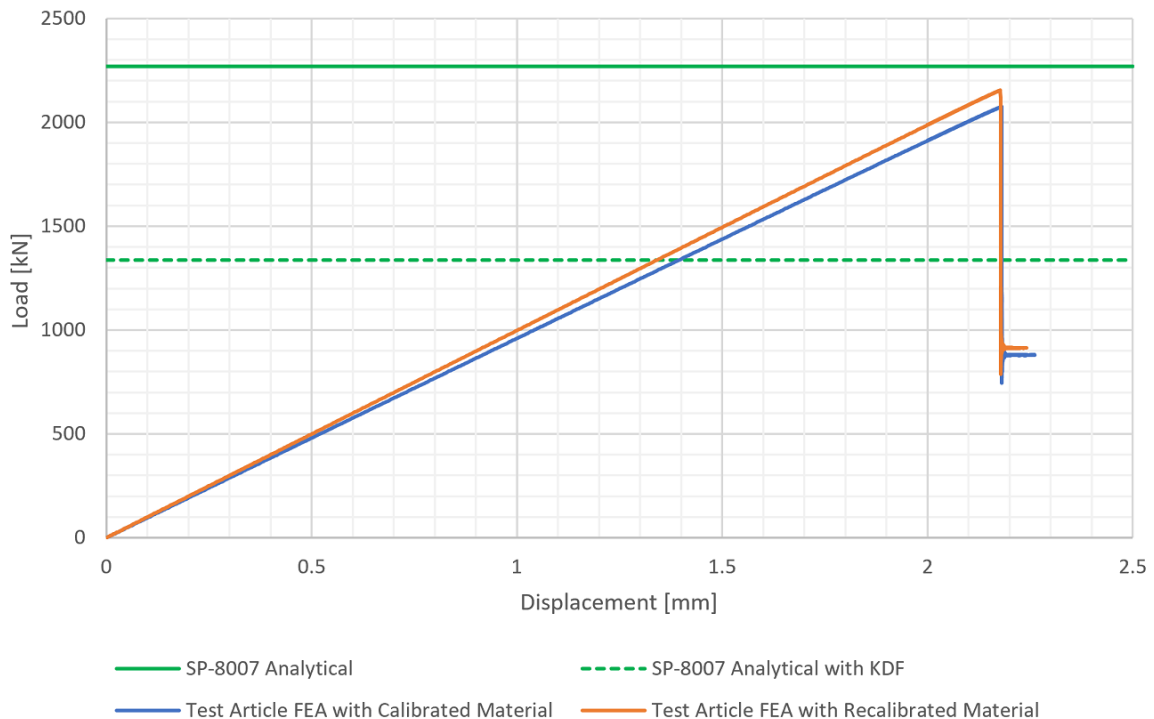


**Figure 8.11:** Load versus displacement plots of the two pre-test simulations with measured imperfections.

Various failure criteria were assessed at the simulation intervals immediately before and after buckling to investigate if any were met or exceeded. The purpose was threefold: to check that material failure would not occur prior to buckling, and to determine when and where failure was expected to occur. This was accomplished by extracting the most critical plies' failure criteria values immediately prior to buckling and immediately after buckling (i.e. before and after the peak load). The points at which these values were extracted from each simulation are specified in Figure 8.12. The most critical values and plies are presented in Tables 8.8 and 8.9. In the case of both materials, failure was not expected to occur before buckling. This is indicated by all pre-buckling criteria values being below unity. However, failure was expected to occur immediately upon buckling, as indicated by the presence of greater-than-unity criteria values in the post-buckling columns of these tables.

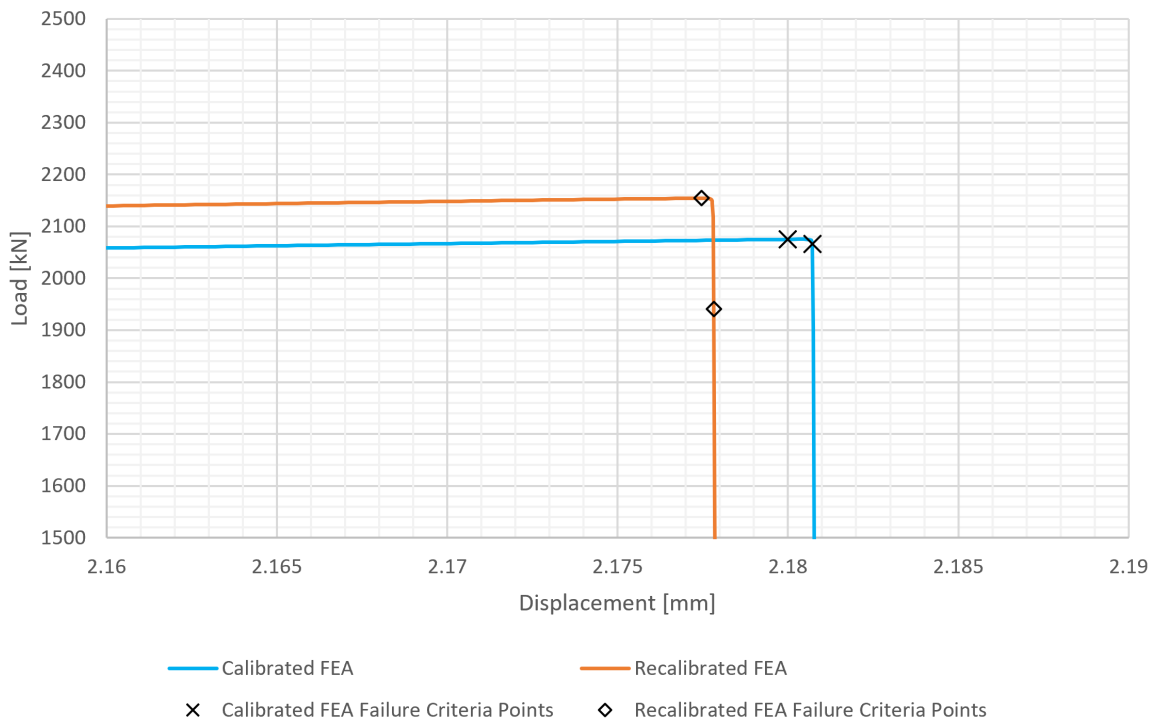


**Figure 8.12:** Pre-buckling and post-buckling points used for extracting failure criteria.

Failure Criteria	Most Critical			
	Pre-buckling Value	Ply #	Post-buckling Value	Ply #
Maximum Stress	0.36	1	1.00	24
Maximum Strain	0.50	2	1.12	24
Tsai-Hill	0.46	3	1.03	24
Tsai-Wu	0.52	3	1.08	24
Hashin Fiber Compressive	0.05	23	0.20	24
Hashin Fiber Tensile	0.02	90° pad-up	0.04	1
Hashin Matrix Compressive	0.08	-45° pad-up	0.61	1
Hashin Matrix Tensile	0.19	3	1.06	24

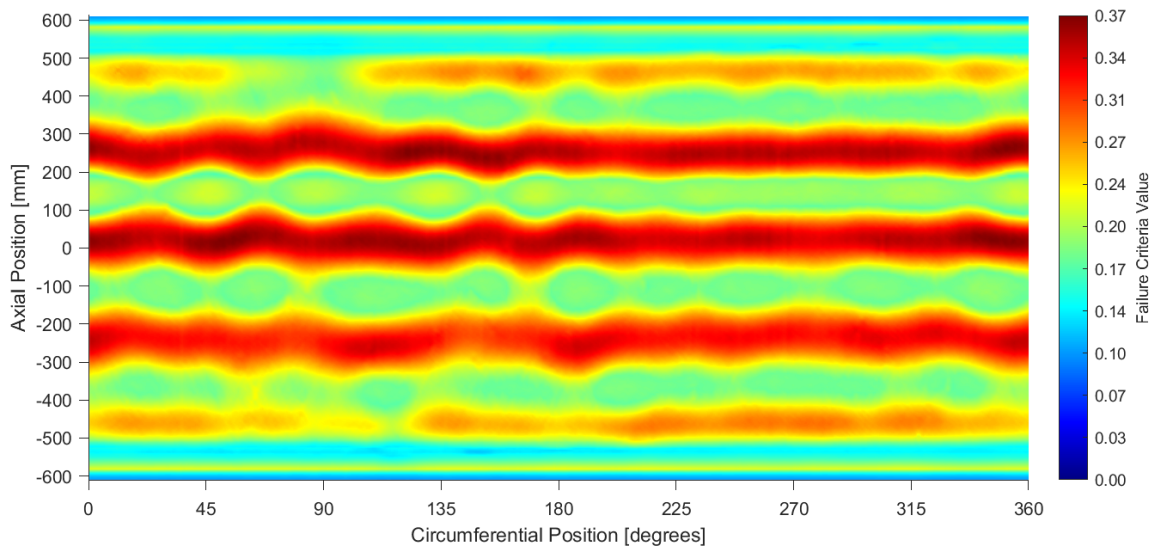
**Table 8.8:** Failure criteria of the calibrated simulation.

Failure Criteria	Most Critical			
	Pre-buckling		Post-buckling	
	Value	Ply #	Value	Ply #
Maximum Stress	0.37	23	1.65	24
Maximum Strain	0.50	2	1.63	23
Tsai-Hill	0.47	3	1.82	24
Tsai-Wu	0.54	3	1.87	24
Hashin Fiber Compressive	0.05	23	0.40	1
Hashin Fiber Tensile	0.02	90° pad-up	0.14	24
Hashin Matrix Compressive	0.08	-45° pad-up	0.97	1
Hashin Matrix Tensile	0.21	3	3.28	24

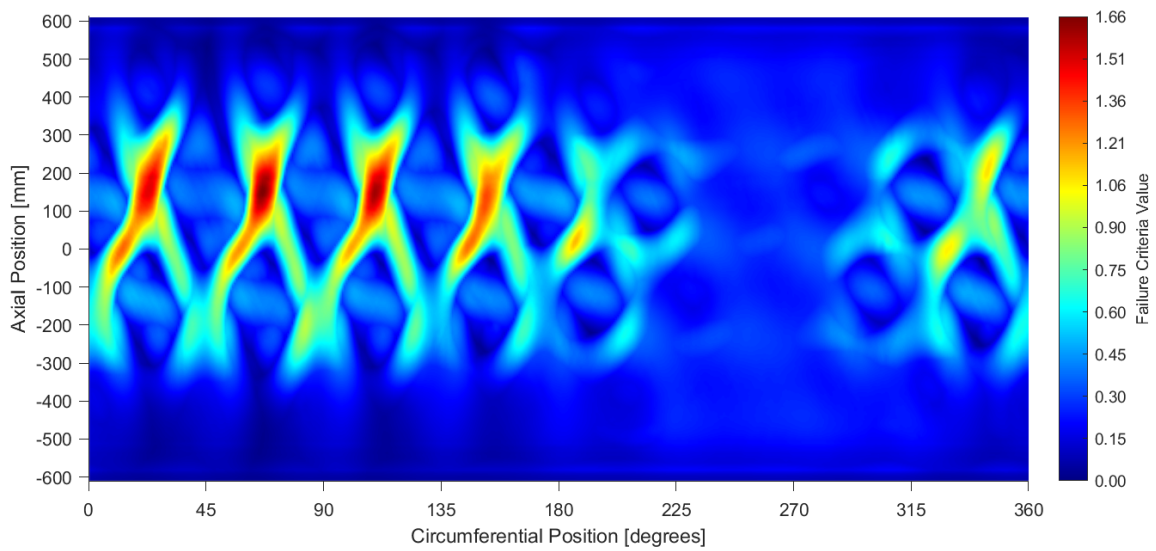
**Table 8.9:** Failure criteria of the recalibrated simulation.

Two categories of failure criteria and one of damage initiation were assessed: maximum allowable, energy-based, and component-damage based. Maximum strain and stress criteria consider the corresponding allowables; if the strength or strain value is exceeded, the criterion indicates failure. The Tsai-Hill criterion is energy-based and considers the interaction of component stresses, just as the von Mises criterion does with isotropic materials [55, 60]. The Tsai-Wu criterion built upon Tsai-Hill by allowing for different strength allowables in tension and compression [60]. Hashin-Rotem potentially has more physical significance than Tsai-Wu and Tsai-Hill in that it considers failure of the fiber and matrix material separately. By contrast, the maximum allowable and energy-based criteria make the simplification of homogeneity [55, 60, 61]. For the calibrated simulation, Tsai-Wu is the most conservative (i.e. has the highest value) in both pre- and post-buckling as indicated in Table 8.8. For the recalibrated simulation Tsai-Wu is also the most conservative in pre-buckling, but the Hashin Matrix Tensile criterion is most conservative in post-buckling, as indicated in Table 8.9.

Potential sites for failure initiation in the recalibrated simulation are indicated by the maximum criteria values in Figures 8.13 through 8.15. These figures, showing one of each category of the aforementioned criteria for pre- and post-buckling, are generally in agreement and suggest that failure may be expected to occur at axial positions between approximately 100 mm and 200 mm, and at circumferential positions of approximately 23°, 68°, or 113°. Figure 8.16 indicates the radial displacement corresponding to the increment at which post-buckling failure contours were taken. In combination with the failure criteria figures, it suggests that failure is expected to occur at locations of outward radial displacement.

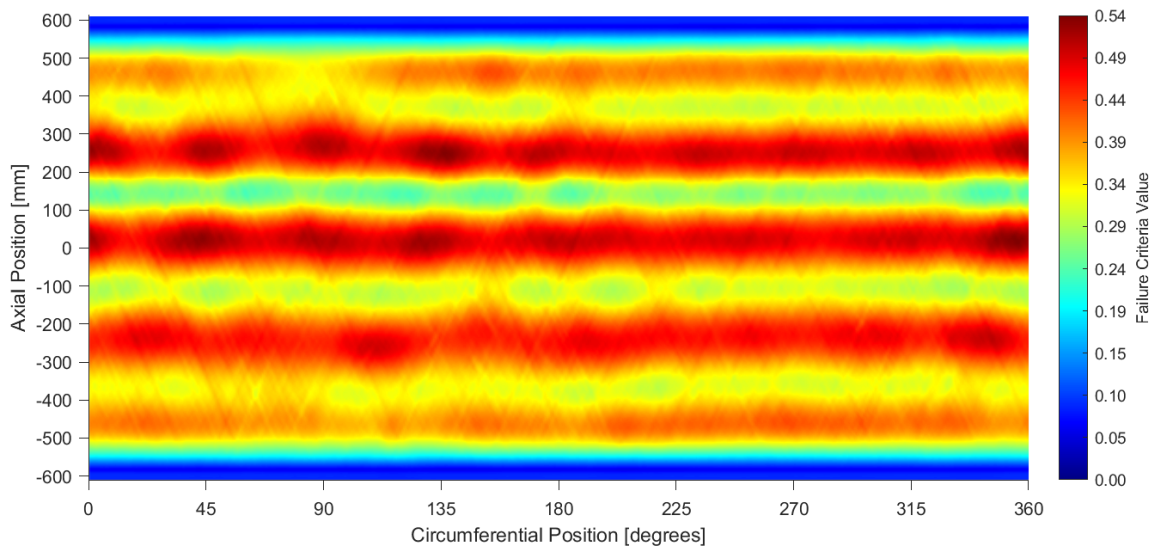


(a) Pre-buckling, Ply 23.

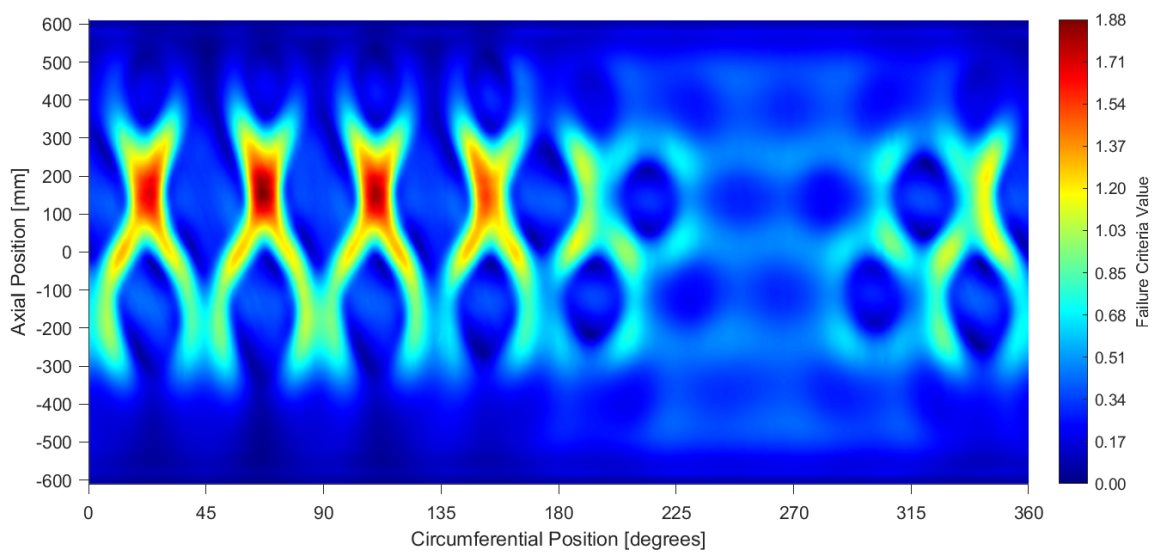


(b) Post-buckling, Ply 24.

**Figure 8.13:** Most critical plies of the recalibrated simulation according to the Maximum Stress criterion.

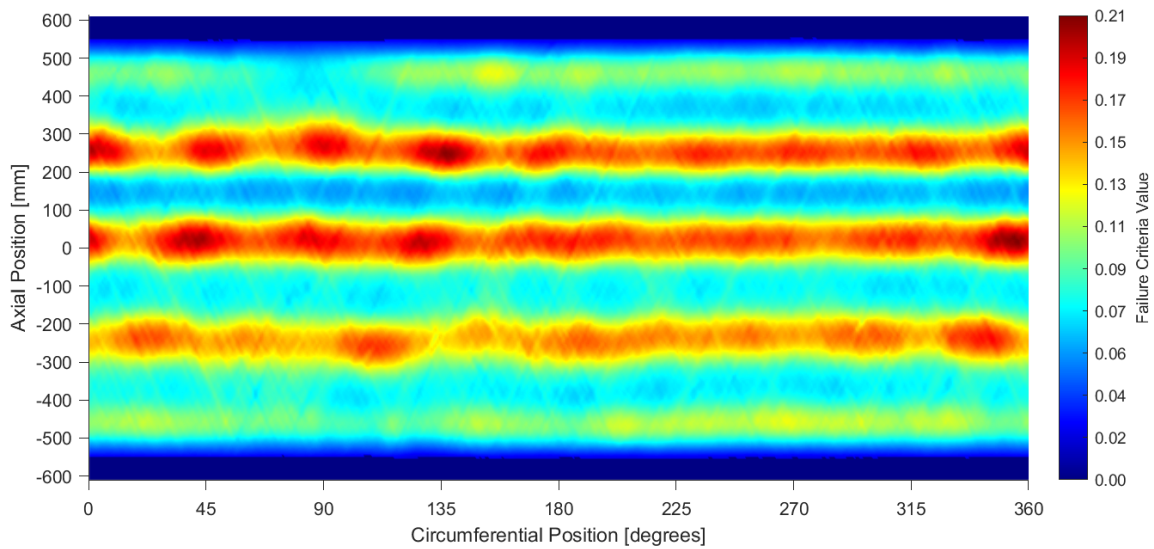


(a) Pre-buckling, Ply 3.

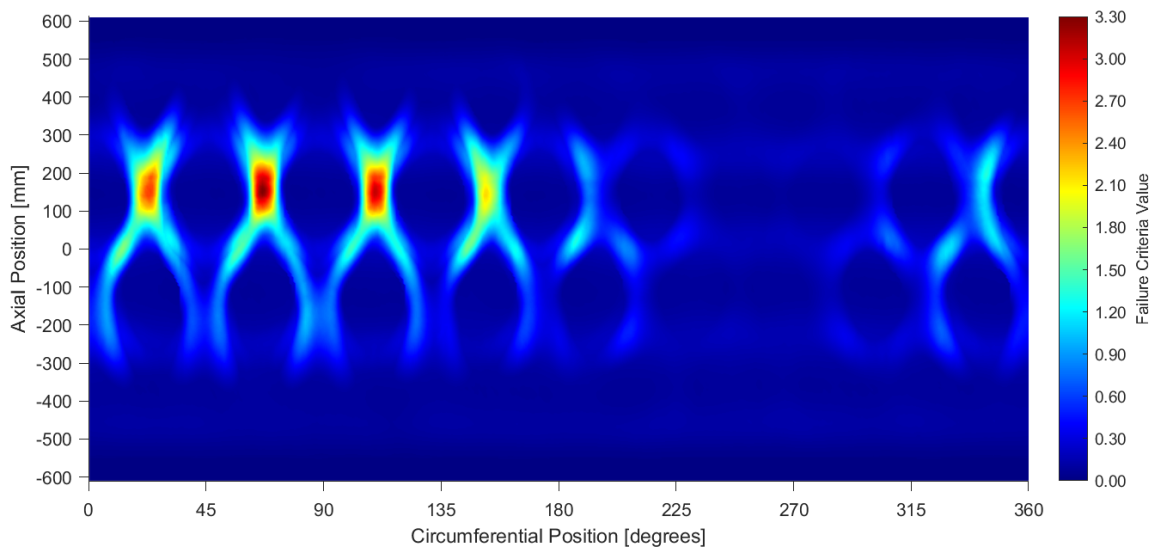


(b) Post-buckling, Ply 24.

**Figure 8.14:** Most critical plies of the recalibrated simulation according to the Tsai-Wu criterion.



(a) Pre-buckling, Ply 3.



(b) Post-buckling, Ply 24.

**Figure 8.15:** Most critical plies of the recalibrated simulation according to the Hashin Matrix Tensile damage criterion.

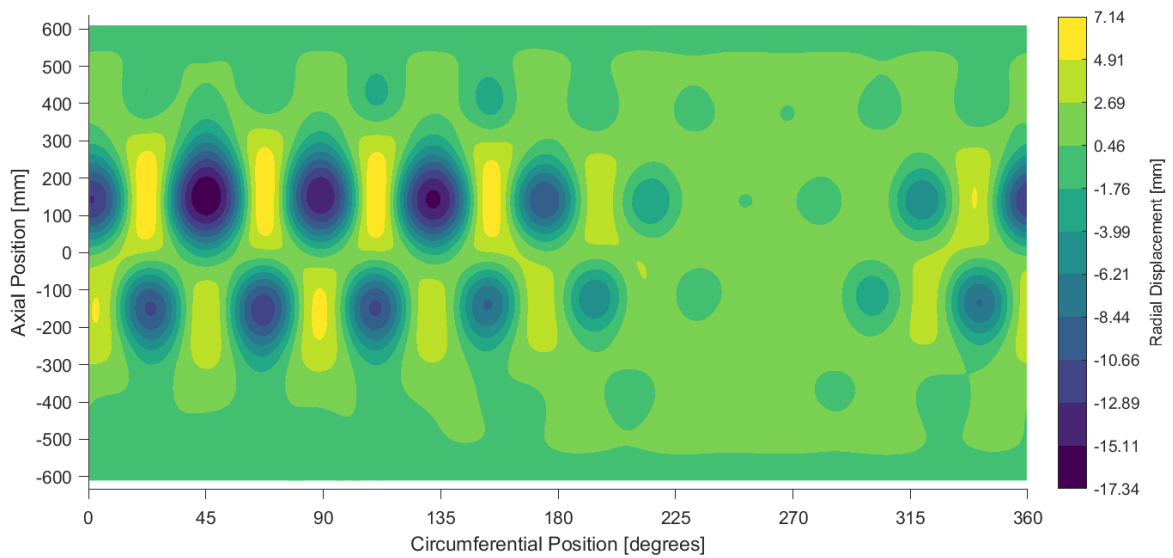
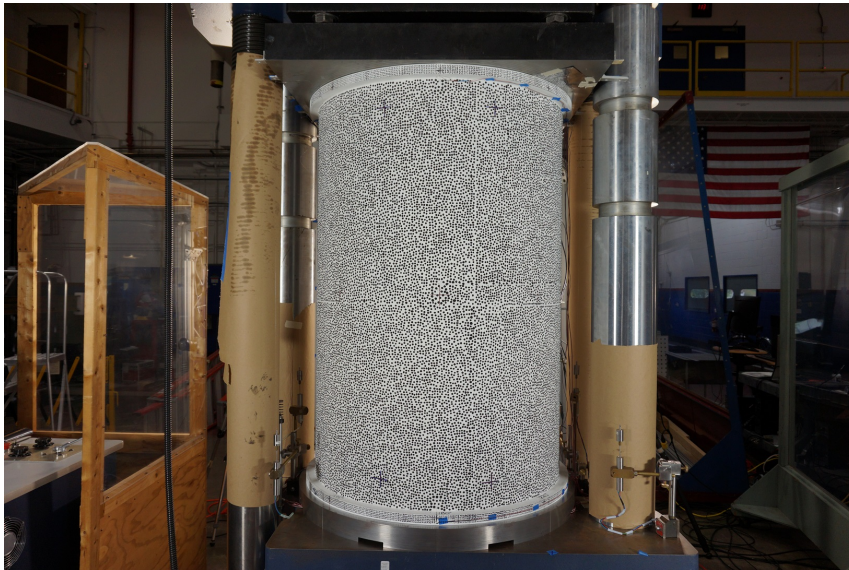


**Figure 8.16:** Radial displacement corresponding to the post-buckling increment at which failure criteria were assessed.



# Experimental Results & Simulation Correlation

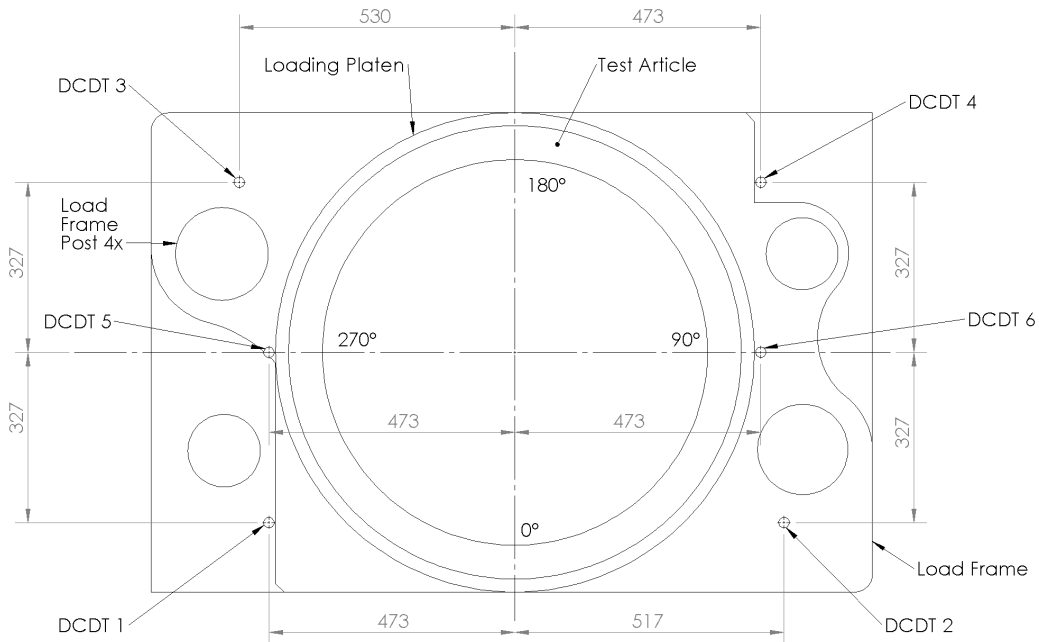
An axial compression buckling test was performed by NASA on NDL-1 in June 2019. The test article is shown in the load frame before testing in Figure 9.1. A displacement-controlled compression rate of approximately 0.04 mm/min was applied. The test article was loaded to failure, which as indicated in Section 8.3 was expected immediately upon buckling. Results from the experiment are explored in this chapter and compared with the simulations.



**Figure 9.1:** NDL-1 mounted in the load frame at NASA Langley Research Center prior to testing (photo courtesy of NASA).

Test data came from several sources. Load was measured via a load cell. Displacement was measured by six direct current differential transducers (DCDTs) positioned around the load frame, two of which are visible next to the bases of the two front columns in Figure 9.1. All

DCDT locations are specified in Figure 9.2, along with the circumferential orientations that are referenced throughout this chapter.



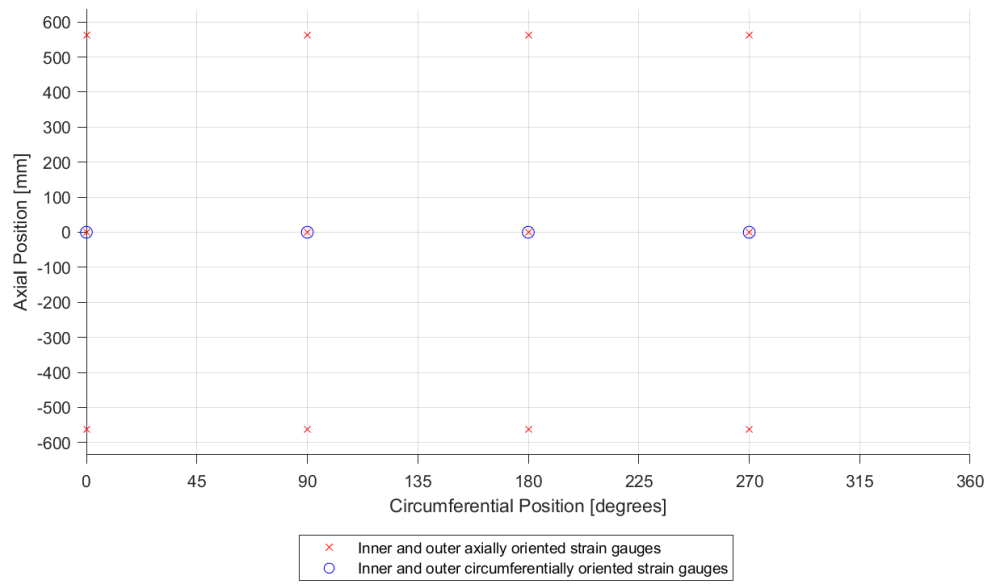
**Figure 9.2:** Mid-section top-view drawing of the load frame indicating angular locations and DCDT mounting points. All dimensions are in millimeters.

Figure 9.3 shows the locations and orientations of strain gauges that were affixed to ND1-1. On both the inner and outer surfaces, 12 axially oriented gauges were spaced at regular intervals: every permutation of  $0^\circ$ ,  $90^\circ$ ,  $180^\circ$ , and  $270^\circ$  around the circumference with axial positions of  $-562$  mm,  $0$  mm (the meridian), and  $562$  mm. Additionally, four inner and four outer meridian gauges measured circumferential strain at  $0^\circ$ ,  $90^\circ$ ,  $180^\circ$ , and  $270^\circ$ .

Eight digital image correlation (DIC) systems observed the experiment: four low-speed and four high-speed systems, with each system comprised of two cameras. Pairs consisting of one low-speed and one high-speed system were positioned facing circumferential positions of the shell at  $45^\circ$ ,  $135^\circ$ ,  $225^\circ$ , and  $315^\circ$  as indicated in Figure 9.4. As single set of cameras from one such pair is shown in Figure 9.5. All DIC systems' fields of view were centered on ND1-1's meridian. Images from set of systems were digitally merged. Low-speed DIC recorded the experiment at one frame per second. Pre-buckling radial and axial displacements were derived from this data. High-speed DIC captured the buckling event at 20,000 frames per second. The DIC speckle pattern visible in Figure 9.1 was applied after imperfection measurements were taken and strain gauges were mounted.

The experimental setup is shown Figure 9.6. Monitoring stations were used to observe full-field displacements and strains from low-speed DIC along with load and axial displacements in real time. A sawtooth wave provided a common synchronization signal for all data sources.

Before the final load sequence, shims were introduced between the upper edge of ND1-1 and the upper loading platen to achieve the best possible uniformity of load transfer. The positions and amounts of shimming shown in Table 9.1 were determined after assessing DIC data during preliminary sub-critical load sequences.



**Figure 9.3:** Strain gauge locations and orientations on the shell.

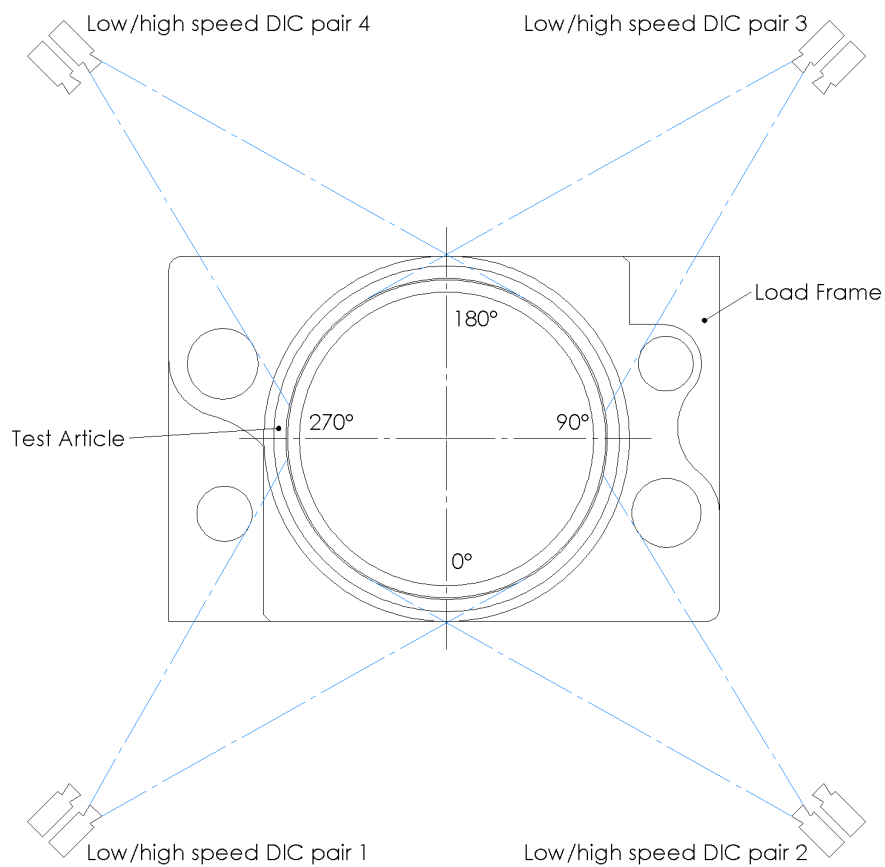


**Figure 9.4:** Locations of DIC systems. Approximate fields of view are indicated by blue lines.

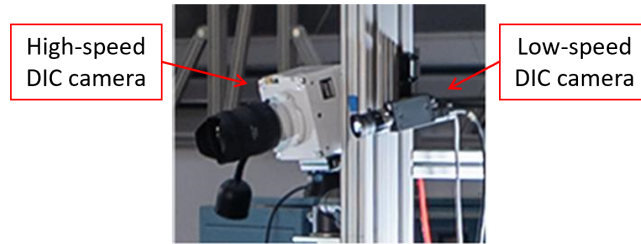


**Figure 9.5:** A pair of DIC cameras (photo courtesy of NASA).

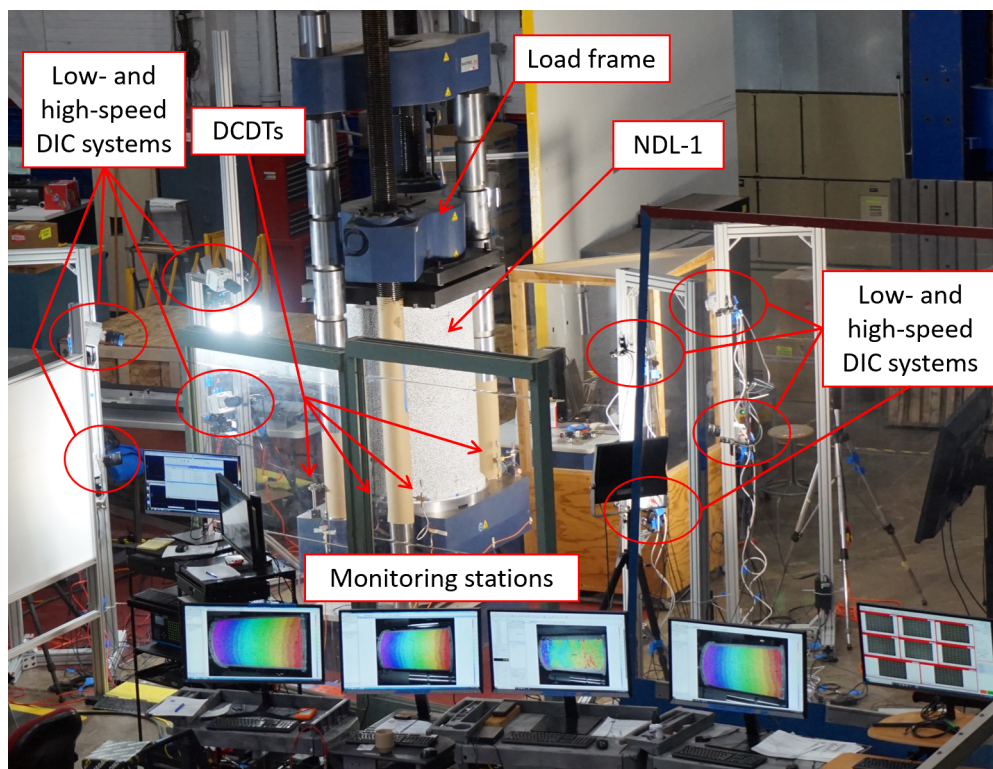


**Figure 9.6:** The experimental setup (photo courtesy of NASA).

Circumferential Position	Shim Height [mm]
210° - 225°	0.0254
225° - 285°	0.0508
285° - 300°	0.0254
300° - 315°	0.0127

**Table 9.1:** Shimming added around the upper edge of NDL-1 prior to the final load sequence.

## 9.1 Load-Displacement

The experimental buckling load is compared with both simulations in Table 9.2. Both simulations match well with the test, particularly the calibrated simulation with agreement within 0.1%. The experimentally obtained KDF is in better agreement with the observations of Singer et al. [62] – who distinguished different KDF curves based on expertise of manufacturing – than the SP-8007-prescribed 0.59 KDF. According to Singer et al., an expertly made shell with an equivalent radius-to-thickness ratio of 300 (this equivalent ratio is used for composite shells) is expected to have a buckling load ratio of approximately 0.8.

Source	Buckling Load [kN]	Error	KDF with respect to SP-8007
Experimental	2077	[ref]	0.91
Calibrated FEA with Measured Imperfections	2075	-0.08%	0.91
Recalibrated FEA with Measured Imperfections	2154	3.7%	0.95

**Table 9.2:** Experimental buckling load result of ND1-1 compared with FEA results.

Figure 9.7 shows the load-displacement behavior as derived from DCDTs. The displacement at buckling and pre-buckling stiffnesses indicated by the DCDTs do not qualitatively match either simulation well.

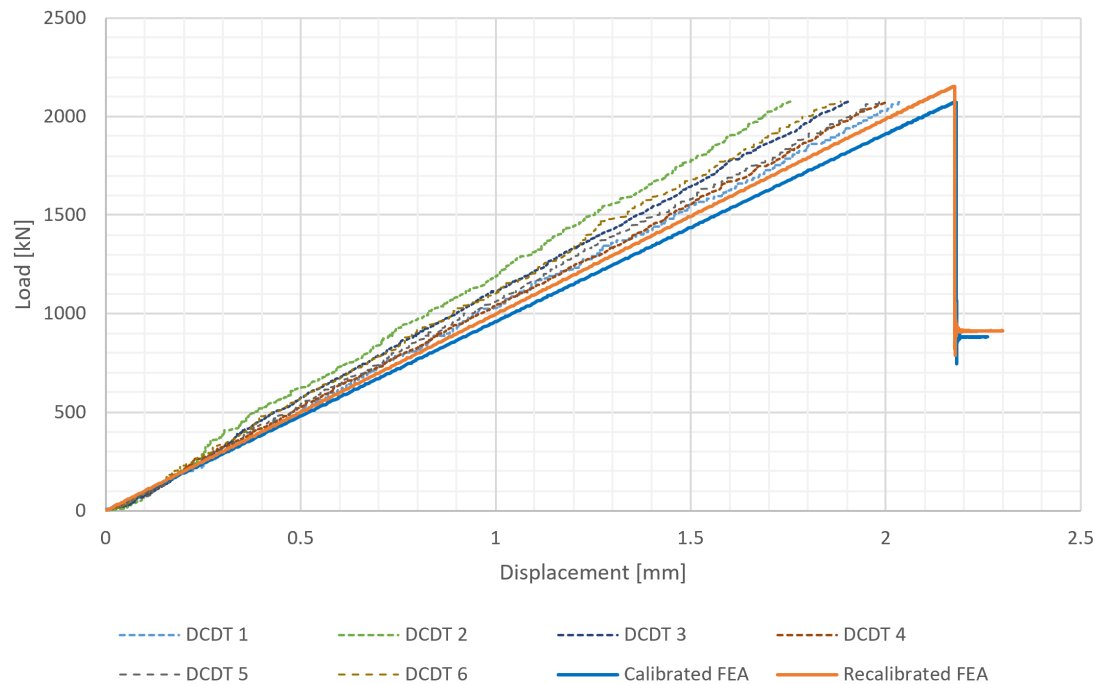


**Figure 9.7:** DCDT load-displacement behavior compared with both simulations.

This was initially puzzling because of the excellent to-be-discussed load-strain agreement between simulation and experiment. Thus an additional set of axial displacement data was obtained from low-speed DIC at circumferential positions of  $45^\circ$ ,  $135^\circ$ ,  $225^\circ$ , and  $315^\circ$ . Figure 9.8 shows the average displacement from these positions. This axial displacement DIC data

shows much better agreement with the simulations than the DCDT data.

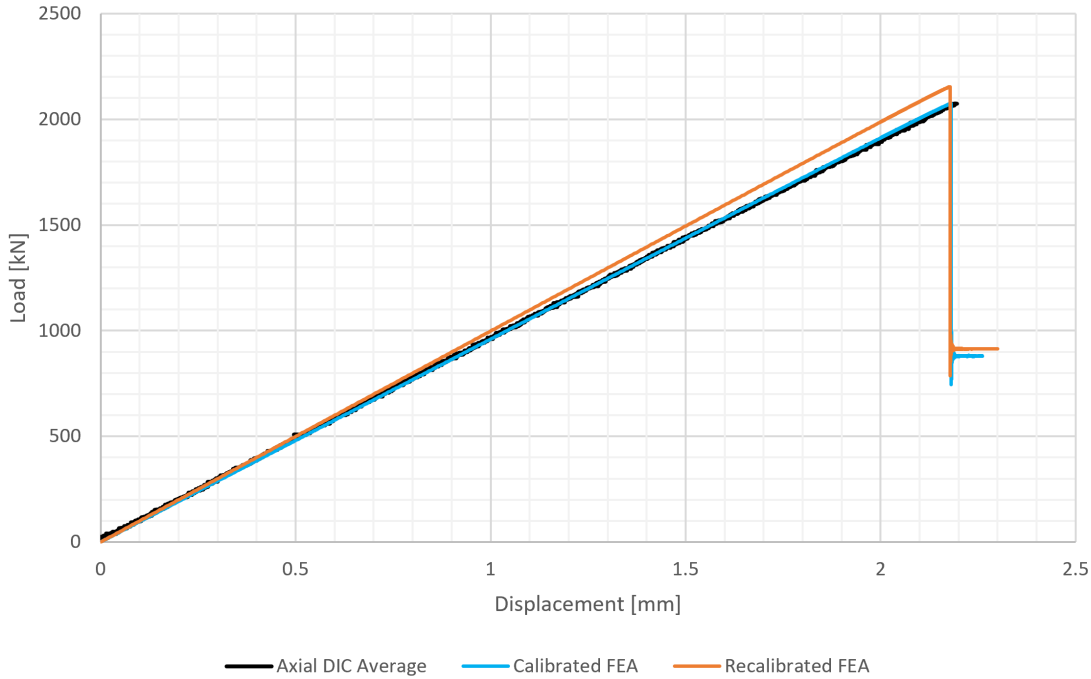


**Figure 9.8:** Averaged axial DIC-derived load-displacement behavior compared with both simulations.

The correlation is quantitatively confirmed by the simulated and experimental pre-buckling stiffnesses given in Table 9.3. These axial stiffnesses were acquired via the slope of linearly best-fitting the data sets. Data points after buckling were excluded from this fitting procedure. The first 0.25 mm of imposed displacement was also eliminated from fitting due to settling at the beginning of the test. Both simulations match well with the experimental stiffness obtained via DIC, yielding agreements within 0.2% and 3.7% for the calibrated and recalibrated simulations, respectively. It was thought that the DCDT displacement measurements were inaccurate due to the test article's high stiffness. As a result of the stiffness, the treatment of the load frame as rigid relative to ND1-1 was likely an invalid assumption. Since the DCDTs were mounted to the load frame, they thus would have incorporated deformation of both the test article and the frame.

Source	Stiffness [kN/mm]	Difference
Experimental - Axial DIC	955	[ref]
Experimental - Average DCDT	1089	14%
Calibrated FEA with Measured Imperfections	953	-0.2%
Recalibrated FEA with Measured Imperfections	990	3.7%

**Table 9.3:** Simplified linear stiffness of the ND1-1 experiment via DCDT and axial DIC compared with both FEA results.

Figure 9.9 allows for investigation of possibility of loading imperfections via the separate 45°, 135°, 225°, and 315° DIC information. Linear fits were generated for displacements

greater than 2 mm to discern circumferential variations in axial displacement leading up to buckling. Displacement values corresponding to the buckling load are given in Table 9.4. The variations from 2.170 mm to 2.214 mm indicate a slight loading imperfection may have been present. From the values in this table, a best-fit plane was derived to represent the potential orientation of the outer upper edge of NDL-1 at buckling, as shown in Figure 9.10. If the axial DIC information and fits are accurate, this indicates that at a circumferential position of  $151^\circ$ , there may have been up to a  $0.003^\circ$  tilt to the shell at the moment of the peak load. It is also possible that the boundary non-uniformity as measured by DIC did not conform to a planar shape due to potential deformation of the load frame.

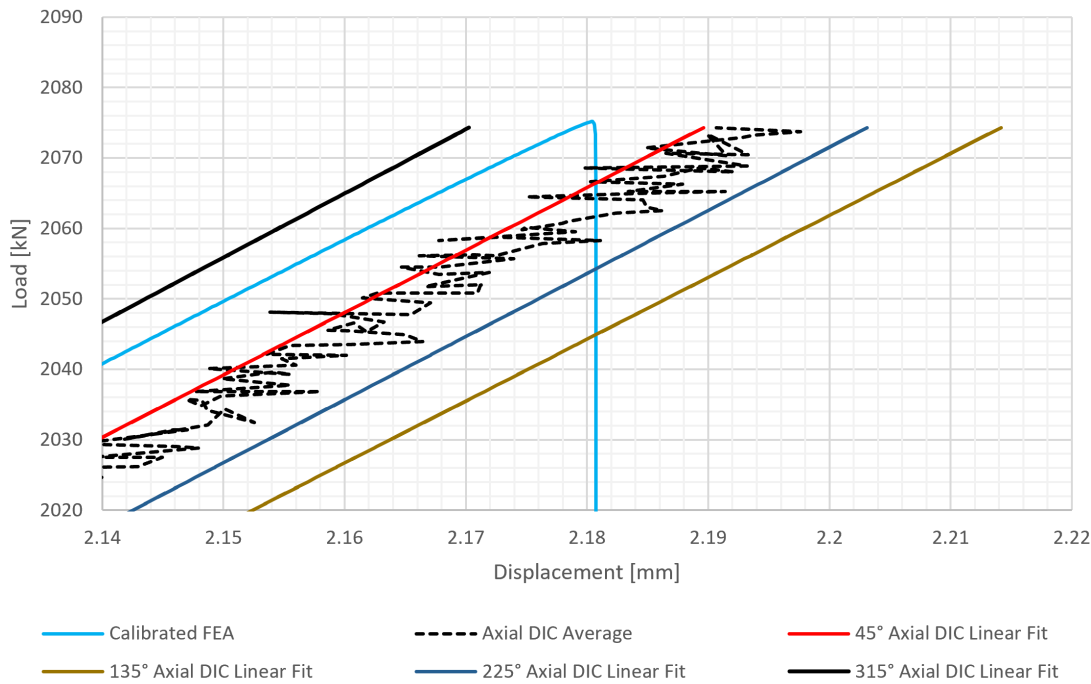


**Figure 9.9:** Linear-fit axial DIC-derived load-displacement behavior at four circumferential locations, compared with average DIC displacement and the calibrated simulation.

Source	Displacement at Buckling [mm]	Difference
Experimental - Axial DIC Average Linear Fit	2.194	[ref]
Experimental - Axial DIC $45^\circ$ Linear Fit	2.190	-0.21%
Experimental - Axial DIC $135^\circ$ Linear Fit	2.214	0.91%
Experimental - Axial DIC $225^\circ$ Linear Fit	2.203	0.40%
Experimental - Axial DIC $315^\circ$ Linear Fit	2.170	-1.10%
Calibrated FEA with Measured Imperfections	2.180	-0.63%
Recalibrated FEA with Measured Imperfections	2.177	-0.77%

**Table 9.4:** Displacement at buckling.

The effect of the potential planar tilt illustrated by Figure 9.10 was investigated through two post-test simulations. Both the calibrated and recalibrated nonlinear dynamic simulations with measured imperfections were re-run, but with the additional application of rotation

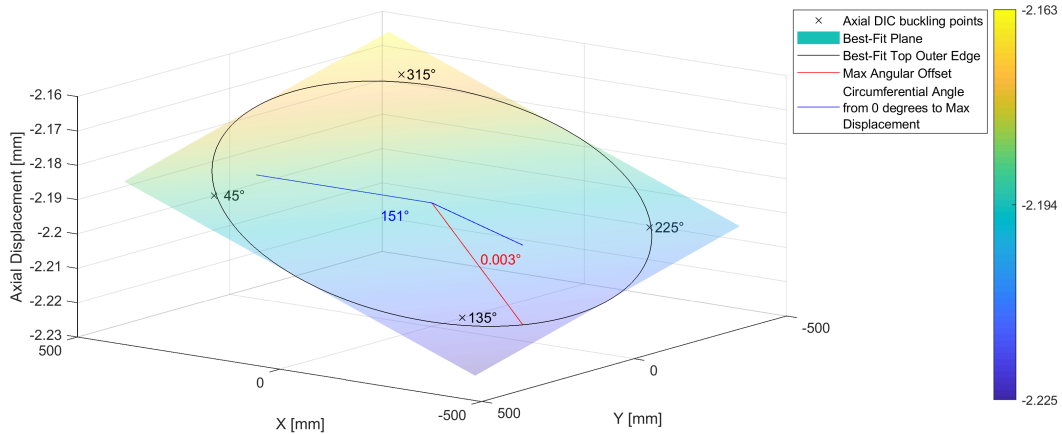


**Figure 9.10:** Best-fit plane to the linearized axial DIC data representing the plane of the top edge of shell at buckling, from Table 9.4.

to the upper reference node towards the model's  $151^\circ$  circumferential position. This was accomplished by linearly increasing the angular tilt of the reference node from  $0^\circ$  to  $0.003^\circ$  during the first 2 mm of axial compression. For axial displacement beyond 2 mm, the  $0.003^\circ$  was then held constant.

The buckling loads of these simulations with loading imperfections are presented in Table 9.5 in comparison to the experimental result as well as the simulation results without the loading imperfections. The inclusion of the planar tilt in simulations did not cause a substantial reduction in the buckling load. The portion of load-displacement behavior around the moment of buckling is shown in Figure 9.11. The only qualitatively observed difference between the simulations with the loading imperfection and without was that the former buckled with 0.18 mm less of axial compression. Up until buckling, the load-displacement curves appeared nearly identical to the simulations without loading imperfections.

Source	Buckling Load [kN]	Error
Experimental	2077	[ref]
Calibrated FEA with Measured Imperfections	2075	-0.08%
Calibrated FEA with Measured Imperfections & Load Imperfection	2061	-0.78%
Recalibrated FEA with Measured Imperfections	2154	3.7%
Recalibrated FEA with Measured Imperfections & Load Imperfection	2139	3.0%

**Table 9.5:** Experimental buckling load result compared with FEA with and without loading imperfections.

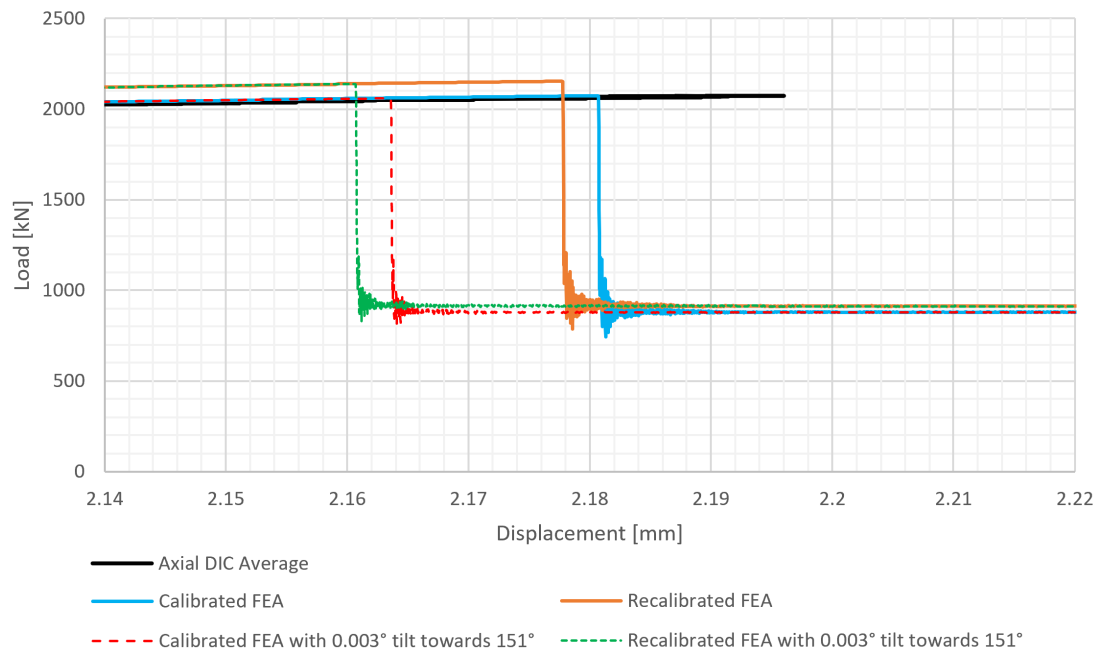


**Figure 9.11:** Comparison of adding a planar tilt to the simulations with measured imperfections.

## 9.2 Load-Strain

To obtain simulation strains corresponding to the precise gauge locations in Figure 9.3, a multi-step process was employed. This was because the footprint of each gauge overlapped areas contained by multiple elements in the FE models. Furthermore the strain gauges' centers did not coincide with the centers of element faces. First, strain history output was requested for the nodes of each element face analogous to shell acreage covered by a gauge (including partially covered elements); this was between six and nine elements per gauge. For each given gauge location, the distance from its center to each associated elements' inner or outer face centers was calculated. Finally, the inverse of this distance was used as a weight to compute the weighted average of simulation strains corresponding to each gauge location. Thus the closer an element's face center to the strain gauge location, the more influence it had on the calculated strain.

Per axial/circumferential strain measurement location, membrane strains were derived by averaging the inner and outer strains. Bending strains were computed as half the difference between inner and outer strains.

Figure 9.12 indicates good agreement between the meridian axial membrane strains of the simulation and test. There was a slightly larger spread in the experimental strains around the circumference than in simulation. This may have been partially due to variations in loading around the circumference of the test article. However, the higher strains at  $0^\circ$  and  $180^\circ$  than  $90^\circ$  and  $270^\circ$  suggest that if a loading imperfection was present, it may not have been a simple planar tilt as indicated in Section 9.1. The meridian axial membrane strain behavior was primarily linear, with some nonlinearity occurring right before buckling.

The meridian circumferential membrane strains are compared in Figure 9.13. The analysis correlated well with the experiment. As with the meridian axial membrane strains, the test article exhibited lower strain at the  $0^\circ$  and  $180^\circ$  positions than at the  $90^\circ$  and  $270^\circ$  positions. All circumferential strains were higher than the axial strains for a given load level. This was expected due to the  $[(23/0/-23)_{S4}]$  layup having greater axial stiffness than circumferential stiffness. These strains obeyed a similar trend as the axial membrane strains above: primarily linear behavior up to 1500 kN followed by a nonlinear region between 1500 kN and the buckling load.

The meridian axial bending strains are shown in Figure 9.14. The simulation correlated well with the experiment in terms of the nonlinear load-strain behavior. Both indicate that little axial bending occurred at the meridian below 1500 kN, after which the amount of bending increased drastically. The experimental spread in this bending strain was likely due to the influence of the imperfection signature's circumferential variance.

Figures 9.15 and 9.16 show the axial membrane strains in the lower and upper pad-up regions, respectively. The lower experimental strains showed little variation in stiffness and good agreement with the simulation. Figure 9.16 indicates a larger experimental spread in stiffness at the upper gauge position, with the  $0^\circ$  and  $180^\circ$  gauges showing greater compliance than the  $90^\circ$  and  $270^\circ$  gauges, similar to the meridian axial membrane strains. This spread was not predicted by the simulation, which showed a more consistent behavior among the circumferential positions.

Bending strains at the lower and upper pad-ups are shown respectively in Figures 9.17 and 9.18. The test and simulation were in better agreement at the lower pad-up than the upper

pad-up. In particular, the  $0^\circ$  and  $270^\circ$  upper pad-up gauges indicated less bending compliance than the simulation predicted. This may have been caused by slight asymmetries in load introduction. The jagged upper  $90^\circ$  experimental bending strain curve in Figure 9.18 was thought to have been caused by a partial detachment of the inner gauge around 900 kN.

In Figures 9.19 through 9.21, the load versus average strain from each axial position (i.e. a set of  $0^\circ$ ,  $90^\circ$ ,  $180^\circ$ , and  $270^\circ$  measurements) are compared with both simulations. Figure 9.19 shows the averaged axial membrane strains. Notably, the meridian strains were higher than the upper and lower strains. This was likely due to the upper and lower gauge positions corresponding to the third pad-up regions, which have three more plies than the primary layup at the meridian. Both simulations showed good agreement with the experimental results, although the calibrated material appears to have given slightly closer results for all three axial locations. The recalibrated simulation appeared slightly stiffer than the test article from the standpoint of strain gauges.

On the basis of averaged circumferential membrane strains per Figure 9.20, the test result indicated higher stiffness than either simulation. The average axial bending strains in Figure 9.21 showed a generally close match between the test and simulations, with the exception of the upper axial bending stiffness.

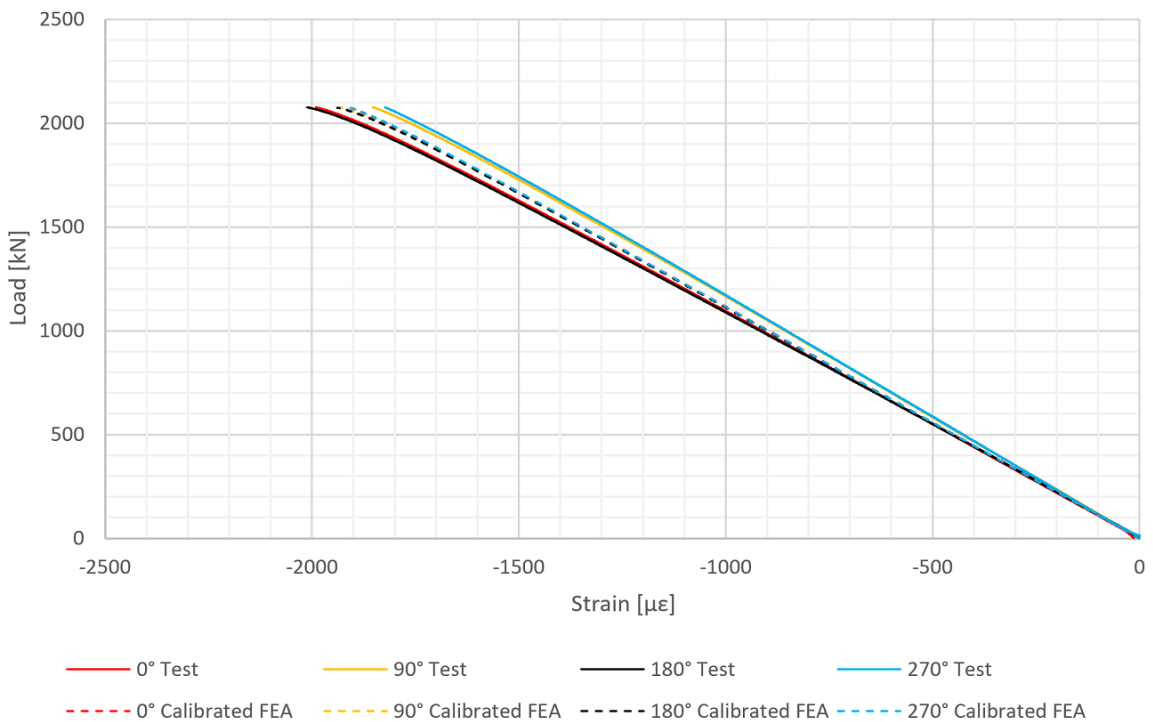


**Figure 9.12:** Meridian axial membrane strains.

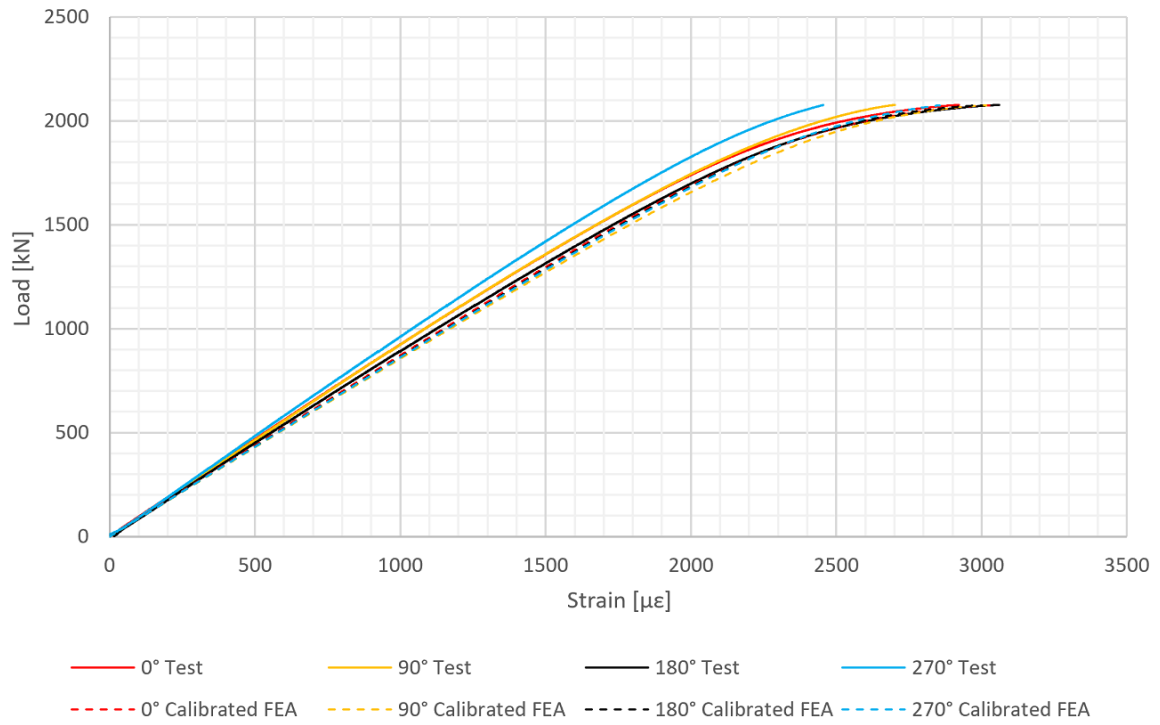


Figure 9.13: Meridian circumferential membrane strains.

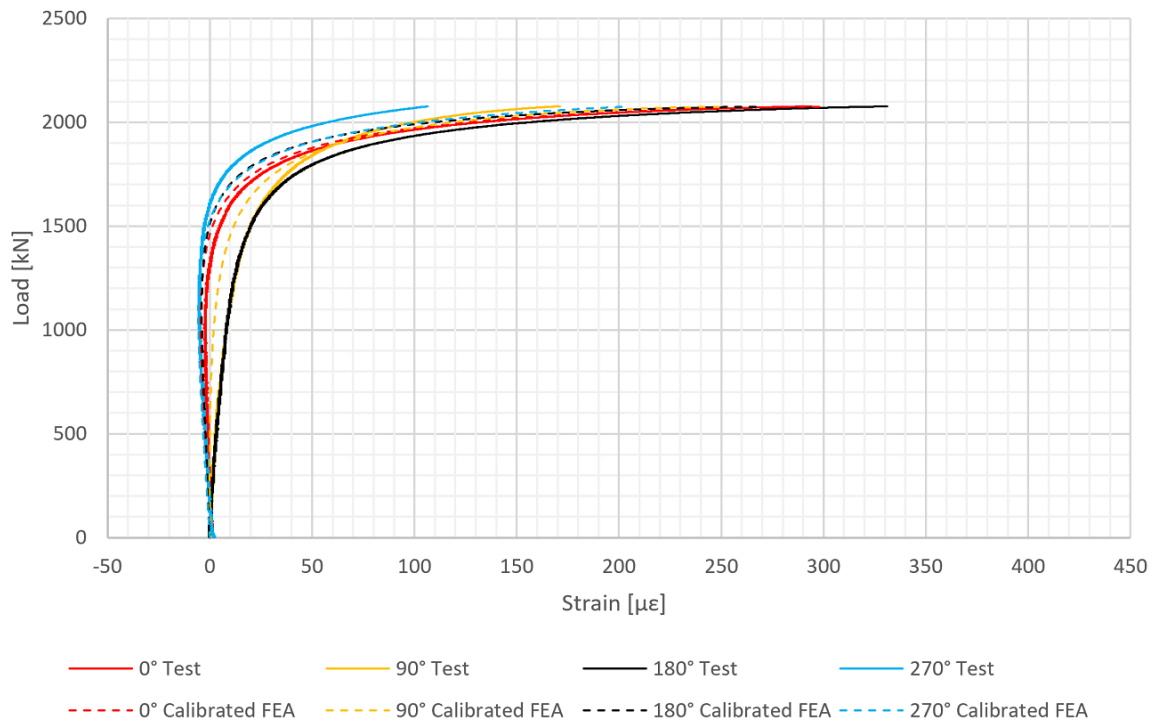


Figure 9.14: Meridian axial bending strains.

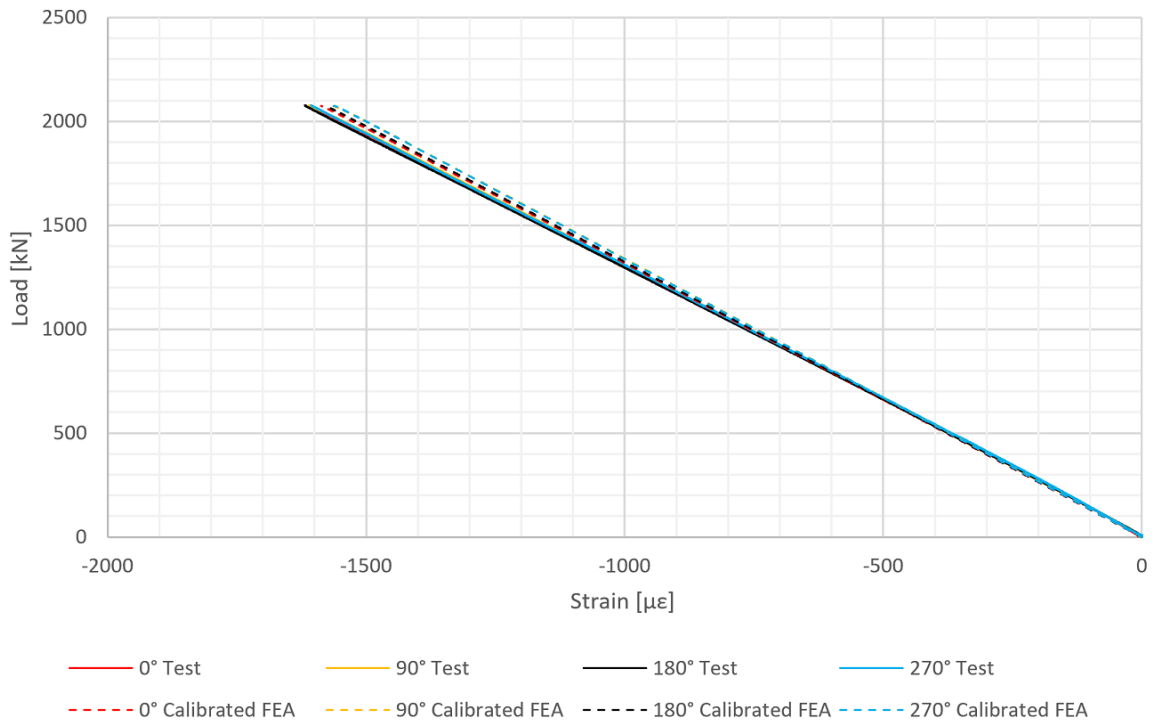


Figure 9.15: Lower axial membrane strains.

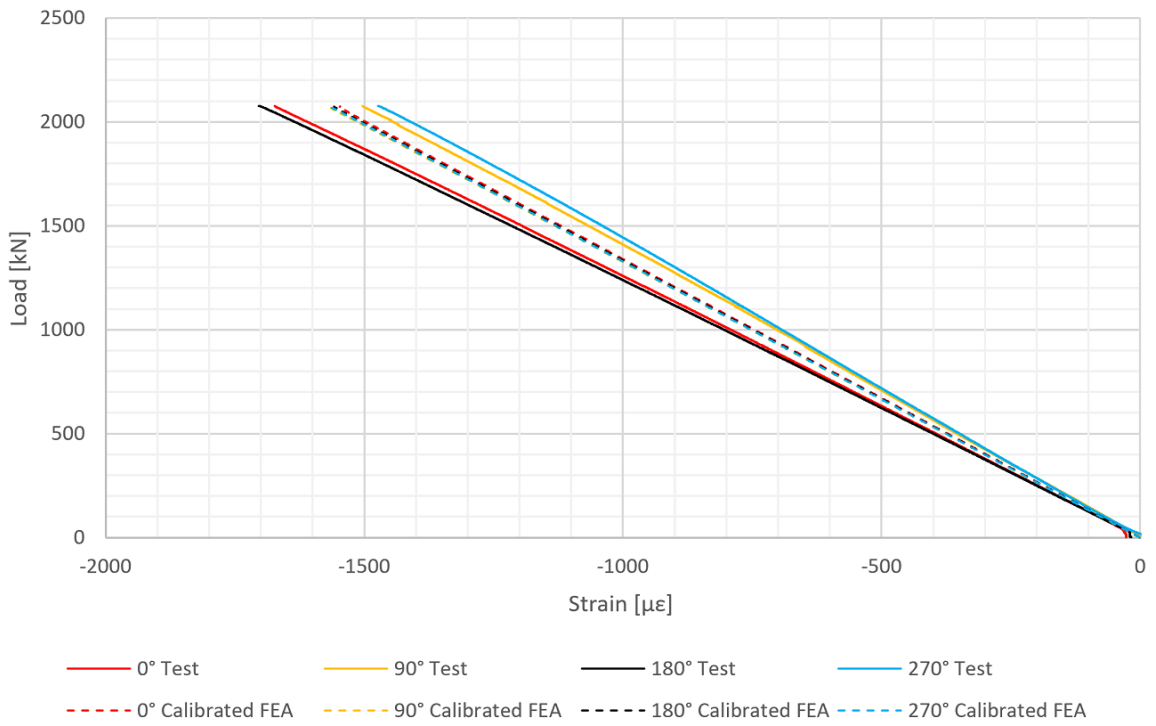


Figure 9.16: Upper axial membrane strains.

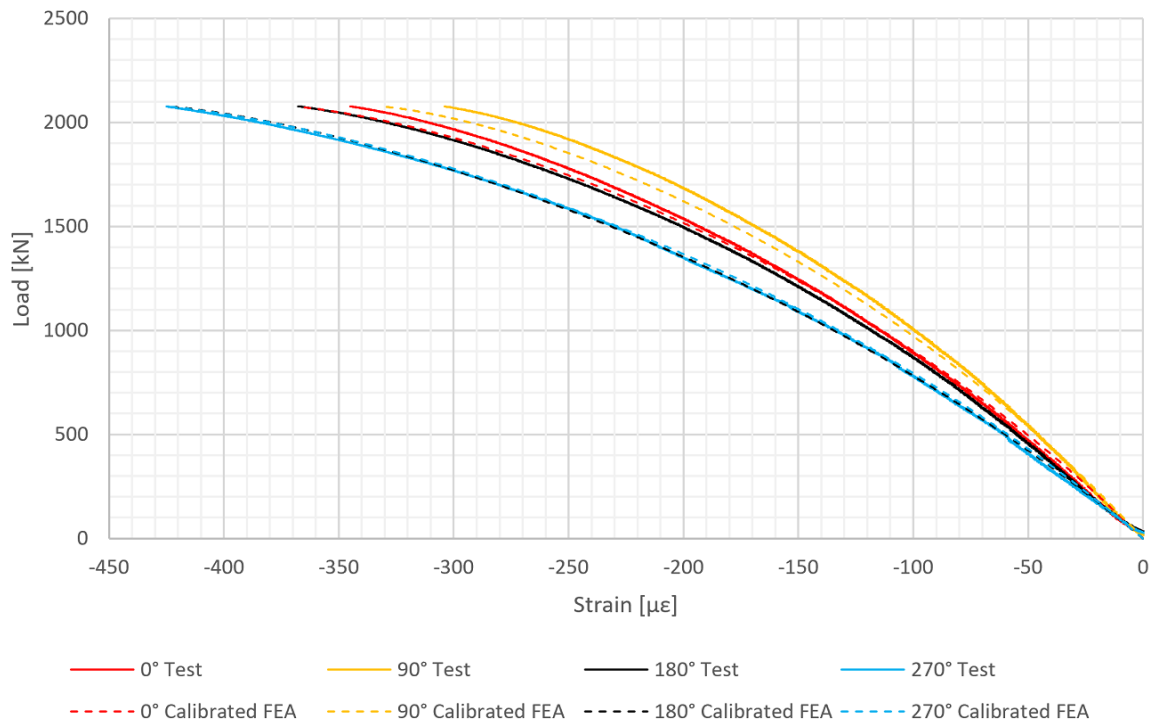


Figure 9.17: Lower axial bending strains.

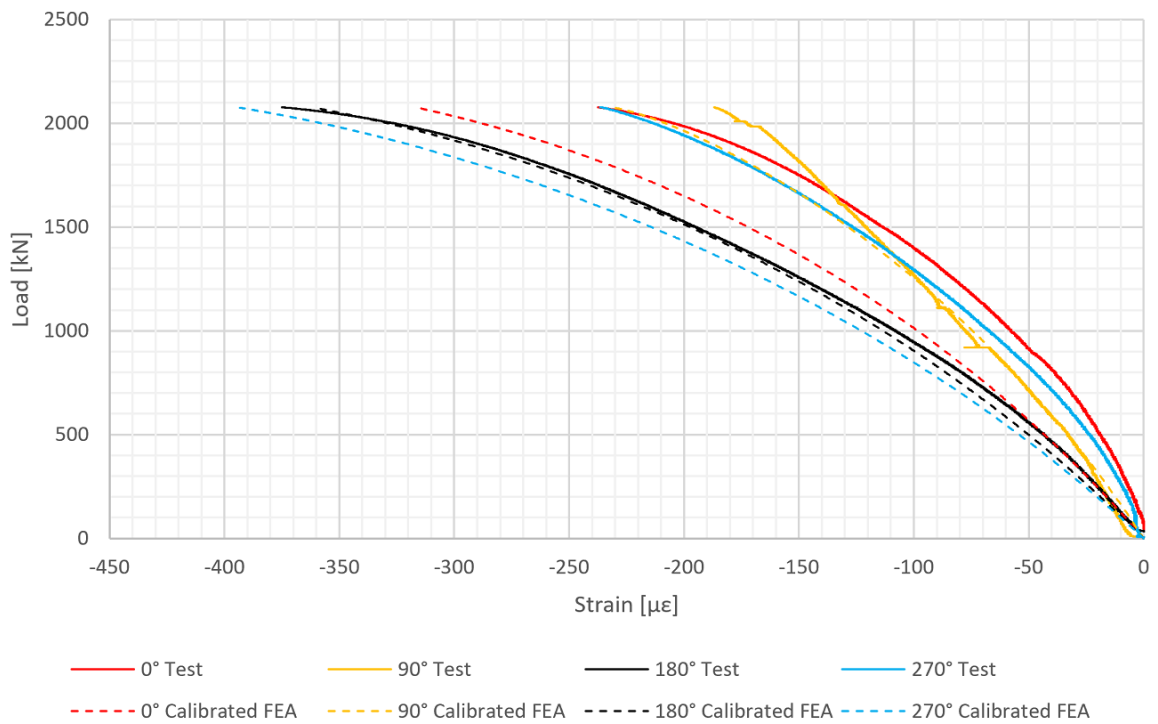


Figure 9.18: Upper axial bending strains.

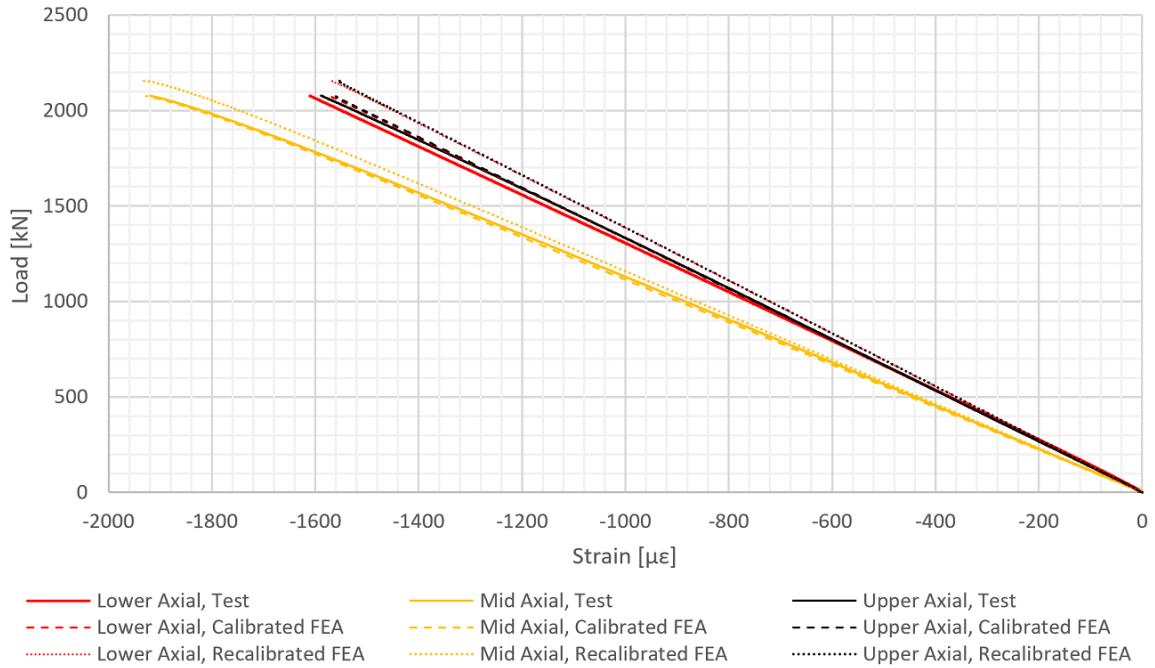


Figure 9.19: Average axial membrane strains compared between the test and both simulations.

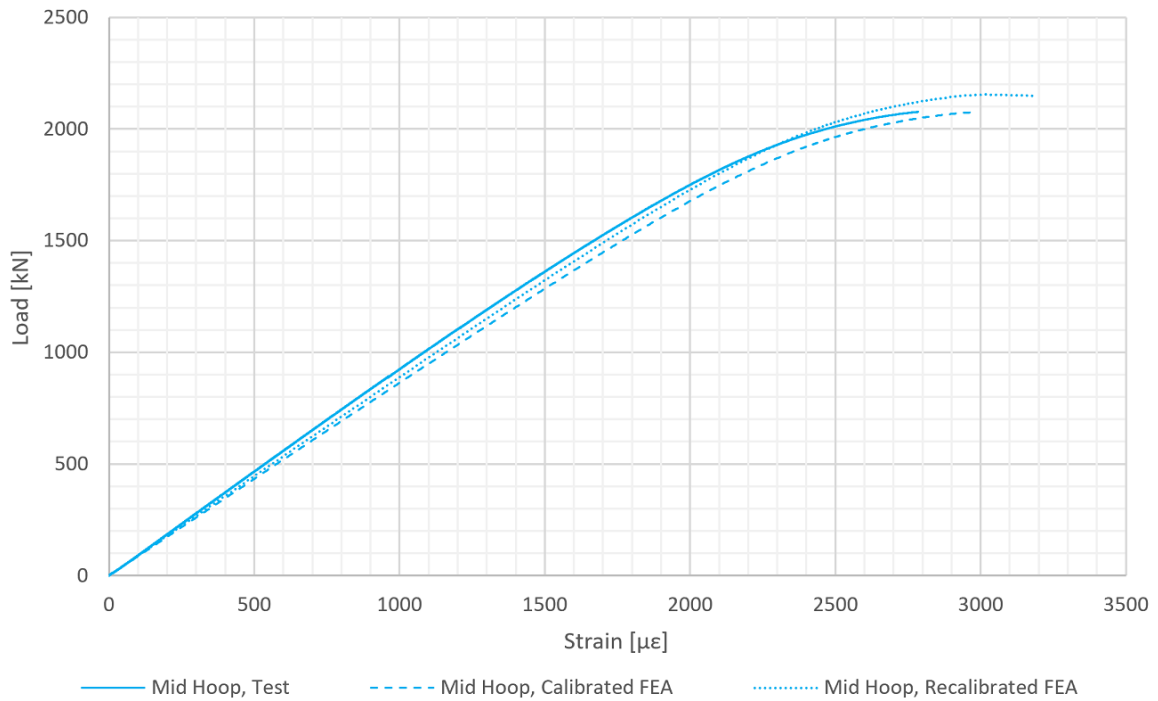
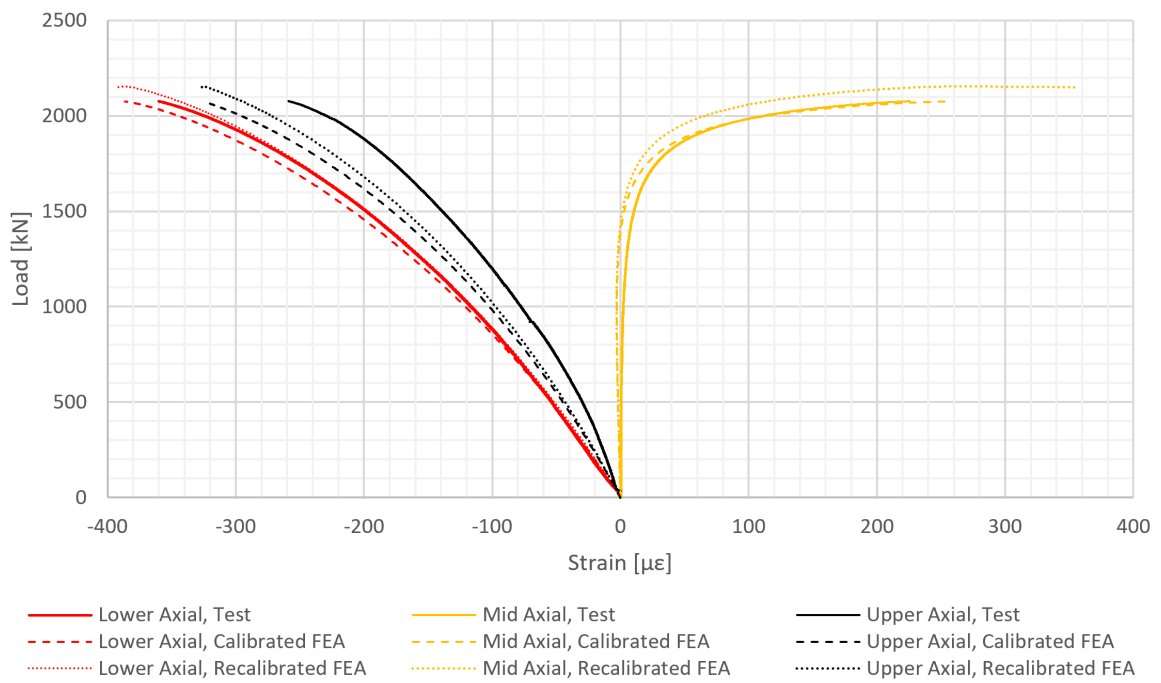


Figure 9.20: Average circumferential membrane strains compared between the test and both simulations.



**Figure 9.21:** Average axial bending strains compared between the test and both simulations.

### 9.3 Pre-buckling and Buckling Shape Evolution

NDL-1's radial displacement contours from low- and high-speed DIC are compared to those of the calibrated simulation in this section. NASA provided all DIC contours with length units in inches. Scales were removed and regenerated in SI units via MATLAB scripting. As indicated by Figure 9.4, the DIC systems were unable to achieve full circumferential coverage due to the load frame's columns. Hence blank vertical areas appear around the  $90^\circ$  and  $270^\circ$  positions of Figures 9.23a through 9.27a, 9.29a through 9.33a, and 9.34. All experimental contours featured larger radial displacement ranges than the corresponding simulation contours. Thus the color scales of each individual contour was set according to its own unique minimum and maximum radial displacement (rather than sharing a common scale). Additionally, since the DIC contours only included the non-potted shell acreage, simulation contours were produced to show the same acreage between axial positions of approximately  $-585$  mm and  $585$  mm.

#### 9.3.1 Pre-buckling

Low-speed DIC was used to capture the general shape of the test article prior to buckling. Figure 9.22 indicates the loads and axial displacements at which the radial displacement contours of Figures 9.23 through 9.27 were captured. Figures 9.23 through 9.26 represent load levels  $445$  kN (100 kilopound) apart, an interval equal to 21.4% of the buckling load. Additionally, Figure 9.27 shows the pre-buckling shape at the peak load.

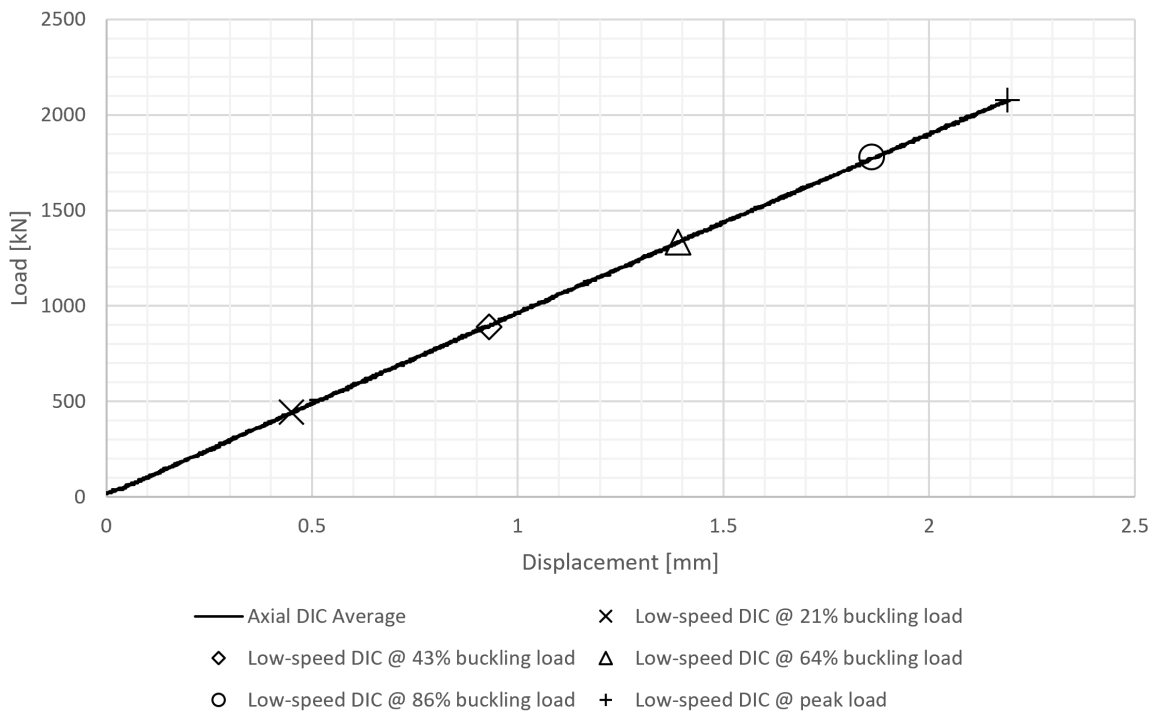


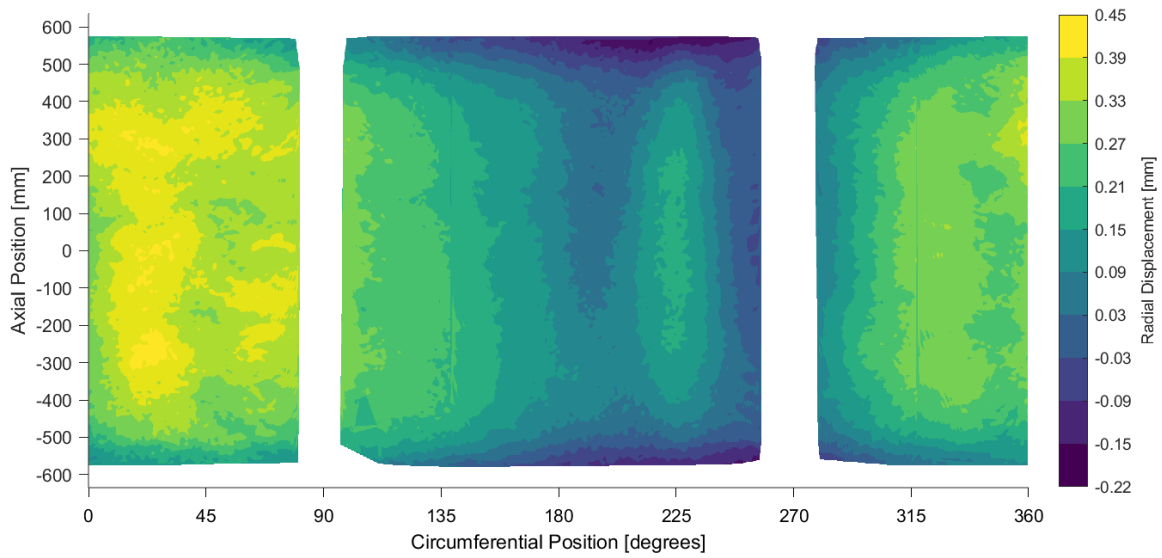
**Figure 9.22:** Points corresponding to the contours of Figures 9.23 through 9.27.

As imposed axial displacement increases, the pre-buckling figures feature progressively larger radial displacement of the shell acreage between axial positions of  $-500$  mm and  $500$  mm. Ex-

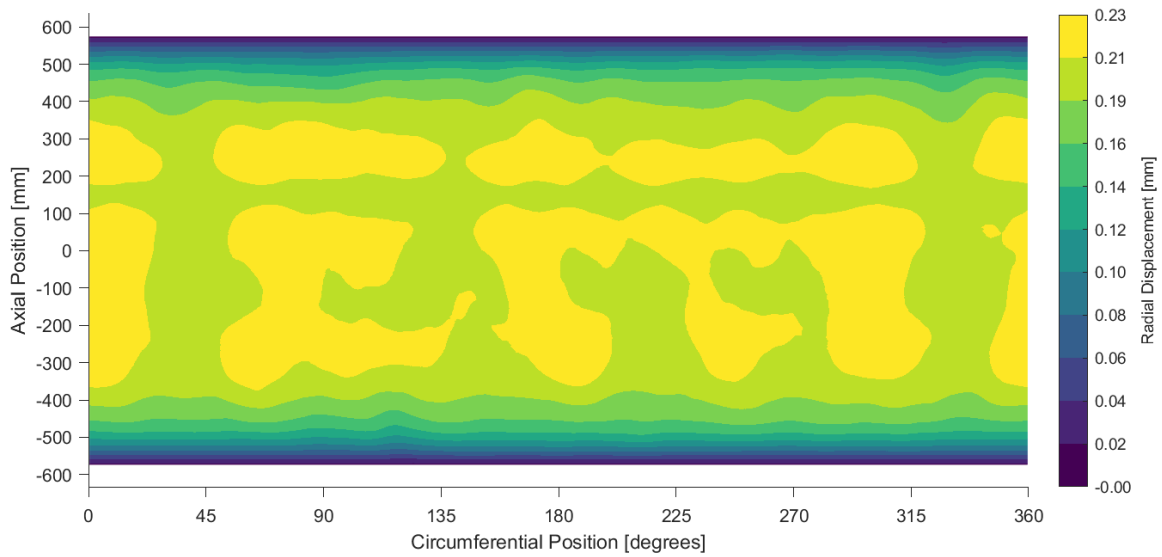
pectedly, there was less radial displacement change in acreage beyond these limits (i.e. closer to the potted regions). Circumferentially varying radial displacement from the experiment was evident early in the loading process, particularly in Figures 9.23a, 9.24a, and 9.25a; in contrast, the simulated radial displacement was much more circumferentially uniform, per Figures 9.23b, 9.24b, and 9.25b. This may be evidence of a slightly uneven load introduction in the experiment. Alternatively or additionally, the reference shape from which the DIC systems measured radial displacement may have been off-center. This is supported by the experimental radial displacements at the upper and lower edges of these figures; these edges' radial displacement around  $225^\circ$  remained fixed at about  $-0.20$  mm, whereas that of the opposite circumferential position (around  $45^\circ$ ) was  $0.20$  mm.

The nascent pre-buckling pattern is evident in Figures 9.25 and 9.26. Notable features developed in this interval: a ring shaped groove between 100 mm and 200 mm (coincident with the mandrel imperfection) and a pattern of axial half-waves and circumferential full-waves. Figure 9.27 corresponds to the moment before buckling. The experimental location that became the first buckle was the deep dimple centered at  $200^\circ$  and 150 mm. The calibrated simulation agreed with the test in predicting two other dimples around  $45^\circ$  and  $135^\circ$ ; it cannot be seen in Figure 9.27a how deep the dimple at  $90^\circ$  was. However, the simulation failed to predict the deep pre-buckling dimple at  $200^\circ$ . This may have been due to loading asymmetry, which further suggested by the circumferentially varying radial displacement. In contrast, the simulation indicated more circumferentially uniform radial displacement at this load level.

The nine axial half-waves of the experimental and simulated pre-buckling patterns, shown respectively in Figures 9.27a and 9.27b, agreed with the SP-8007 analytical solution. However, the number of circumferential full-waves in the simulation (about eight or nine depending on the axial location) and experiment (around six) differed from SP-8007's zero. This may have been due to the imperfection signature itself, which is not accounted for in the analytical solution.

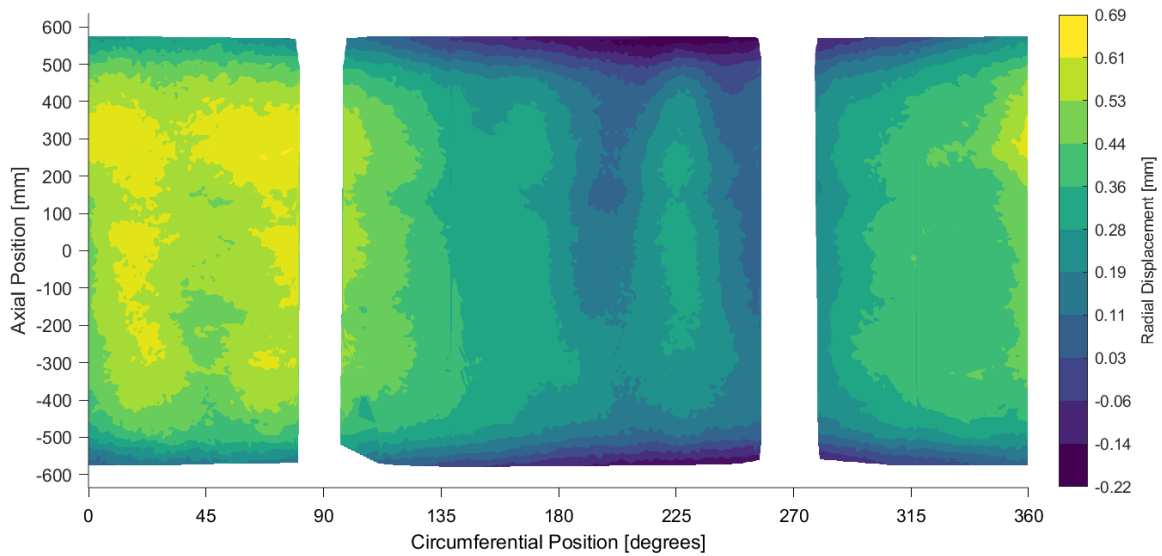


(a) Experimental. Axial displacement = 0.45 mm; Load = 445 kN.

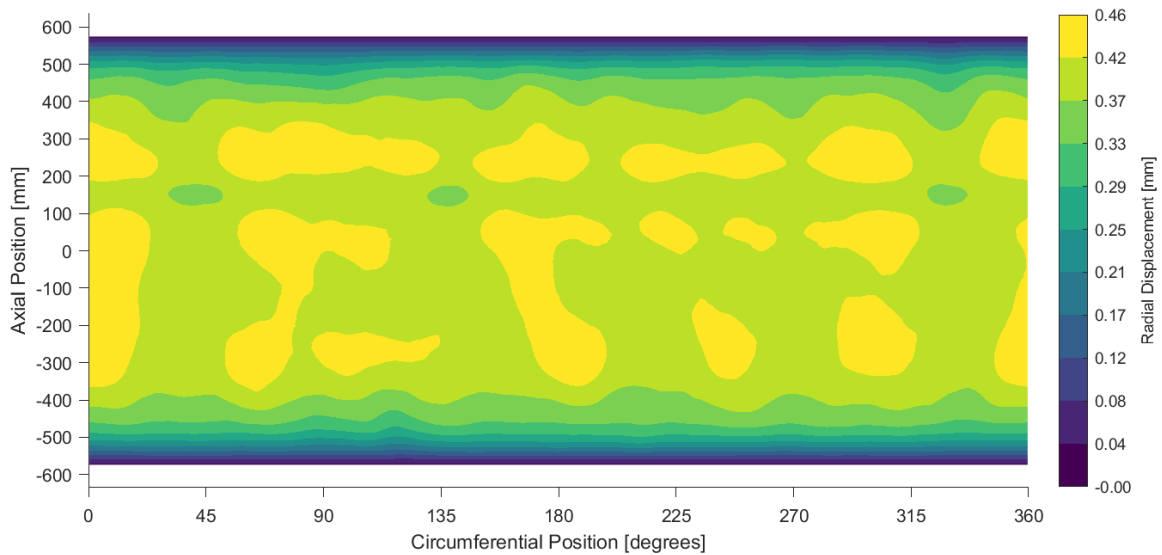


(b) Simulation. Axial displacement = 0.46 mm; Load = 444 kN.

**Figure 9.23:** Radial displacement at 21% of the buckling load.

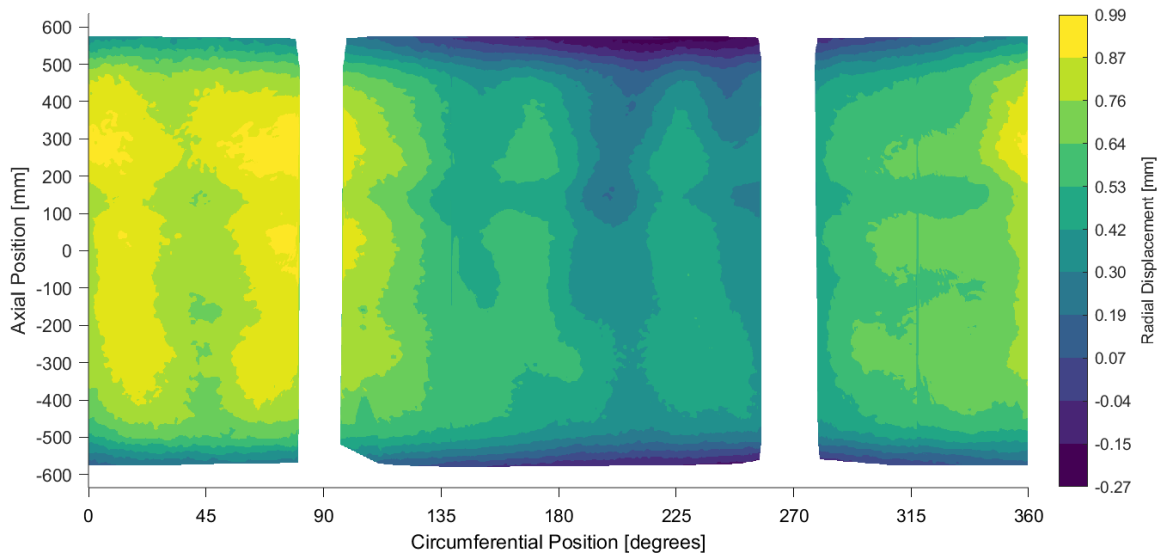


(a) Experimental. Axial displacement = 0.92 mm; Load = 890 kN.

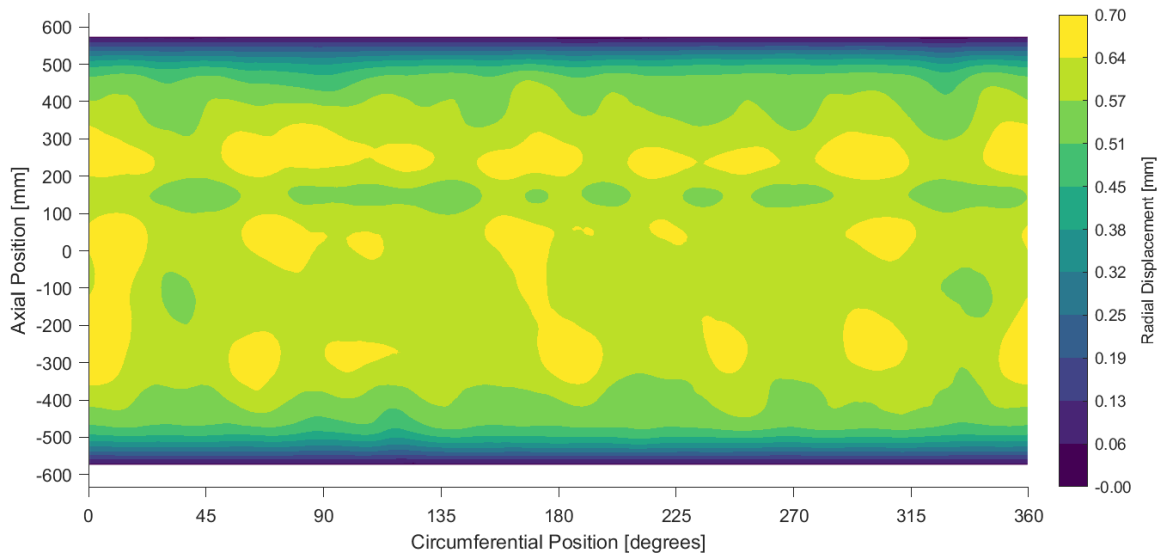


(b) Simulation. Axial displacement = 0.93 mm; Load = 889 kN.

**Figure 9.24:** Radial displacement at 43% of the buckling load.

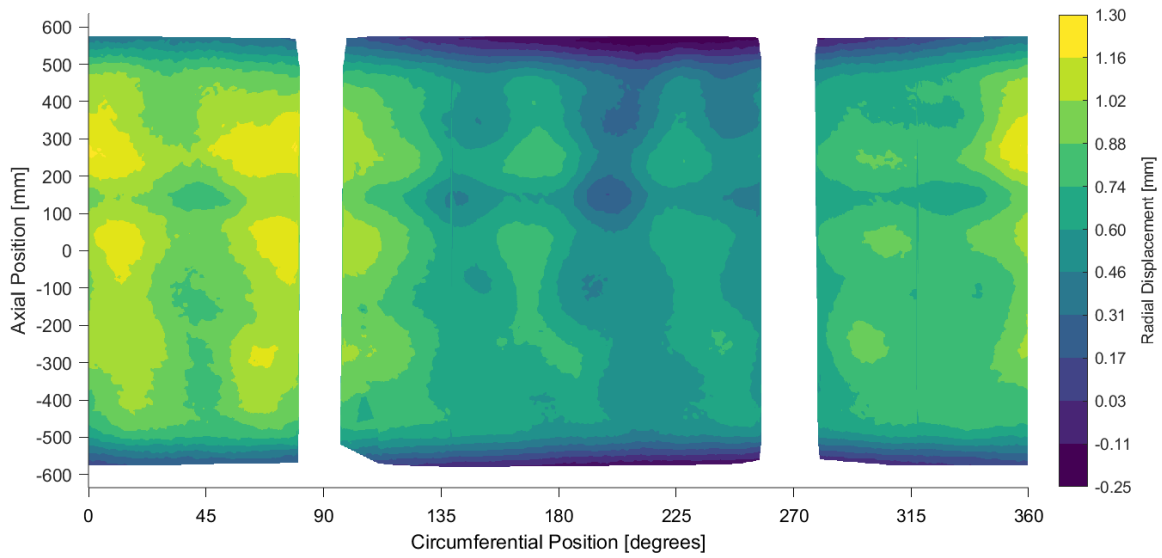


(a) Experimental. Axial displacement = 1.39 mm; Load = 1335 kN.

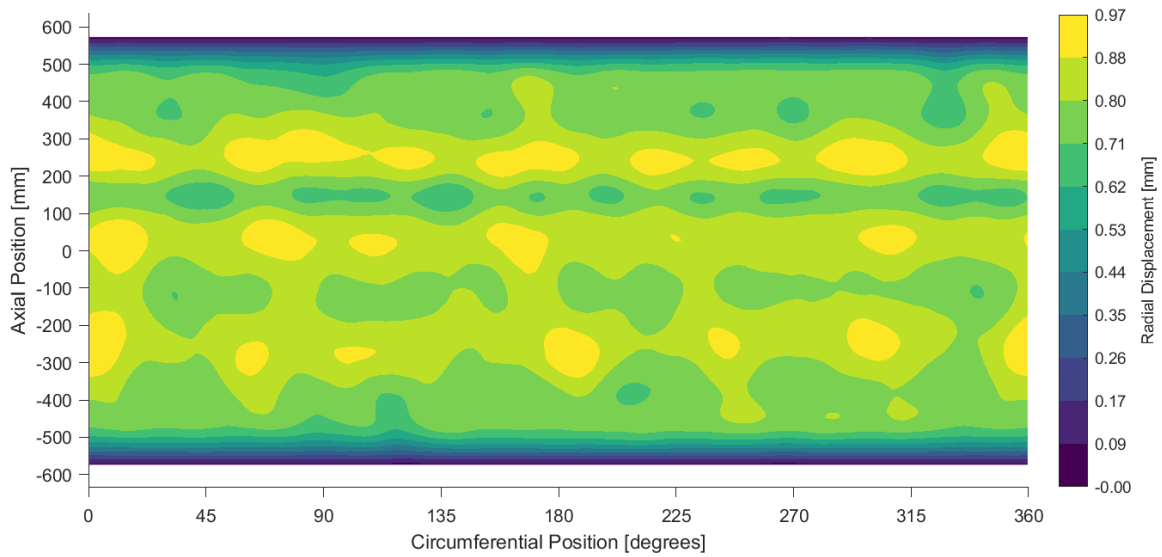


(b) Simulation. Axial displacement = 1.38 mm; Load = 1333 kN.

**Figure 9.25:** Radial displacement at 64% of the buckling load.

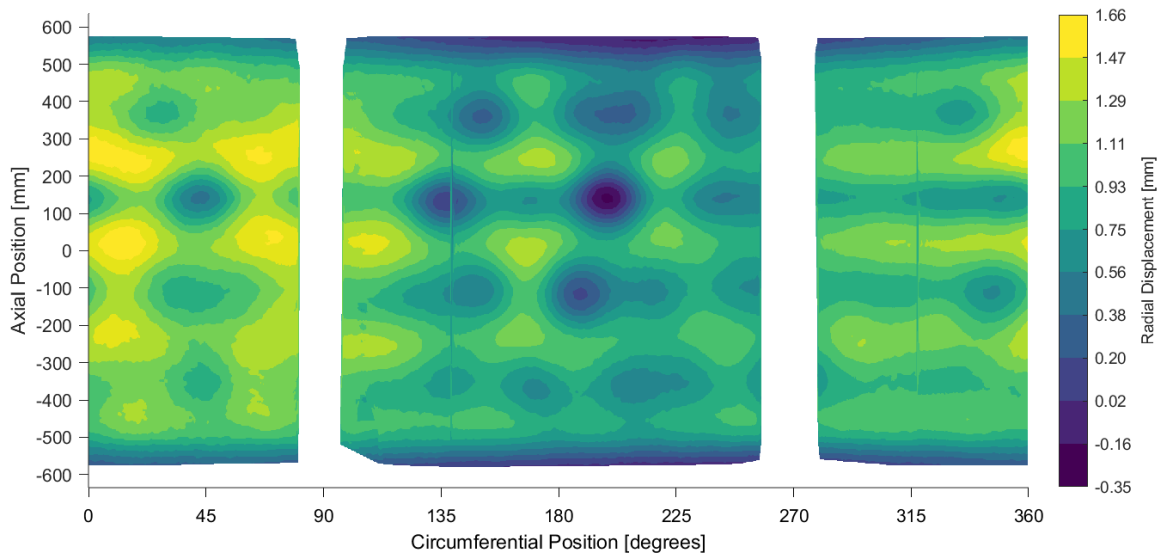


(a) Experimental. Axial displacement = 1.88 mm; Load = 1779 kN

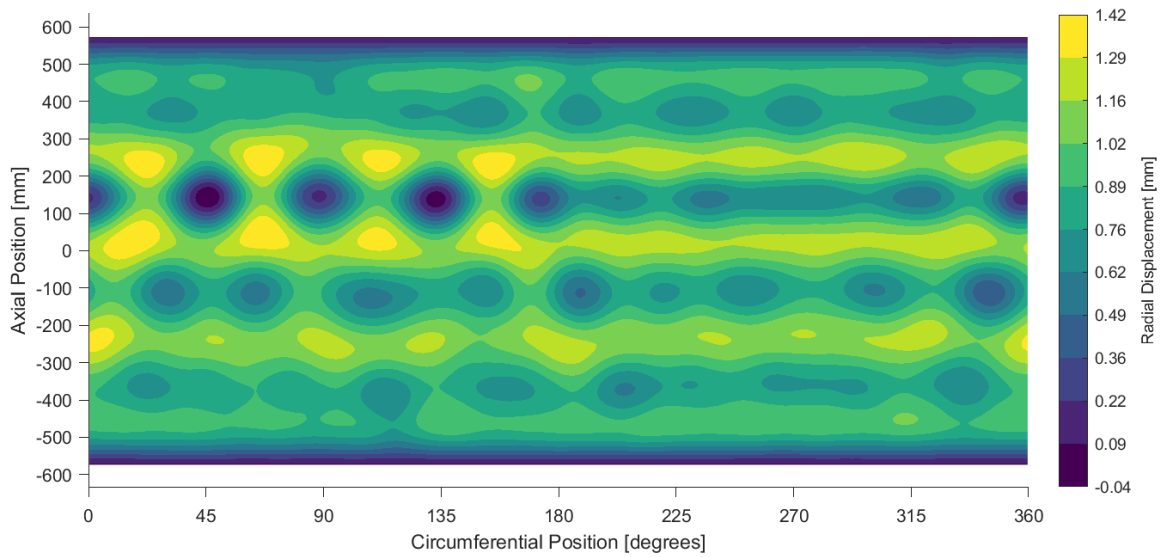


(b) Simulation. Axial displacement = 1.86 mm; Load = 1778 kN.

**Figure 9.26:** Radial displacement at 86% of the buckling load.



(a) Experimental. Axial displacement = 2.19 mm; Load = 2074 kN.



(b) Simulation. Axial displacement = 2.18 mm; Load = 2075 kN.

Figure 9.27: Radial displacement immediately prior to buckling.

### 9.3.2 Buckling Event

The buckling evolution of the calibrated simulation and the experiment are compared in Figures 9.29 through 9.33. The experimental contours of Figures 9.29a through 9.33a were obtained via high-speed DIC. No information was available regarding exact times, loads, or axial displacements at which these high-speed DIC frames were taken. Consequently, these moments could not be precisely identified on the load-displacement plot. However, they were compared with qualitatively similar simulation contour data to investigate the buckling propagation. Figure 9.28 indicates the loads and displacements corresponding to the simulated buckling contours in Figures 9.29b through 9.33b. Additionally, Figure 9.34 shows the buckling pattern as captured via low-speed DIC; this was the only low-speed DIC frame provided that showed the buckled shape.

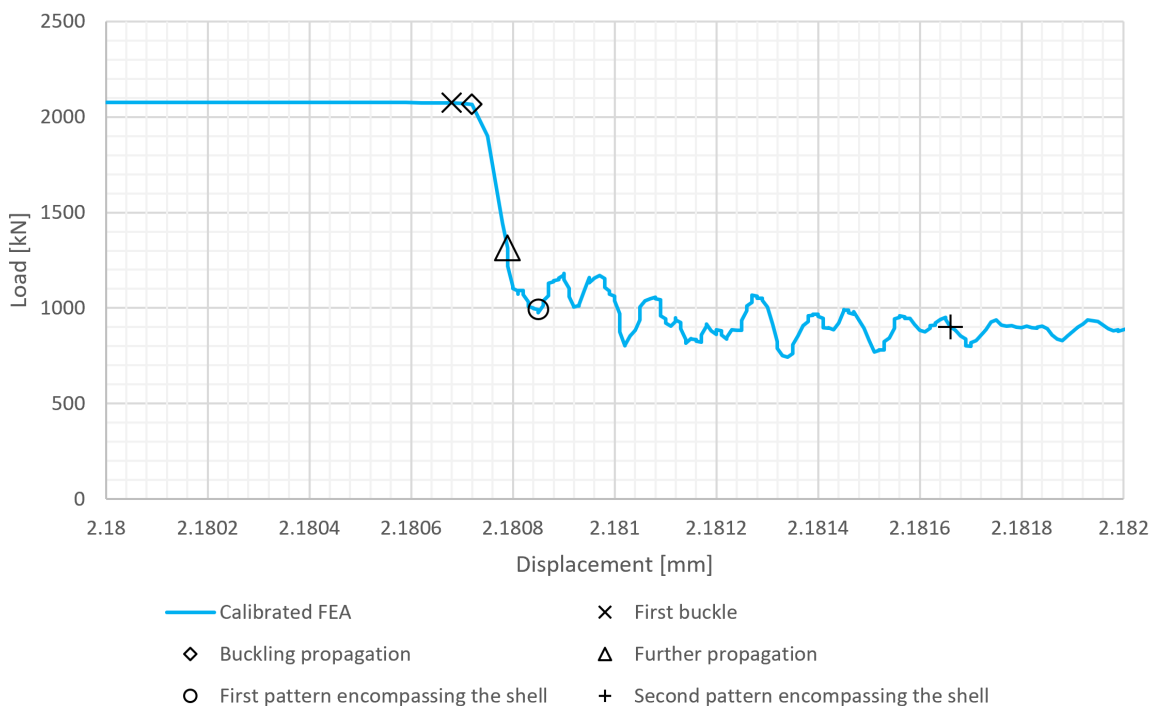


**Figure 9.28:** Points corresponding to the simulated buckling contours of Figures 9.29b through 9.33b.

The first provided high-speed DIC frame is shown in Figure 9.29a. This was used as a reference for elapsed times noted in the captions of Figures 9.30a through 9.33a. The times of experimental buckling propagation were calculated by dividing the number of frames elapsed from this reference frame by the known frame rate of 20,000 frames per second. The contour of Figure 9.29b was similarly used as the timing reference for simulated buckling propagation; the elapsed times in the captions of Figures 9.30b through 9.33b were taken from the simulation data.

Figure 9.29 shows the first experimental and simulated buckles. The experiment featured a distinct first dimple, whereas the simulation predicted a series of simultaneous initial dimples. Both the simulation and the experiment were in agreement regarding the axial position of the initial buckle(s), which was centered on the mandrel imperfection between 100 mm and 200

mm in Figure 8.7. However, the experimental buckle of Figure 9.29a occurred at  $200^\circ$  rather than  $45^\circ$  or  $135^\circ$  as predicted by the simulation per Figure 9.29b. This could be explained by the boundary shimming analysis of Wagner et al. [63], who found initial buckling occurred at the circumferential position of a shim. Thus the aforementioned potential boundary tilt centered at  $151^\circ$  may have biased the first experimental dimple to occur near it. The physical shims described in Table 9.1 may have also played a role in influencing the initial buckling location relative to the simulation, as they were not taken into account in the analysis.

This first experimental dimple then began to propagate into a pattern throughout the structure as indicated in Figure 9.30a. The range of radial displacement range (-25 mm to 8.6 mm) increased drastically during this transition. This was more than twice the magnitude of the simulated radial displacement in Figure 9.30b (-8.4 mm to 4.3 mm), which represents a similar stage in the pattern's propagation around the shell's circumference.

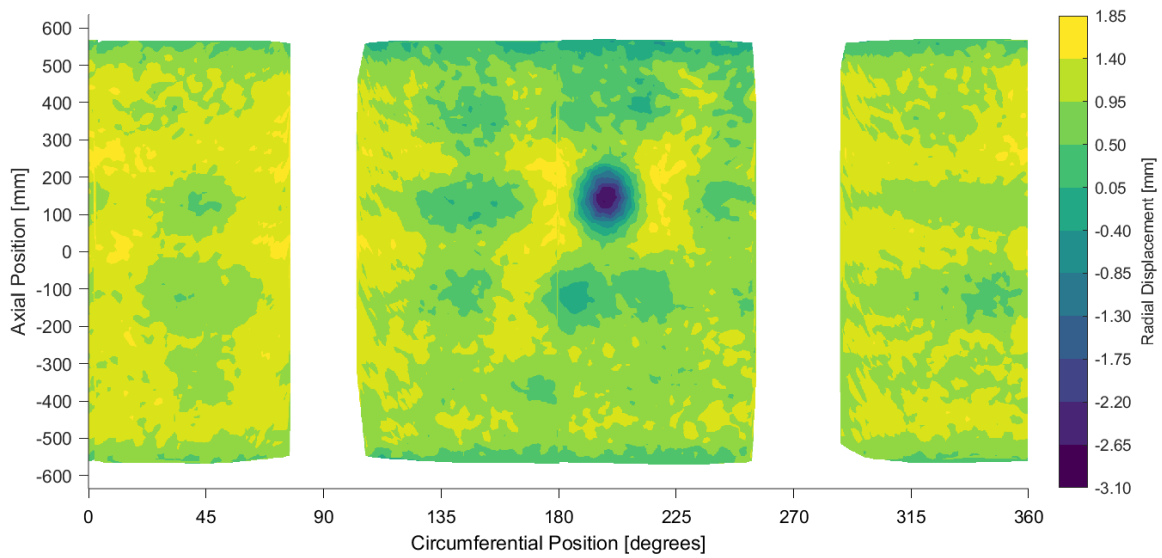
Figure 9.31 shows the buckling patterns as they approached the circumferential position opposite the initial buckling location. The radial displacement range continued to grow. The fully propagated buckling patterns are shown in Figure 9.32, with further expanding radial displacement. The experimental radial displacement range (-29 mm to 16 mm) was nearly double that of the simulation (-17 mm to 6.9 mm). Moreover, the simulation and experiment differed with regard to the first fully propagated buckling pattern. Both were in agreement with two axial half-waves, but NDL-1 exhibited seven circumferential full-waves, while the simulation predicted eight. This may have been why the experimental buckles were larger than the simulated buckles. It took 7.3 milliseconds from the first provided high-speed DIC frame of Figure 9.29a to propagate into the first full buckling pattern shown in Figure 9.32a. The simulation propagation time was of a similar magnitude: 5.1 milliseconds. This slight difference may have been caused by several factors: temporal alignment mismatch between the reference frames of Figures 9.29a and 9.29b; different experimental and simulated displacement rates; implicit analysis default damping parameters that were not tuned to any experimental values; or the explosiveness of the buckling event that resulted in interaction with the load frame.

After the first buckling shapes encompassed the shell, the experimental and simulated buckling patterns further evolved in a similar manner. For both, Figure 9.33 shows a reduction of one circumferential full-wave relative to the patterns of Figure 9.32, which led to six circumferential full-waves in the experiment and seven in the simulation. Figure 9.33a was the last available high-speed DIC frame.

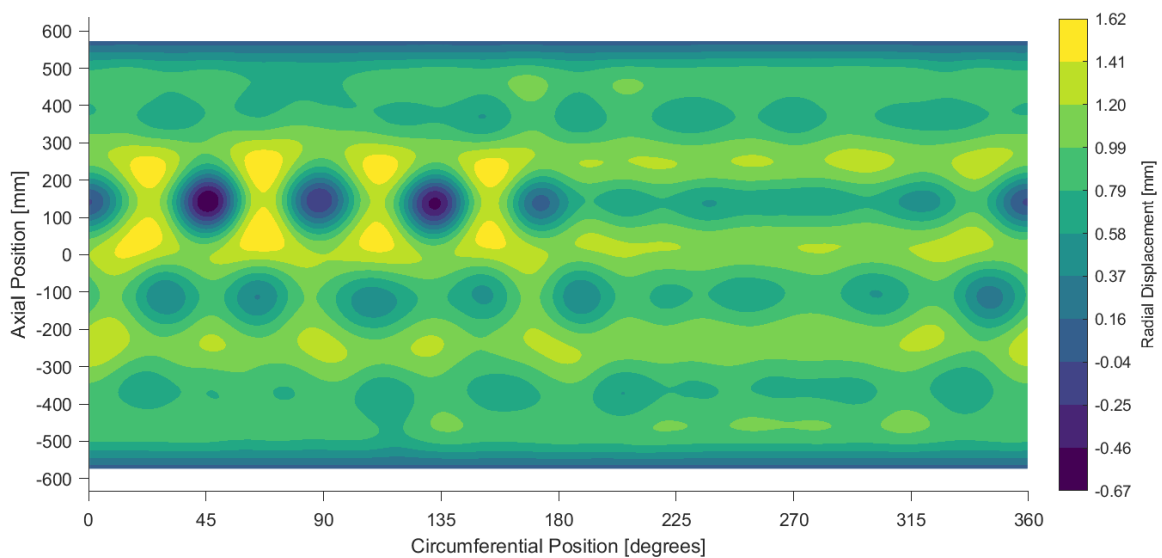
In addition to loading asymmetry, material failure of the test article during the buckling event may have caused a different evolution pattern from the simulation. While failure criteria were output from the simulation to understand when and where failure might occur, material failure and damage propagation themselves were not modeled. Such details could have had an effect on the minimum strain energy state of the structure and thus may have influenced the stability characteristics like the buckling shape and amount of radial displacement.

Figure 9.34 was the only low-speed DIC frame that showed the buckled shape of the shell. Data provided by NASA indicated this frame corresponded to a load of 663 kN and an axial displacement of 4.49 mm (as derived from DIC). The latter is more than double the immediate pre-buckling axial displacement of 2.19 mm; it was not known at the time of writing if this measurement was valid or not. This contour displays the same buckled pattern of six circumferential full-waves and two axial half-waves as Figure 9.33a, albeit with substantially

less radial displacement, ranging from -31 mm to 16 mm. Additionally, Figure 9.34 shows more uniform radial displacement between each of the outwardly displaced ridges and between each of the inwardly displaced dimples than those of Figure 9.33a, potentially indicating the end of the evolution and thus equilibrium. Further, this suggests all high-speed DIC frames were captured prior to this frame, as the load was decreasing from 2077 kN to 663 kN.

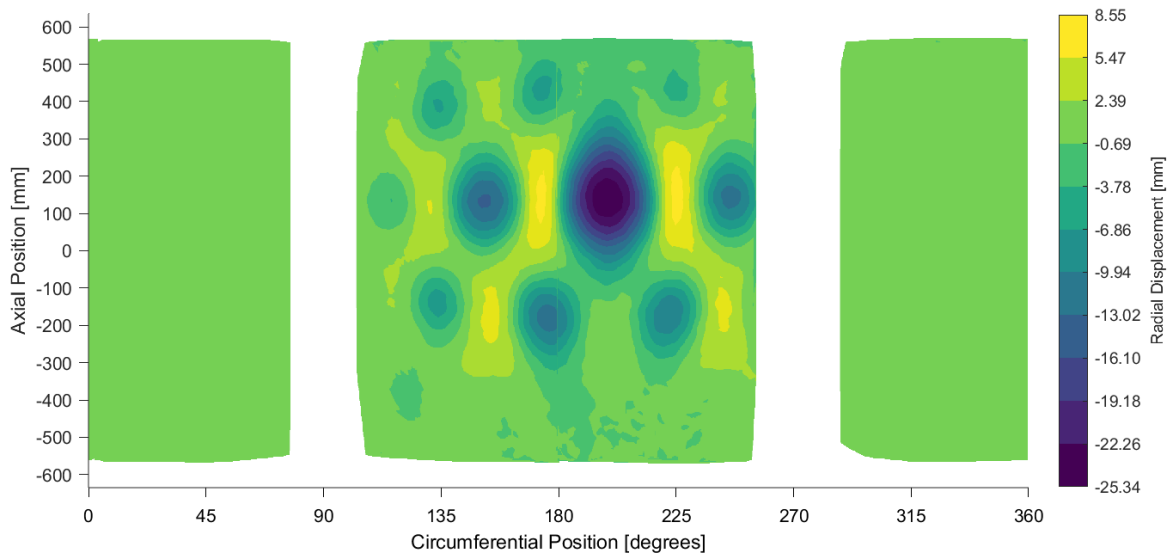


(a) Experimental

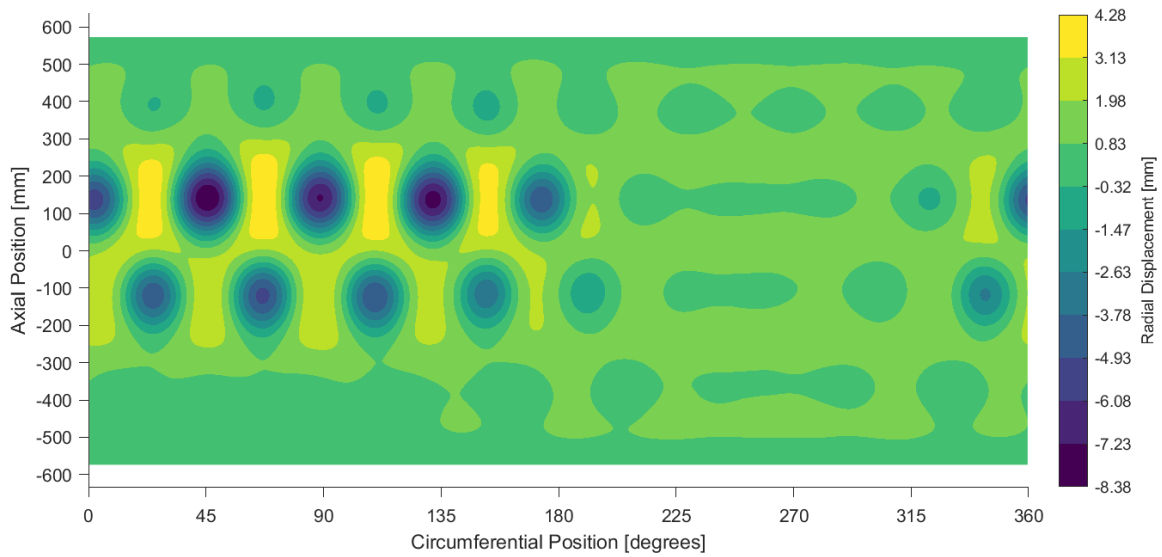


(b) Simulation

Figure 9.29: Initial dimples.

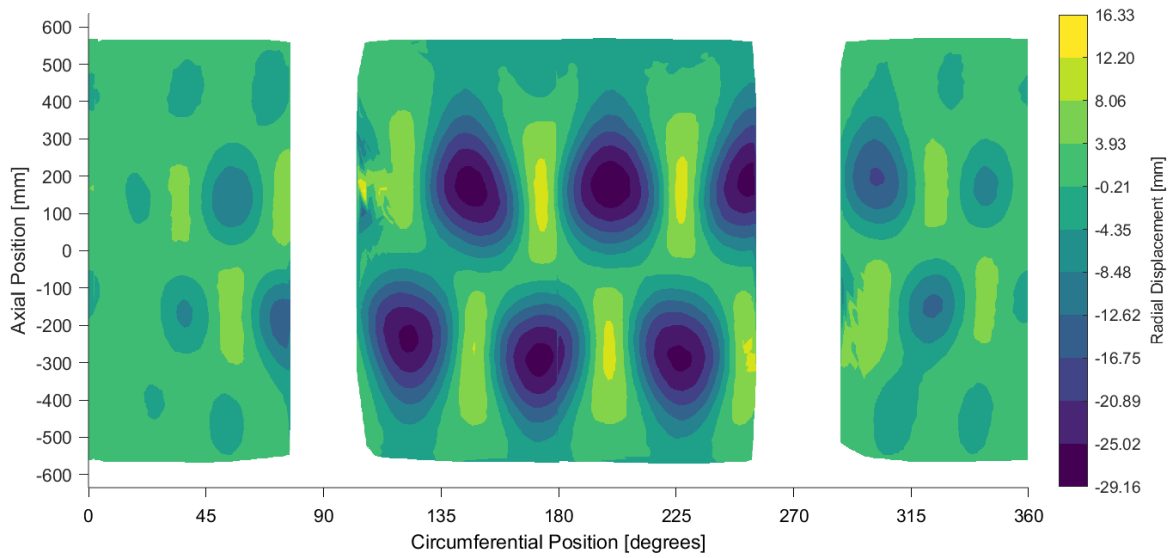


(a) Experimental (2.5 milliseconds after Figure 9.29a)

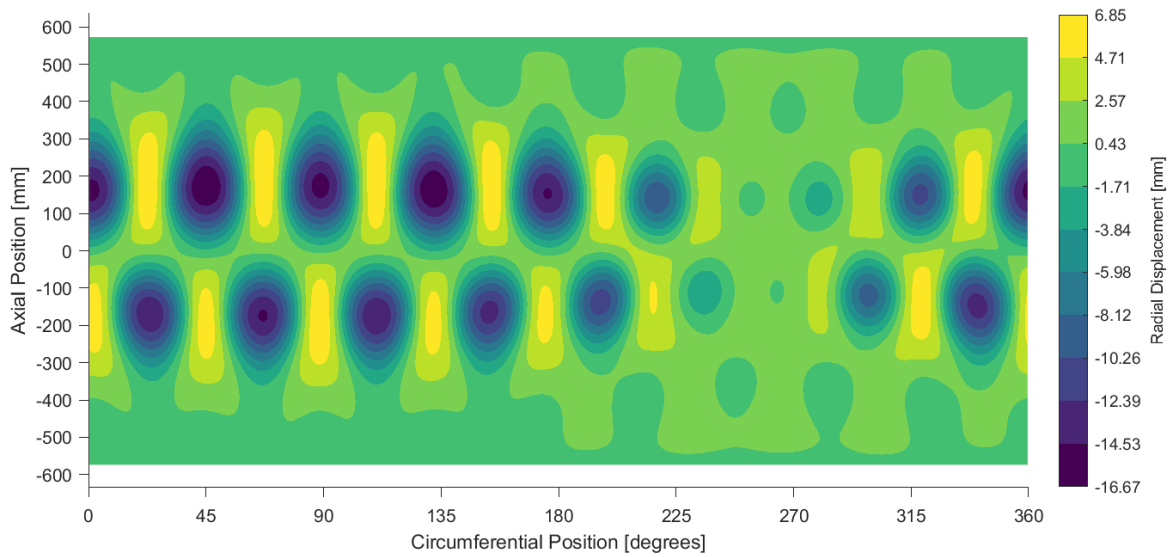


(b) Simulation (1.2 milliseconds after Figure 9.29b)

Figure 9.30: Buckling propagation.

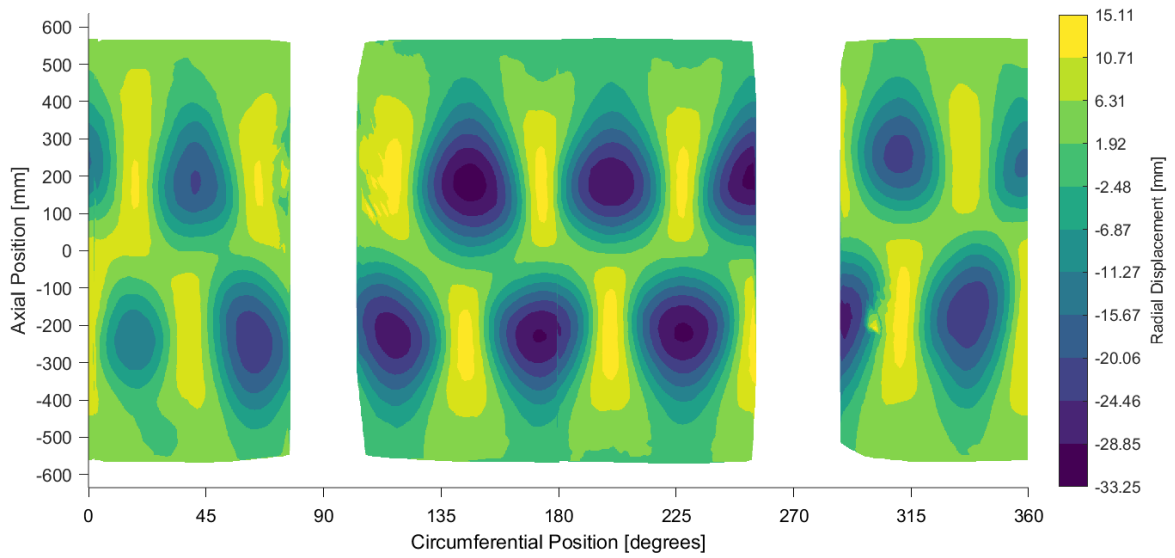


(a) Experimental (5.1 milliseconds after Figure 9.29a)

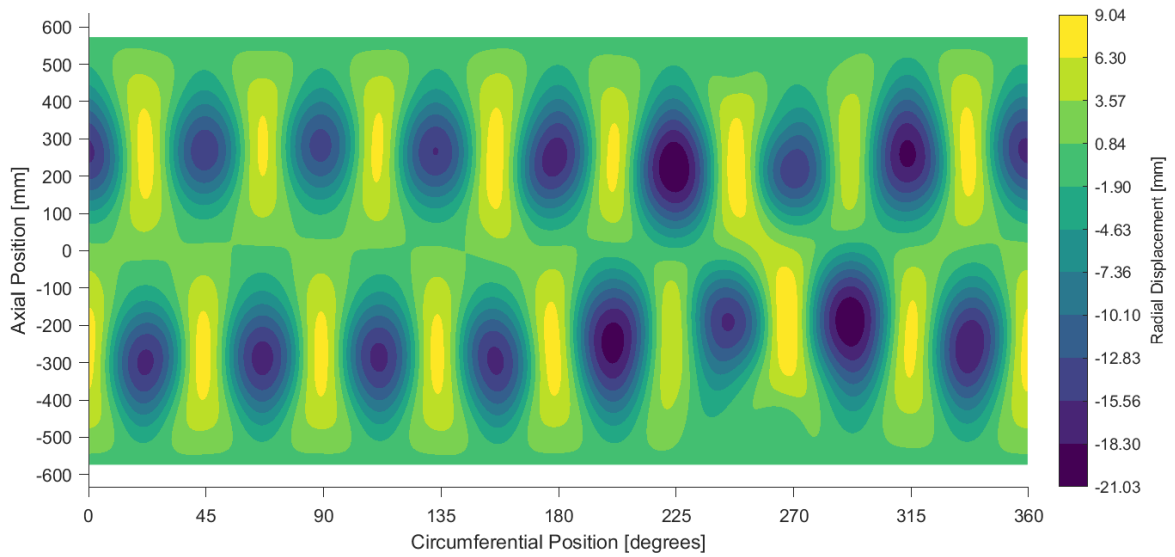


(b) Simulation (3.3 milliseconds after Figure 9.29b)

**Figure 9.31:** Further buckling propagation.

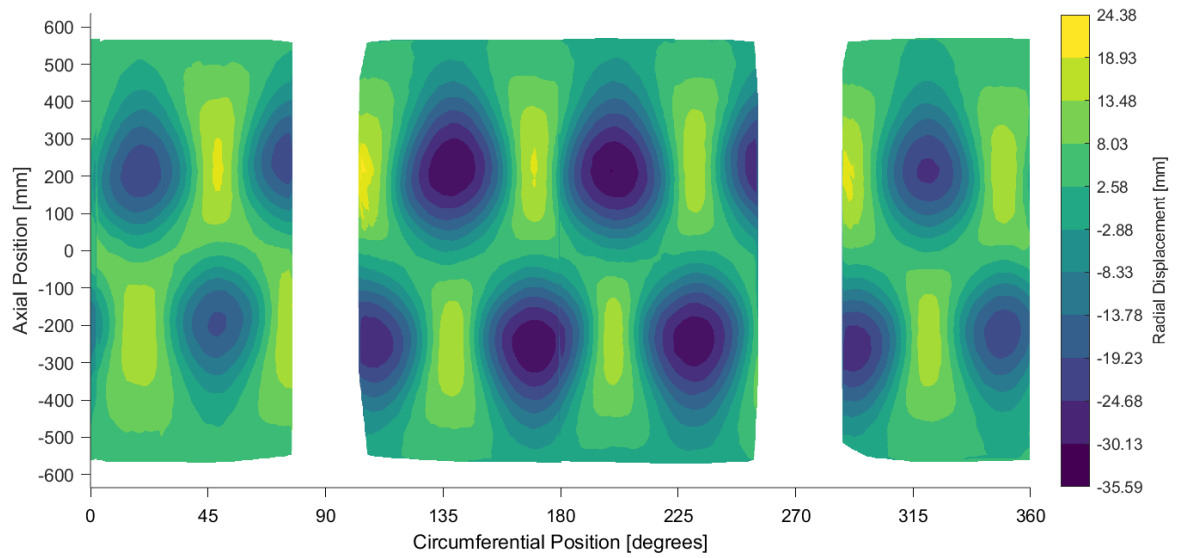


(a) Experimental (7.3 milliseconds after Figure 9.29a)

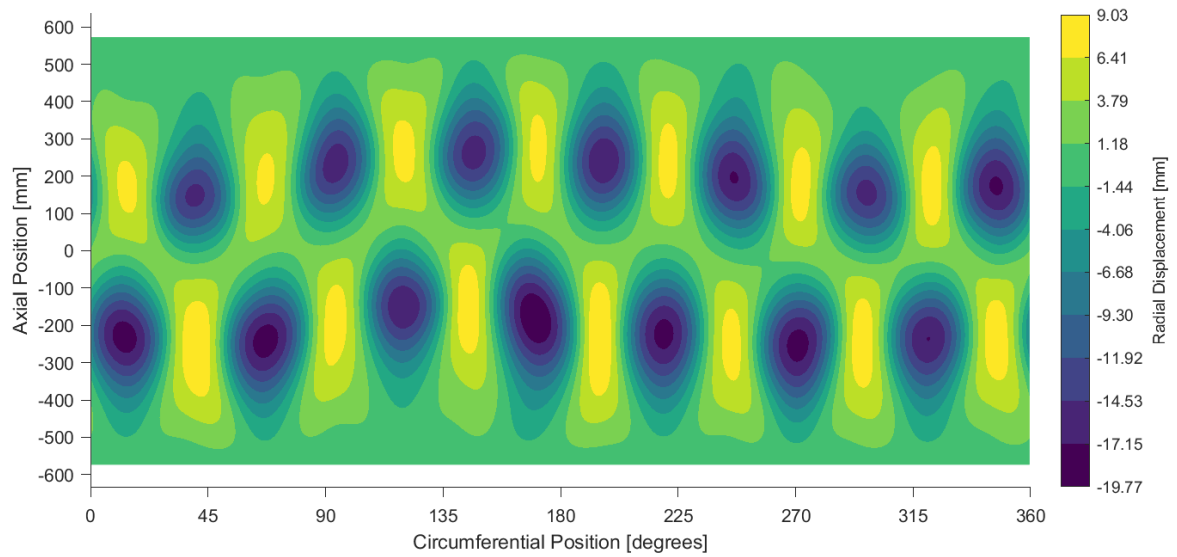


(b) Simulation (5.1 milliseconds after Figure 9.29b)

**Figure 9.32:** Buckling propagation to the entire circumference.



(a) Experimental (16.3 milliseconds after Figure 9.29a)



(b) Simulation (29.4 milliseconds after Figure 9.29b)

**Figure 9.33:** Further buckling evolution: one circumferential full-wave less than Figure 9.32.

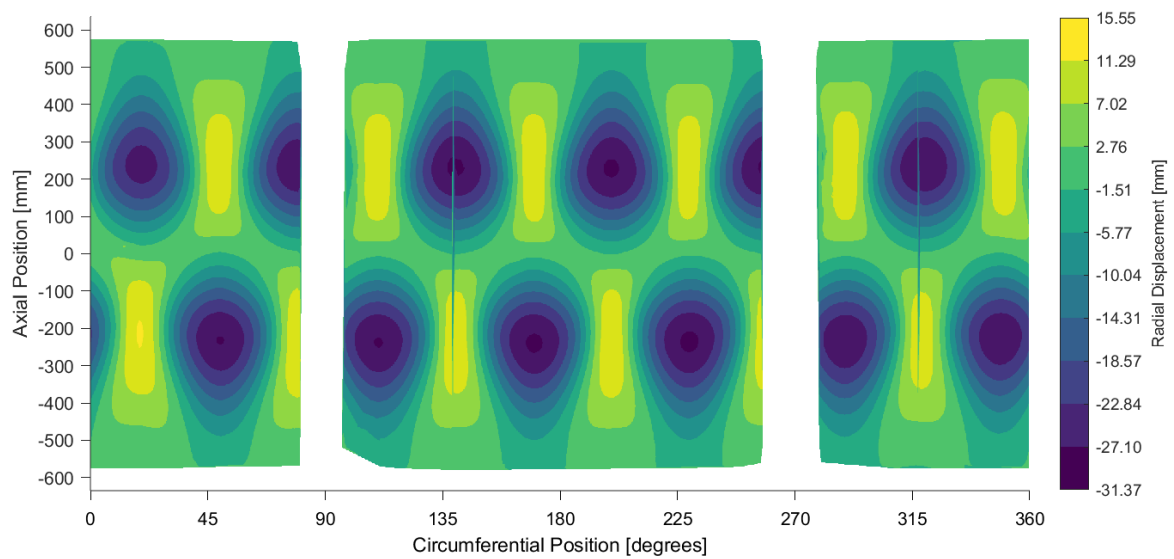


**Figure 9.34:** Low-speed DIC capture of the buckling event. The associated load was 663 kN.

## 9.4 Additional Observations

A delamination was found after the buckling test at an axial location of about 0 mm and a circumferential location of  $170^\circ$ , as indicated on NDL-1 in Figure 9.35. It was believed to have occurred as a result of the buckling event. This idea was also supported by the radial displacement shown in Figure 9.36 after unloading, which reveals an elevated area in the contour data, along with the outwardly radial displaced area in Figure 9.27a. This elevated area – indicated by the red ellipse in Figure 9.36 – was approximately the same size as the hand-circled area of Figure 9.35. While the simulation predicted failure along an outwardly displaced ridge in between dimples (see Figures 8.15 through 8.13), failure happened at a lower axial position than expected.

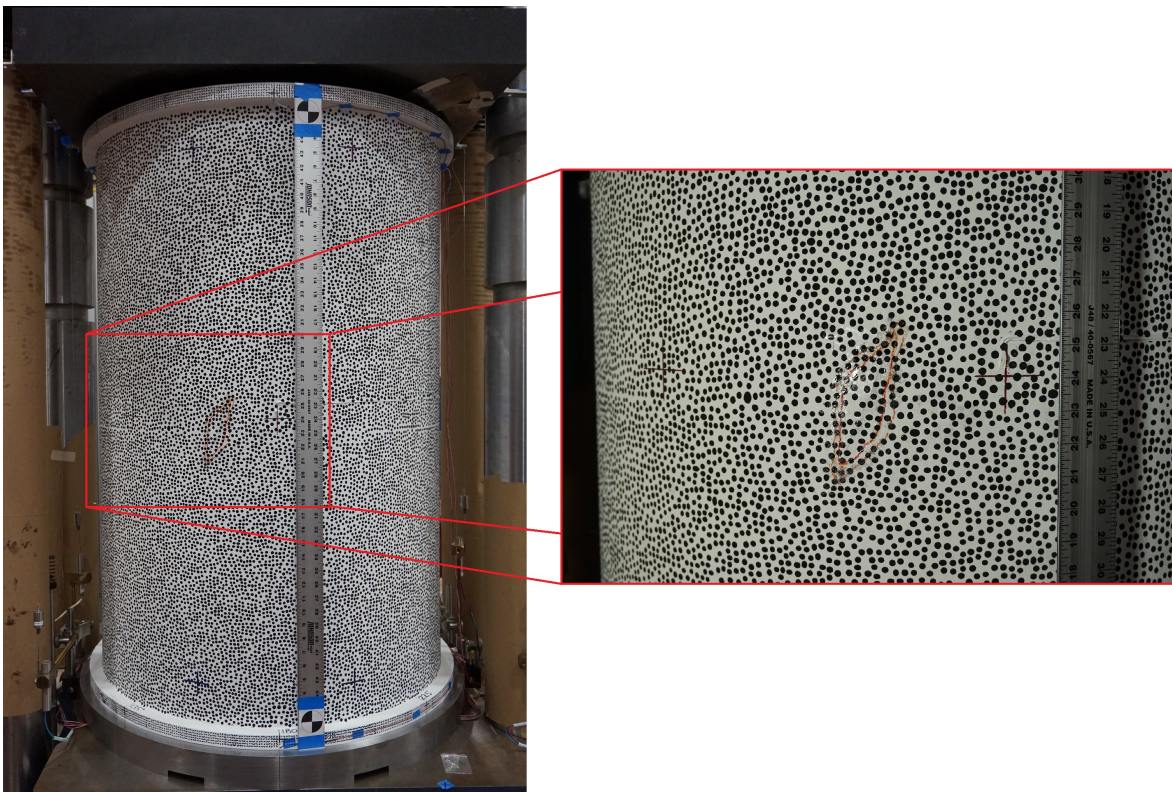


**Figure 9.35:** The delamination location is outlined in red (photo courtesy of NASA).

The delamination was further investigated in comparison to the interpolated mid-surface and thickness, as shown in Figures 9.37 and 9.38, respectively. It appeared that this delamination occurred near, and potentially coincidentally, with a light blue area, which was believed to be a tow-splice inherent to the manufacturing process.

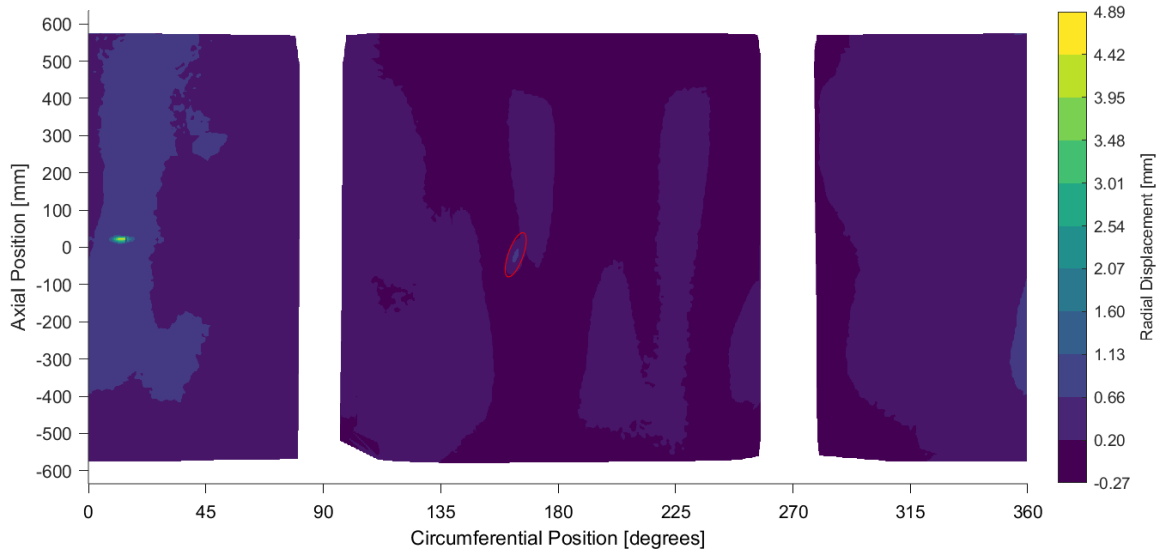


**Figure 9.36:** The delamination area (red ellipse) overlaid with a low-speed DIC contour taken after unloading NDL-1.

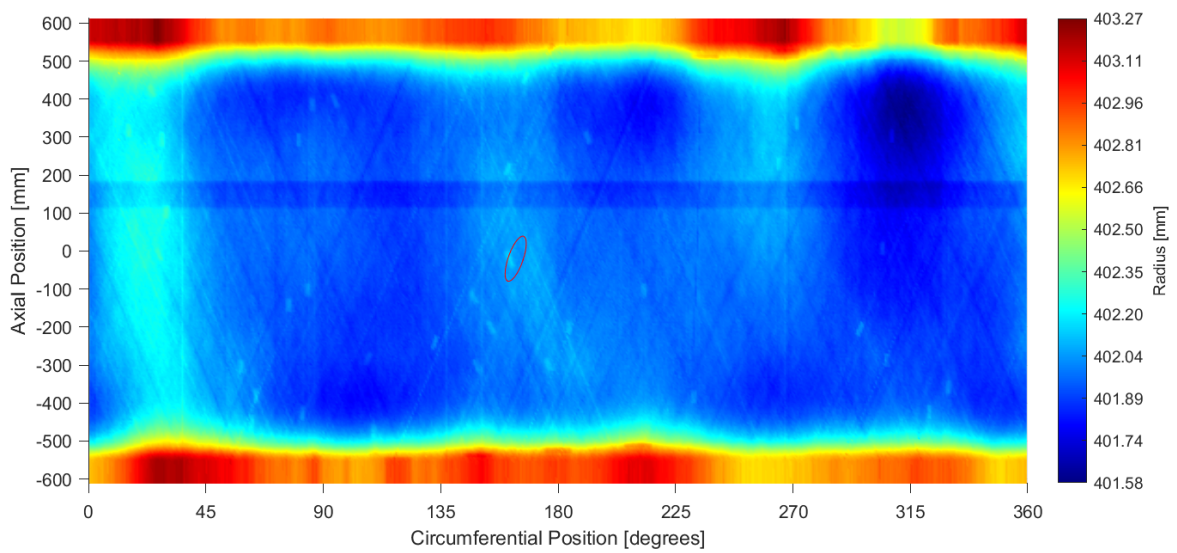


**Figure 9.37:** The delamination area (red ellipse) overlaid with the interpolated mid-surface.

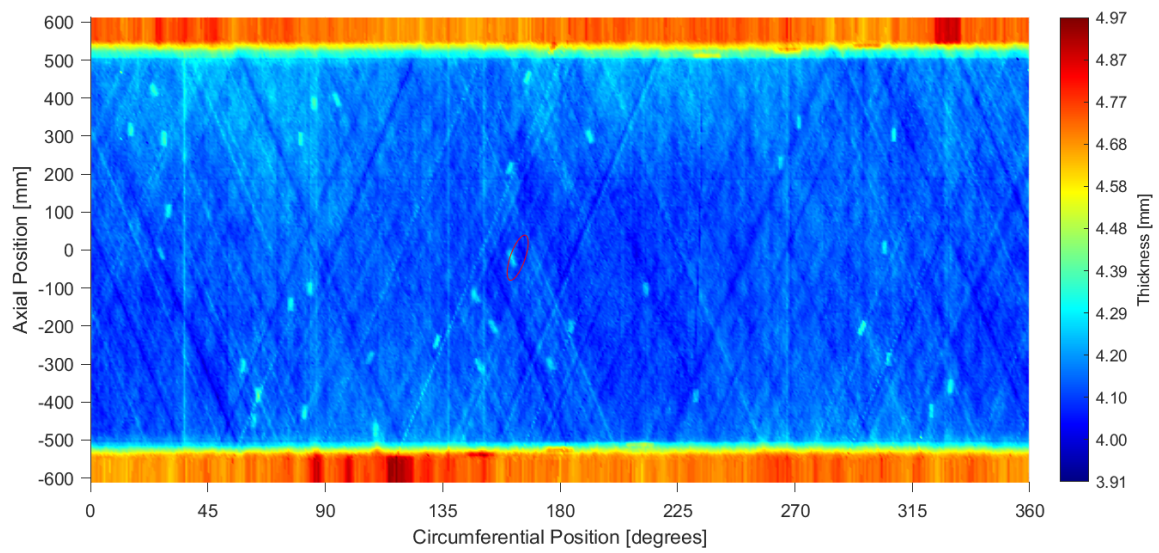


**Figure 9.38:** The delamination area (red ellipse) overlaid with the interpolated thickness.

---

## Chapter 10

---

# Conclusions

This research was part of a collaborative framework between NASA and Delft University of Technology on the NASA Engineering and Safety Center's Shell Buckling Knockdown Factor Project. The objective of this thesis was to contribute to the development of contemporary knockdown factors for imperfection-sensitive composite launch vehicle structures by creating pre-test simulations for an experimental buckling test and assessing the validity of the simulations in light of the experiment. A laboratory-scale composite cylindrical shell test article named NDL-1 was the subject of this investigation.

The research undertaken was accomplished via modeling NDL-1's unique inner, outer, and boundary surface imperfections for use in nonlinear dynamic simulations of the experiment. In addition, two other types of geometric imperfections that may be used to estimate experimental cylindrical shell buckling behavior were explored with an equivalent simplified shell model. The sensitivity of the shell's buckling behavior to loading imperfections – which are an inescapable reality in buckling experiments – was also studied prior to the test on the simplified shell model, with a view towards understanding the approximate order of influence of tilted loading edges on the buckling behavior.

Relative to the manufactured test article's 12.8% maximum mid-surface imperfection amplitude, it was clear that similar magnitude eigenmode and trigonometric imperfections of the shapes studied provided knockdown factors commensurate with the one prescribed by NASA SP-8007, 0.59. 10% eigenmode and trigonometric imperfections produced KDFs of 0.64 and 0.63, respectively, whereas the resultant KDF of the experiment was 0.91. Additionally, the resultant KDF agreement between S4R- and SC8R-element models with the 10% trigonometric and eigenmode imperfections indicated that transverse shear compliance may have been negligible for this laminate. Most probably this was due NDL-1's solid construction, which forgoes a transversely shear-compliant core material.

It was found that subtle loading imperfections could affect the buckling load of this cylindrical shell design. The response of the buckling load to loading imperfections began between  $0.001^\circ$  and  $0.01^\circ$  of planar tilt to the shell's upper boundary, which respectively reduced the buckling load of the shell without geometric imperfections by 0% and 3%.

Two simulations were conducted due to pre-test uncertainties in the material properties of the shell. A calibrated material variant was created to match the composite material's elastic moduli to the results of a tensile test. Then a recalibrated material property set was derived to account for a 4.3% average ply thickness difference that was observed between the manufactured test article and the tensile test specimens. The logic upon which the recalibrated material was derived was due to the possibility of more resin being bled off during NDL-1's manufacturing process than that of the tensile specimens. The recalibrated assumption thus stipulated that a cured tow of NDL-1 should have had the same amount of fibers as a cured tow of the tensile specimen, but with slightly reduced thickness and thus cross sectional area; as a result, the load-per-area elastic moduli would have increased.

Both simulations showed excellent agreement with the test. The calibrated simulation was able to predict NDL-1's buckling load within 0.08% and its axial stiffness within 0.2%. The recalibrated simulation matched both the buckling load and the stiffness of NDL-1 within 3.7%. The experimental displacement at buckling was within 1% of both simulations. It is possible that excess resin was not bled off relative to the tensile specimen, and that tow-spacing gaps caused by the shell's hand-layup process led to a change in aspect ratio of the cured tows' cross sections, while maintaining the same average cross-sectional area relative to the tensile specimens' tows. This could explain why the calibrated material simulation matched with experimental result slightly better than the recalibrated simulation. However, for conclusive answers on this matter, NDL-1's material properties should be thoroughly interrogated through destructive testing to validate material property assumptions. This would provide insight into additional complexities of the as-manufactured layup properties such as elastic nonlinearity. In summary, material property assumptions must be carefully approached, justified, and eventually validated when used in simulation.

A potential loading imperfection was found via DIC-derived axial displacement data around the moment of buckling. A best-fit plane to the data points indicated a possible  $0.003^\circ$  tilt of the top edge from the horizontal plane towards the  $151^\circ$  circumferential position of NDL-1. Based on the aforementioned loading imperfection sensitivity study, it was not expected that such a tilt would have affected the buckling load by more than 3%. To verify this assumption, the calibrated and recalibrated simulations with measured imperfections were re-run with the addition of this  $0.003^\circ$  tilt. The results confirmed that the buckling load was reduced by only 0.7%. With both measured and loading imperfections considered, the calibrated and recalibrated post-test simulations showed agreements of -0.8% and 3% with the experiment, respectively.

The pre-buckling shapes of the simulation and the experiment were qualitatively in agreement: both featured nine axial half-waves, which was also the prediction of NASA SP-8007. However, it is uncertain how well this correlation with SP-8007 would hold up in other manufacturing and simulation situations. This was due to the possibility that an axisymmetric mandrel imperfection, which was coincident with one of those axial half-waves, influenced the pre-buckling shape of the experiment and the simulation.

After the peak load, high-speed digital image correlation systems captured the experimental buckling evolution. A single dimple was first observed, which then propagated into a pattern of two axial half-waves and seven circumferential full-waves. This shape further evolved into a pattern of two axial half-waves and six circumferential full-waves. The simulation predicted two simultaneous initial dimples at the same axial location as the initial experimental dimple,

---

but neither was at the same circumferential location as the experiment. These evolved into a pattern of two axial half-waves and eight circumferential full-waves, which in turn transformed into a pattern of two axial half-waves and seven circumferential full-waves. Furthermore, the experimental buckling event was characterized by consistently greater radial displacement ranges than qualitatively similar stages of the simulation's buckling evolution.

The simulation's lack of damage modeling may have caused this discrepancy, as failure was expected to occur upon buckling. Because the buckling behavior is dictated by a structure's minimum strain energy state, the immediately incipient material failure following buckling may have changed the shell's minimum strain energy state during buckling propagation, thus leading to a cascading effect of qualitative differences in radial displacement magnitudes and patterns between the experiment and simulation.

With respect to the experiment itself, the importance of having multiple measurement systems cannot be overstated. The first axial displacement measurements were from DCDTs attached to the load frame. The stiffnesses derived from these DCDTs were not in good agreement either simulation. However, it was found that the strains for both simulations were qualitatively in very good agreement. This was initially found to be unusual, as the strains may be considered a "higher order" measurement than displacements. In other words, the displacements in the test and the simulation were prescribed, whereas structural and material responses lie between the imposed displacement input and the surface strains detected by strain gauges. Thus, it did not make sense that a higher order measurement showed better agreement with simulations than a lower order measurement. Consequently, axial displacement DIC data was used to assess if corroboration could be provided to the other data sources and simulations. Ultimately, the stiffness data derived from the low-speed DIC system provided excellent agreement with the that of the simulations, and further made sense in the context of the load-strain behavior. It was later determined that the load frame deformed substantially during the experiment as a result of the test article's stiffness; this was determined to be the cause of the anomalous DCDT measurements.

Overall, NDL-1's resultant KDF of 0.91 was much less conservative than the NASA SP-8007 KDF of 0.59, even in the presence of a slight loading imperfection. While design KDFs differ from resultant KDFs via the inclusion of statistical reliability limits, NDL-1's high normalized buckling load and its excellent agreement with simulation results indicate that measured imperfection modeling approaches could play a key role in developing updated and potentially less conservative knockdown factors for composite launch vehicle structures of the future.



---

## References

- [1] L.H. Donnell. A new theory for the buckling of thin cylinders under axial compression and bending. *Transactions of the American Society of Mechanical Engineers*, 56(12): 795–806, 1935.
- [2] T. von Kármán, L.G. Dunn, and H.S. Tsien. The influence of curvature on the buckling characteristics of structures. *Journal of the Aeronautical Sciences*, 7(7):276–289, 1940.
- [3] T. von Kármán and H.S. Tsien. The buckling of thin cylindrical shells under axial compression. *Journal of the Aeronautical Sciences*, 8(8):303–312, 1941.
- [4] W.T. Koiter. *On the stability of elastic equilibrium*. PhD thesis, Delft University of Technology, Delft, Netherlands, 1945.
- [5] V.I. Weingarten, P. Seide, and J.P. Peterson. Buckling of thin-walled circular cylinders. Technical Report NASA SP-8007, NASA, Springfield, Virginia, USA, 1968.
- [6] M. Hilburger and J. Starnes Jr. High-fidelity nonlinear analysis of compression-loaded composite shells. In *19th AIAA Applied Aerodynamics Conference*, number AIAA 2001-1394, Reston, Virginia, USA, 2001. American Institute of Aeronautics and Astronautics.
- [7] NASA Engineering and Safety Center technical bulletin no. 16-01. Technical Report 16-01, NASA Engineering & Safety Center, Hampton, Virginia, USA, 2016.
- [8] M. Hilburger. Developing the next generation shell buckling design factors and technologies. In *53rd AIAA/ASME/ASCE/AHS/ASC Structures, Structural Dynamics and Materials Conference 20th AIAA/ASME/AHS Adaptive Structures Conference 14th AIAA*, number AIAA 2012-1686, Reston, Virginia, USA, 2012. American Institute of Aeronautics and Astronautics.
- [9] S.G.P. Castro, R. Zimmermann, M.A. Arbelo, and R. Degenhardt. Exploring the constancy of the global buckling load after a critical geometric imperfection level in thin-walled cylindrical shells for less conservative knock-down factors. *Thin-Walled Structures*, 72:76–87, 2013.

- [10] M.R. Schultz, D.W. Sleight, D.E. Myers, Jr. Waters, W.A., P.B. Chunchu, A.E. Lovejoy, and M.W. Hilburger. Buckling design and imperfection sensitivity of sandwich composite launch-vehicle shell structures. In *American Society for Composites 31st Technical Conference*, number 2922, Williamsburg, Virginia, USA, 2016. American Society for Composites.
- [11] J. Kepple, M.T. Herath, G. Pearce, B.G. Prusty, R. Thomson, and R. Degenhardt. Stochastic analysis of imperfection sensitive unstiffened composite cylinders using realistic imperfection models. *Composite Structures*, 126:159–173, 2015.
- [12] B. Wang, K. Du, P. Hao, K. Tian, Y.J. Chao, L. Jiang, S. Xu, and X. Zhang. Experimental validation of cylindrical shells under axial compression for improved knockdown factors. *International Journal of Solids and Structures*, 164:37–51, 2019.
- [13] E. Zapata. The state of play US space systems competitiveness. Technical Report KSC-E-DAA-TN48988, NASA, Cocoa Beach, Florida, USA, 2017.
- [14] NASA Engineering & Safety Center 2017 technical update. Technical Report NP-2017-10-006-LaRC, NASA Engineering & Safety Center, Hampton, Virginia, USA, 2017.
- [15] NASA Engineering & Safety Center 2018 technical update. Technical Report NP-2018-11-126-LaRC, NASA Engineering & Safety Center, Hampton, Virginia, USA, 2018.
- [16] I. Uriol Balbin, C. Bisagni, M.R. Schultz, and M.W. Hilburger. Scaling methodology for buckling of sandwich composite cylindrical structures. In *2018 AIAA/ASCE/AHS/ASC Structures, Structural Dynamics, and Materials Conference*, number AIAA 2018-1988, Reston, Virginia, USA, 2018. American Institute of Aeronautics and Astronautics.
- [17] M.W. Hilburger, M.P. Nemeth, and J.H. Starnes Jr. Shell buckling design criteria based on manufacturing imperfection signatures. Technical Report NASA/TM-2004-212659, NASA, Hampton, Virginia, USA, 2004.
- [18] W. Haynie and M. Hilburger. Comparison of methods to predict lower bound buckling loads of cylinders under axial compression. In *51st AIAA/ASME/ASCE/AHS/ASC Structures, Structural Dynamics, and Materials Conference*, number AIAA 2010-2532, Orlando, Florida, USA, 2010. American Institute of Aeronautics and Astronautics.
- [19] A.C. Orifici and C. Bisagni. Perturbation-based imperfection analysis for composite cylindrical shells buckling in compression. *Composite Structures*, 106:520–528, 2013.
- [20] S.G.P. Castro, R. Zimmermann, M.A. Arbelo, R. Khakimova, M.W. Hilburger, and R. Degenhardt. Geometric imperfections and lower-bound methods used to calculate knock-down factors for axially compressed composite cylindrical shells. *Thin-Walled Structures*, 74:118–132, 2014.
- [21] H.N.R. Wagner, C. Hühne, S. Niemann, K. Tian, B. Wang, and P. Hao. Robust knock-down factors for the design of cylindrical shells under axial compression: Analysis and modeling of stiffened and unstiffened cylinders. *Thin-Walled Structures*, 127:629–645, 2018.

- [22] L. Friedrich, S. Loosen, K. Liang, M. Ruess, C. Bisagni, and K.U. Schröder. Stacking sequence influence on imperfection sensitivity of cylindrical composite shells under axial compression. *Composite Structures*, 134:750–761, 2015.
- [23] J. Arbocz and H. Abramovich. The initial imperfection data bank at the Delft University of Technology: Part I. Technical Report LR-290, Delft University of Technology, Delft, Netherlands, 1979.
- [24] C. Bisagni. Numerical analysis and experimental correlation of composite shell buckling and post-buckling. *Composites Part B: Engineering*, 31(8):655–667, 2000.
- [25] L. Wullschleger and H.R. Meyer-Piening. Buckling of geometrically imperfect cylindrical shells — definition of a buckling load. *International Journal of Non-Linear Mechanics*, 37(4-5):645–657, 2002.
- [26] M.W. Hilburger and J.H. Starnes Jr. Effects of imperfections on the buckling response of compression-loaded composite shells. *International Journal of Non-Linear Mechanics*, 37(4-5):623–643, 2002.
- [27] C. Hühne, R. Rolfes, E. Breitbach, and J. Teßmer. Robust design of composite cylindrical shells under axial compression — Simulation and validation. *Thin-Walled Structures*, 46(7-9):947–962, 2008.
- [28] R. Degenhardt, A. Kling, A. Bethge, J. Orf, L. Kärger, R. Zimmermann, K. Rohwer, and A. Calvi. Investigations on imperfection sensitivity and deduction of improved knock-down factors for unstiffened CFRP cylindrical shells. *Composite Structures*, 92(8):1939–1946, 2010.
- [29] M. Broggi and G.I. Schuëller. Efficient modeling of imperfections for buckling analysis of composite cylindrical shells. *Engineering Structures*, 33(5):1796–1806, 2011.
- [30] M. Broggi, A. Calvi, and G.I. Schuëller. Reliability assessment of axially compressed composite cylindrical shells with random imperfections. *International Journal of Structural Stability and Dynamics*, 11(02):215–236, 2011.
- [31] K.C. Wu, B.K. Stanford, G.A. Hrinda, Z. Wang, R.A. Martin, and H.A. Kim. Structural assessment of advanced tow-steered shells. In *54th AIAA/ASME/ASCE/AHS/ASC Structures, Structural Dynamics, and Materials Conference*, number AIAA 2013-1769, Boston, Massachusetts, USA, 2013. American Institute of Aeronautics and Astronautics.
- [32] M.A. Arbelo, R. Degenhardt, S.G.P. Castro, and R. Zimmermann. Numerical characterization of imperfection sensitive composite structures. *Composite Structures*, 108(1):295–303, 2014.
- [33] C. Schillo, D. Röstermundt, and D. Krause. Experimental and numerical study on the influence of imperfections on the buckling load of unstiffened CFRP shells. *Composite Structures*, 131:128–138, 2015.
- [34] S.C. White, P.M. Weaver, and K.C. Wu. Post-buckling analyses of variable-stiffness composite cylinders in axial compression. *Composite Structures*, 123:190–203, 2015.

- [35] R. Khakimova, S.G.P. Castro, D. Wilckens, K. Rohwer, and R. Degenhardt. Buckling of axially compressed CFRP cylinders with and without additional lateral load: Experimental and numerical investigation. *Thin-Walled Structures*, 119:178–189, 2017.
- [36] M.R. Schultz, D.W. Sleight, N.W. Gardner, M.T. Rudd, M.W. Hilburger, T. Palm, and N.J. Oldfield. Test and analysis of a buckling-critical large-scale sandwich composite cylinder. In *2018 AIAA/ASCE/AHS/ASC Structures, Structural Dynamics, and Materials Conference*, number AIAA 2018-1693, Reston, Virginia, USA, 2018. American Institute of Aeronautics and Astronautics.
- [37] E. Labans and C. Bisagni. Buckling and free vibration study of variable and constant-stiffness cylindrical shells. *Composite Structures*, 210:446–457, 2019.
- [38] A. Takano. Statistical knockdown factors of buckling anisotropic cylinders under axial compression. *Journal of Applied Mechanics*, 79(5):051004, 2012.
- [39] M.W. Hilburger and J.H. Starnes Jr. Effects of imperfections of the buckling response of composite shells. *Thin-Walled Structures*, 42(3):369–397, 2004.
- [40] H.R. Meyer-Piening, M. Farshad, B. Geier, and R. Zimmermann. Buckling loads of CFRP composite cylinders under combined axial and torsion loading – experiments and computations. *Composite Structures*, 53(4):427–435, 2001.
- [41] M.W. Hilburger. High-fidelity buckling analysis of composite cylinders using the STAGS finite element code. In *55th AIAA/ASME/ASCE/AHS/ASC Structures, Structural Dynamics, and Materials Conference*, number AIAA 2014-0846, Reston, Virginia, USA, 2014. American Institute of Aeronautics and Astronautics.
- [42] B. Wang, S. Zhu, P. Hao, X. Bi, K. Du, B. Chen, X. Ma, and Y.J. Chao. Buckling of quasi-perfect cylindrical shell under axial compression: A combined experimental and numerical investigation. *International Journal of Solids and Structures*, 130-131:232–247, 2018.
- [43] C. Bisagni and M. Alfano. Probabilistic buckling analysis of sandwich composite cylindrical shells based on measured imperfections. In *58th AIAA/ASCE/AHS/ASC Structures, Structural Dynamics, and Materials Conference*, number AIAA 2017-0886, Grapevine, Texas, USA, 2017. American Institute of Aeronautics and Astronautics.
- [44] H.N.R. Wagner and C. Hühne. Robust knockdown factors for the design of cylindrical shells under axial compression: potentials, practical application and reliability analysis. *International Journal of Mechanical Sciences*, 135:410–430, 2018.
- [45] F. Franzoni, F. Odermann, E. Lanbans, C. Bisagni, M.A. Arbelo, and R. Degenhardt. Experimental validation of the vibration correlation technique robustness to predict buckling of unstiffened composite cylindrical shells. *Composite Structures*, 224:111107, 2019.
- [46] C.C. Chamis. Mechanics of composite materials: Past, present, and future. Technical Report NASA-TM-100793, NASA, Blacksburg, Virginia, USA, 1984.
- [47] J. Kepple, M. Herath, G. Pearce, G. Prusty, R. Thomson, and R. Degenhardt. Improved stochastic methods for modelling imperfections for buckling analysis of composite cylindrical shells. *Engineering Structures*, 100:385–398, 2015.

- [48] G. Cha and M.R. Schultz. Buckling analysis of a honeycomb-core composite cylinder with initial geometric imperfections. Technical Report NASA/TM-2013-217967, NASA, Hampton, Virginia, USA, 2013.
- [49] A. Przekop, M.R. Schultz, and M.W. Hilburger. Design of buckling-critical large-scale sandwich composite cylinder test articles. In *2018 AIAA/ASCE/AHS/ASC Structures, Structural Dynamics, and Materials Conference*, number AIAA 2018-1694, Reston, Virginia, USA, 2018. American Institute of Aeronautics and Astronautics.
- [50] P. Hao, B. Wang, G. Li, K. Tian, K. Du, X. Wang, and X. Tang. Surrogate-based optimization of stiffened shells including load-carrying capacity and imperfection sensitivity. *Thin-Walled Structures*, 72:164–174, 2013.
- [51] B. Wang, P. Hao, G. Li, Y. Fang, X. Wang, and X. Zhang. Determination of realistic worst imperfection for cylindrical shells using surrogate model. *Structural and Multidisciplinary Optimization*, 48(4):777–794, 2013.
- [52] B. Wang, X. Ma, P. Hao, Y. Sun, K. Tian, G. Li, K. Zhang, L. Jiang, and J. Guo. Improved knockdown factors for composite cylindrical shells with delamination and geometric imperfections. *Composites Part B: Engineering*, 163:314–323, 2019.
- [53] H.N.R. Wagner, E.M. Sosa, T. Ludwig, J. Croll, and C. Hühne. Robust design of imperfection sensitive thin-walled shells under axial compression, bending or external pressure. *International Journal of Mechanical Sciences*, 156:205–220, 2019.
- [54] C. Bisagni. Composite cylindrical shells under static and dynamic axial loading: An experimental campaign. *Progress in Aerospace Sciences*, 78:107–115, 2015.
- [55] D. Hibbit, B. Karlsson, and P. Sorensen. Abaqus/CAE user’s manual, 2010.
- [56] K. van Dooren. Buckling analysis and imperfection sensitivity study of scaled launch-vehicle cylindrical shells. Master’s thesis, Delft University of Technology, Delft, Netherlands, 2018.
- [57] M. Hilburger and J. Starnes Jr. Buckling and failure of compression-loaded composite cylindrical shells with geometric and material imperfections. Technical Report NASA/TM-2004-212677, NASA, Hampton, Virginia, USA, 2004.
- [58] E. Clarkson. Hexcel 8552 IM7 unidirectional prepreg 190 gsm & 35%RC qualification statistical analysis report. Technical Report NCP-RP-2009-028 Rev N/C, National Institute for Aviation Research, Wichita, Kansas, USA, 2011.
- [59] Micorox Standard Grout. Technical Report 3/14, Micor Co., Inc., Milwaukee, Wisconsin, USA, 2014.
- [60] C. Kassapoglou. *Design and analysis of composite structures with applications to aerospace structures*. John Wiley & Sons, Ltd, 2nd edition, 2013.
- [61] Z. Hashin and A. Rotem. A fatigue failure criterion for fiber reinforced materials. *Journal of Composite Materials*, 7(4):448–464, 1973.

- [62] J. Singer, J. Arbocz, and T. Weller. *Buckling experiments: experimental methods in buckling of thin-walled structures*, volume 2. John Wiley & Sons, Inc, 2002.
- [63] H.N.R. Wagner, C. Hühne, K. Rohwer, S. Niemann, and M. Wiedemann. Stimulating the realistic worst case buckling scenario of axially compressed unstiffened cylindrical composite shells. *Composite Structures*, 160:1095–1104, 2017.